

**GEOFORSCHUNGSZENTRUM POTSDAM**  
STIFTUNG DES ÖFFENTLICHEN RECHTS

---

# Scientific Technical Report

ISSN 1610-0956

Pavelyev, A.G., Wickert, J., Schmidt, Torsten, Gubenko, V.N.,  
Matyugov, S.S., Pavelyev, A.A.

## Radio holographic methods for atmospheric, ionospheric and stratospheric waves

Final report 2004 of a research contract between the INSTITUTE OF RADIO  
ENGINEERING AND ELECTRONICS OF THE RUSSIAN ACADEMY OF SCIENCES  
(IRE RAS), Moscow  
and  
GeoForschungsZentrum Potsdam (GFZ)

Scientific Technical Report STR 04/18

## CONTENTS

	p.p.
INTRODUCTION.....	4
1. RADIO HOLOGRAPHIC METHODS: REVIEW .....	7
1.1. IMPLEMENTATION OF THE RADIO HALOGRAPHY TO RO DATA ANALYSIS: BACKGROUND .....	7
1.2. CONNECTION BETWEEN RFSA, CT AND BP RADIO HOLOGRAPHIC METHODS .....	9
1.3. RESULTS OF COMPARISON OF RADIO HOLOGRAPHIC METHODS...	12
2. AMPLITUDE OF RO SIGNAL AS RADIO HOLOGRAPHIC INDICATOR FOR IONOSPHERIC DISTURBANCES.....	16
2.1. LOCAL MECHANISM OF RO AMPLITUDE VARIATIONS AND THE PROBLEM OF THE LOCALIZATION OF IONOSPHERIC DISTURBANCES.....	16
2.2. GEOGRAPHICAL DISTRIBUTION OF INTENSE IONOSPHERIC DISTURBANCES AS FUNCTION OF TIME .....	25
3. INFORMATIONAL CONTENT OF THE PHASE PART OF RO HOLOGRAM .....	30
3.1. CONNECTION BETWEEN THE PHASE OF RO SIGNALS AND VERTICAL TEMPERATURE PROFILES .....	30
3.2. COMPARISON OF TEMPERATURE PROFILES OBTAINED BY THE TRADITIONAL PHASE AND THE UPGRADED PHASE METHODS.....	34
4. GW PROPAGATION THEORY AND ITS APPLICATION FOR RO MEASUREMENTS OF GW STRUCTURES IN THE EARTH'S ATMOSPHERE.....	47
4.1. PROBLEM STATEMENT .....	47

4.2. GW AND PERTURBATIONS OF THERMODYNAMICAL PARAMETERS IN THE ATMOSPHERE .....	49
5. AMPLITUDE OF GPS RO SIGNALS AS RADIOHOLOGRAPHIC IMAGE OF GW IN THE ATMOSPHERE.....	53
5.1. ATMOSPHERIC GW: BACKGROUND.....	53
5.2. AMPLITUDE METHOD OF GW ANALYSIS.....	56
5.3. HORIZONTAL WIND PERTURBATIONS RESTORED FROM CHAMP AMPLITUDE DATA .....	75
SUMMARY AND CONCLUSIONS.....	82
RECOMMENDATIONS.....	86
ACKNOWLEDGEMENTS.....	88
REFERENCES.....	89

## INTRODUCTION

The final report contains a description of the results obtained within a research contract between IRE RAS and GFZ Potsdam during the period April-November 2004. The objectives of investigation included (1) the radio-holographic methods for obtaining vertical profiles of the vertical gradients of physical parameters in the atmosphere, (2) radio holographic methods for atmospheric, ionospheric and stratospheric waves, and (3) validation of the software with GPS/MET (GPS/METeorology, e.g., *Rocken et al.* 1997) and CHAMP (CHALLENGING Mini-satellite Payload, e.g., *Reigber et al.* 2005) data and final report with recommendations.

In the first section of the report a review of existing radio-holographic methods is presented. General Inversion Operator (GIO) is introduced for comparison of the existing radio holographic methods: Radio holographic Focused Synthetic Aperture (RFSA), Canonical Transform (CT), and Back Propagation (BP). It follows that RFSA, BP and CT methods are the particular cases of the more general GIO transform. In distinction with CT method, GIO transform is valid for any inclination of the orbital trajectory of the LEO satellite in the radio occultation (RO) plane. As follows from analysis, radio holography can be used after some modernization to realize highly- precise GPS radio signals for the purpose of remote sensing of the atmosphere, mesosphere, and terrestrial surface with high spatial resolution and accuracy.

The informational content of the amplitude part of RO radio holograms is analysed in the second section. The amplitude of RO signal is sensitive to ionospheric influence in the trans-ionospheric links. The noisy and impulsive fluctuations in the CHAMP RO amplitude data are similar to C-type and S-type ionospheric amplitude

scintillations previously observed at 1.5 GHz in mid-latitude region in satellite-to-Earth Inmarsat link. Amplitude scintillations can be associated with different types of the ionospheric structures. A local mechanism is introduced, which can be a cause of the amplitude variations connected with sharp gradients of the electron density in the inclined ionospheric plasma layers. A possibility is demonstrated to reveal the spatial distribution of the electron density in the inclined ionospheric layers from analysis of the RO amplitude variations. The seasonal, geographical and temporal distributions of the CHAMP RO events with high values of the  $S_4$  index of the C- and S- type amplitude variations observed during 2001-2003 years indicated their dependence on the solar activity. The amplitude part of the radio holograms of the CHAMP RO signals can be used to detect the ionospheric irregularities and to find their parameters. For illustration in the second section a possibility is indicated to locate the disturbances in the ionosphere by radio holographic method.

In the third section the informational content of the phase part of radio holograms is considered. It is shown that the most informative is the main refractivity part of the phase path excess. To extract full information on the upper stratosphere the upgraded phase method (UPM) is suggested. The examples of application of UPM method for analysis of the CHAMP RO phase data illustrated its effectiveness for the 35-65 km interval. This method produces the vertical temperature profiles from the phase data without application of the statistical optimization method. UPM method has a promise to be used as operational tool for current data analysis in RO experiments. This conclusion is illustrated by comparison with Earth-based lidar measurements.

In the fourth section the main relationships of the current theory of GW has been presented with aim to apply the results to analysis of the CHAMP RO data. The

new polarization relationship is found which connect the relative variations of the refraction index with horizontal wind perturbations caused by GW propagation.

In the fifth section the GW polarization and dispersion relationships and Hilbert transform are used to find the 1-D GW radio image in the atmosphere by analysing the amplitude radio hologram of the RO signal. The radio image, also called the GW portrait, consists of the phase and amplitude of the GW as functions of height. The GW activity is non-uniformly distributed with the main contribution associated with the upper troposphere and lower stratosphere in the 8-40 km interval. The height dependence of the GW vertical wavelength was inferred through the differentiation of the GW phase. Analysis of this dependence using the dispersion relationship for the GW gives estimation of the projection of the horizontal background wind velocity on the direction of the GW propagation.

In summary and conclusion the main results and recommendations are given. The work plan of the GFZ-IRE research contract is completely fulfilled.

## 1. RADIO HOLOGRAPHIC METHODS: REVIEW

### 1.1. IMPLEMENTATION OF RADIO HOLOGRAPHY TO RO DATA

#### ANALYSIS: BACKGROUND

The radio holographic methods for remote sensing use the diffractive integrals connecting the electromagnetic fields on some interface or curve in the space (for example, the orbital trajectory of a low earth orbit (LEO) satellite with a radio holographic receiver) with the field in the space between the transmitter and receiver. *Zverev*, 1975, obtained the 3-D scalar equation, which links the angular spectrum of the field with the angular spectrum of the back-propagated wave in the free space. *Marouf and Tyler*, 1982, described the inversion method for obtaining the spatial structure of the Saturn's rings using the radio holograms registered onboard Voyager spacecraft. They constructed a reference signal using the circular form of the rings and diffraction theory and obtained spatial resolution about of  $1/10 \dots 1/100$  of the Fresnel's zone size. *Kunitsyn*, 1991, *Kunitsyn et al.* 1994, considered the application of the tomographic methods for the remote sensing of the Earth's ionosphere using radio emission of the communication satellites. *Heise et al.* 2002, applied tomographic approach for investigation of the Earth ionosphere/plasmasphere using GPS radio navigational signals received on the CHAMP satellite. *Gorbunov et al.* 1996, introduced the back propagation (BP) method, based on the scalar diffractive 2-D integral, to heighten the vertical resolution in the RO experiments. The BP method has a significant difference in comparison with the radio holographic approach suggested by *Marouf and Tyler*, 1982. Back propagation is performed using the 2-D free space Green function rather than the Green function obtained as a solution of a boundary diffraction problem in a 3-D medium. *Pavelyev*, 1998, *Hocke et al.* 1999, *Igarashi et al.* 2000, 2001, *Pavelyev et al.* 2002 (a, b), 2004, derived a Radio-

holographic Focused Synthetic Aperture (RFSA) principle for RO data analysis. They applied Fourier analysis in the finite time intervals to product of the RO and reference signals with the aims (1) to obtain 1-D radio images of the atmosphere and terrestrial surface and (2) to retrieve the vertical profiles of the physical parameters in the atmosphere and mesosphere. Using their method one can directly determine the dependence of the refraction angle on the impact parameter without application of complex BP technology. *Hocke et al.* 1999, *Igarashi et al.* 2000, 2001, determined by the RFSA method the electron density  $N_e(h)$  and its vertical gradient  $dN_e(h)/dh$  in the mesosphere and temperature  $T(h)$  in the atmosphere. *Beyerle and Hocke*, 2001, *Igarashi et al.* 2001, applied the RFSA method to visualize signals reflected from the terrestrial surface. They were the first to reveal surface reflections and obtained 1-D radio images of the troposphere and the surface by analysis of GPS/MET and CHAMP RO data. *Igarashi et al.* 2001, *Pavelyev et al.* 2002 (a) provided preliminary analysis of radio images and estimated the vertical resolution of the RFSA method as about of 70 m. *Beyerle et al.* 2002, applied the RFSA method for investigation of boundary layer of the troposphere using surface reflections. They obtained important information with global coverage on the humidity concentration in the boundary layer of the atmosphere using the CHAMP RO data. It may be noted that the RFSA method is distinctive in comparison with the unfocused synthetic aperture (Doppler selection) method applied previously by *Lindal et al.* 1987, for the spectral analysis of RO data to obtain the radio images of the Uranus atmosphere. Some later unfocused synthetic aperture method has been named in publications as a sliding aperture method (*Gorbunov et al.* 2000). *Gorbunov*, 2002 (a, b) applied the presentation of the wave field as a sum of spherical waves to correct approximately for the wave front curvature and considered examples of radio images with multiple

direct and reflected rays using the GPS/MET RO data. In the case of unfocused synthesis the size of the synthetic aperture and the vertical resolution are limited by an uncertainty condition between resolution in the impact parameter and refraction angle (*Gorbunov et al.* 2000). The RFSA method, in principle, does not obey the uncertainty condition because it accounts for the curvature of the wave fronts corresponding to the physical rays after propagation in the Earth's atmosphere and can use the large size of the synthetic aperture for effective compression of the angular plane wave spectrum of the RO signal. According to this advantage the RFSA method can discern the surface reflections near the powerful tropospheric RO signal and can realize in practice the high values of the vertical resolution  $\sim 100$  m as expected early for the BP method (*Hocke et al.*, 1999, *Igarashi et al.* 2000, 2001). Note, however, that to achieve high resolution in the multi-path areas the RFSA method must use accurate model of the refractivity in the RO region to construct the reference signal, which must have high coherence with RO signal. Recently *Gorbunov*, 2002 (c) introduced the Canonical Transform (CT) method for processing GPS RO data in the lower troposphere. The main idea of the CT method consists of using Fourier Integral Operators (FIO) to find directly the dependence of the refraction angle on the impact parameter for each physical ray in multi-path conditions. *Jensen et al.* 2003, introduced Full Spectrum Inversion (FSI) method to process the RO signals. They established a novel connection between the derivative of the phase of a physical ray on the instantaneous frequency in the full Fourier spectrum of the RO signal and the time of intersection of the physical ray with orbital trajectory of LEO satellite. This feature of the FSI method can be used to obtain under an assumption of spherical symmetry the refraction angle and impact parameter for each physical ray.

The progress in developing the radio holographic investigations is connected, in particular, with existence of the radio navigational satellite systems GPS/GLONASS, which are emitting high-precision, coherent and stable radio signals. The radio holographic methods can be used to realize the high-precision and stability of the radio signals of the radio navigational systems and obtain extreme values of the spatial resolution and accuracy in the remote sensing of the atmosphere and terrestrial surfaces from space. The aim of this section consists in introducing a way to obtain the CT and BP transforms and establishing their limitations using GIO.

## 1.2. CONNECTION BETWEEN RFSA, CT AND BP METHODS

The key geometrical parameters of GPS RO experiment are shown in Fig. 1.1. GPS transmitter emits radio signals, which propagate along the ray trajectory GTP through the entrance part of the ionosphere, atmosphere, the exit part of the ionosphere, and then arrive to receiver installed on Low Earth Orbit (LEO) satellite (point P in Fig. 1.1). The receiver registers the phase and amplitude of radio waves during the LEO orbital motion and produces two 1D radio holograms at two GPS frequencies  $f_1=1575.42$  MHz and  $f_2=1227.60$  MHz. The radio holographic approach (RFSA, CT, and BP methods) can be used to reveal the vertical profiles of physical parameters in the ionosphere and atmosphere along the trajectory of motion of the tangent point T (Fig. 1.1), where the ray trajectory GTP has minimal height above the Earth's surface.

Zverev's transform (Zverev, 1975) can be applied to reveal connections between RFSA, CT and BP methods (Pavelyev et al. 2004). Zverev's transform connects the field  $E(y,z)$  and its angular spectrum  $A(\alpha)$  (Zverev, 1975)

$$E(y,z) = (2\pi)^{-1} \int d\alpha A(\alpha) \exp\{ik[\Phi(\alpha,y,z) - \Phi_j(\alpha)]\}, \quad \Phi(\alpha,y,z) = z \cos \alpha + y \sin \alpha,$$

$$\Phi_j(\alpha) = \Phi(\alpha, y_j, z_j), \quad A(\alpha) = k g(\eta) \cos \alpha, \quad g(\eta) = \int E(y, z_j) \exp(-ik\eta y) dy, \quad \eta = \sin \alpha \quad (1.1)$$

where  $g(\eta)$  is the spatial plane-waves spectrum of the field depending on the direction of the plane wave propagation  $\alpha$ , the spatial spectrum  $g(\eta)$  can be found as a Fourier transform of the field in an arbitrary plane located in the free space at co-ordinate  $z=z_j$ ;  $\Phi(\alpha)$ ,  $\Phi_j(\alpha)$ ,  $y_j, z_j$  are the phase function, initial phase, and initial co-ordinates of the  $j$ -th physical ray. The origin of the co-ordinate system  $y, z$  coincides with point  $O$  and axis  $OY$  is perpendicular to direction  $GP$  (Fig. 1.1). Integral (1.1) can be evaluated by method of the stationary phase (SP) as the sum of the fields of the physical rays in the free space. We introduce GIO transform  $I(p)$  of the field  $E(y, z)$ :

$$I(p) = k/2\pi \int d\eta B(\eta) \exp[ik[pf(\eta) - d(\eta)]] I_1(\eta),$$

$$I_1(\eta) = \int ds \exp(-ik\eta s) R(s) E(y(s), z(s)), \quad (1.2)$$

where  $I_1(\eta)$  is the internal operator,  $R(s)$  is the reference signal,  $B(\eta)$  is the amplitude function,  $d(\eta)$  is the auxiliary phase function,  $f(\eta)$  is the impact function,  $p$  is the parameter, having different physical interpretation depending on  $f(\eta)$ ,  $s$  is the path of integration along the orbital trajectory of LEO satellite.

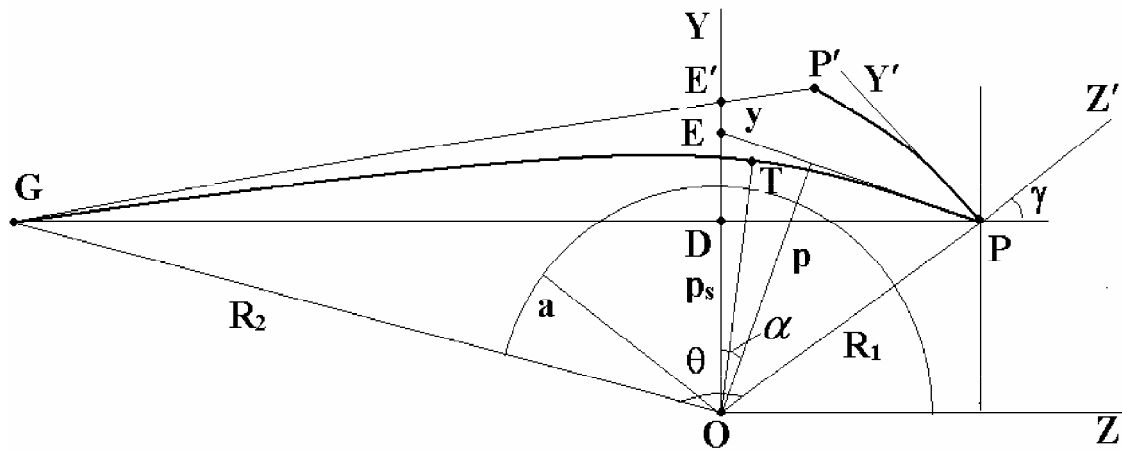


Fig. 1.1. Key geometrical parameters for GIO, RFSA, CT and BP methods.  $PP'$  is the orbital trajectory of LEO satellite.

The GIO transform can be considered as a generalization of the Egorov's Fourier integral operator (Egorov, 1985). The reference signal  $R(s)$  is included in GIO with

aim to compress the angular spectrum and to account for the deflection of the orbital trajectory from the straight line  $PP'$  (Fig. 1.1). The functions  $f(p, \eta)$ ,  $B(p, \eta)$ ,  $d(\eta)$  can be arbitrary and their physical meaning can be revealed using Zverev's presentation for the field (1.1). The RFSA method uses only the operator  $I_l(\eta)$  with the reference signal  $R(s)$  in (1.2). RFSA method can retrieve the field along the curved rays (e.g. rays  $P'E'$ ,  $PE$  in Fig. 1.1) with some approximation depending on the degree of spatial compression achieved. RFSA method can construct the phase and amplitude of the fields in the plane  $GOY$  (Fig. 1.1) and thus obtain the 1-D radio images of the atmosphere and terrestrial surface (Igarashi *et al.* 2001, Pavelyev *et al.* 2002(a), 2002(b)). RFSA method can account for the motion of GPS transmitter in any direction and influence of the horizontal gradients in the ionosphere and atmosphere by means of their introducing to the refractivity model. However RFSA method requires algorithms for solution of the direct propagation problem with accounting for diffraction effect to achieve maximal spatial compression with aim to apply perturbation method to find from experimental data correction to the modeled refractivity profiles.

To obtain connection between the GIO, BP and CT method we introduce the new co-ordinate system  $y', z'$  with the center at point  $P$  and oriented at angle  $\gamma$  relative to the  $OZ$  axes of the co-ordinate system  $y, z$  (Fig. 1.1). The co-ordinate  $y'$  is reckoned from point  $P$  along the tangent to orbital trajectory of LEO satellite. The co-ordinates  $y, z$  and  $y', z'$  are connected by equations

$$y=y_p+y'\cos\gamma+z'\sin\gamma; z=z_p+z'\cos\gamma-y'\sin\gamma, \quad (1.3)$$

where  $y_p, z_p$  are the co-ordinates of the point  $P$  (Fig. 1.1) in the co-ordinate system  $ZOY$  (Fig. 1.1). Now we can substitute the integration variable  $y'$  instead of  $s$  in the

operator  $I_1(\eta)$ . After substitution (1.1), (1.3) into (1.2) and changing the order of the integral operators one can perform integration on  $y'$ ; letting  $z'=0$ ,  $R(s)=I$

$$I_1(\eta)=k/2\pi\int dy' \exp\{-iky'[\eta-\sin(\alpha-\gamma)]\}=\delta(\eta-\sin(\alpha-\gamma)) \quad (1.4)$$

Integration on  $\eta$  in (1.2) after substitution (1.4) gives

$$E(p)=\int d\alpha A(\alpha)\exp\{ik[pf(\eta(\alpha))-d(\eta(\alpha))+z_p\cos\alpha+y_p\sin\alpha-\Phi_j(\alpha)]\}B(\eta(\alpha)),$$

$$\eta(\alpha)=\sin(\alpha-\gamma). \quad (1.5)$$

The left part (1.5) is the field  $E(p)$  transformed by the operator  $I(p)$  from the RO signal. The function  $d(\eta)$  in (1.2) is arbitrary, and one can chose  $d(\eta)$  in the GIO transform (1.2) to simplify the right part of the first equation in (1.5)

$$d(\eta)=z_p\cos(\gamma+\sin^{-1}\eta)+y_p\sin(\gamma+\sin^{-1}\eta). \quad (1.6)$$

If the origin of the co-ordinate system  $y'$ ,  $z'$  is disposed at the  $OZ$  axis and  $\gamma=0$ ,  $y_p=0$ , then the function  $d(\eta)$  is equal to  $z_p(1-\eta^2)^{1/2}$  and coincides with the phase of the transfer function for free space introduced previously (Zverev, 1975).

The choice of the impact function  $f(\eta)$  in the form  $f(\eta)=\sin(\gamma+\sin^{-1}\eta)=\sin\alpha$  and the amplitude function  $B(\eta(\alpha))=I$  in (1.5) corresponds to BP method. In this case the right part of the first equation in (1.5) coincides with (1.1), if  $z=0$ , and, as a consequence, corresponds to the distribution of the field along the straight line  $OY$ . The undetermined parameter  $p$  can be recognized as the co-ordinate  $y$  (Fig. 1.1).

The second important partial case is  $f(\eta)=\gamma+\sin^{-1}\eta=\alpha$ . For the case  $\gamma=0$  this function has been found previously by the CT method (Gorbunov, 2002(c)). For the second case SP method gives connection between the direction angle  $\alpha_j$  and parameter  $p$

$$p=-z_j\sin\alpha_j+y_j\cos\alpha_j \quad (1.7)$$

Equation (1.7) defines  $p$  as the distance between the  $j$ -th physical ray and the center of the co-ordinate system - point  $O$  (Fig. 1.1). If the center of global spherical symmetry of the medium coincides with point  $O$ , then  $p$  is the impact parameter of the  $j$ -th ray.

The SP method gives the next formula for the transformed field

$$E(p,0) = (2\pi/k)^{1/2} L_j^{-1/2} A(\alpha_j) B(\alpha_j) \exp[ik(p\alpha_j - \Phi_j(\alpha_j))], \quad L_j = (R_j^2 - p^2)^{1/2}, \quad (1.8)$$

where  $R_j$  is the distance of the initial point of  $j$ -th physical ray with co-ordinates  $y_j, z_j$  from the point  $O$  (Fig. 1.1). The function  $B(\alpha_j)$  in (1.8) is not specifically determined. It can be chosen according to energy conservation law, using the expression for the refraction attenuation of the radio waves earlier derived for 3D case by *Pavelyev and Kucherjavenkov, 1978*. However for estimation of the refraction angle the form of the function  $B(\alpha_j)$  is not significant.

When the modified refraction index  $M(r)$  is a monotonic function, only one physical ray can correspond to the impact parameter  $p$ . A possibility for the multi-path effect corresponding to monotonic  $M(r)$  profiles has been revealed previously by *Pavelyev, 1998*. In this case the GIO can disentangle the multi-path rays expressing the ray direction angle  $\alpha$  as a single-valued function of the impact parameter  $p$ . The CT method has the same capability as a partial case of the GIO transform when  $\gamma=0$ . The ray direction angle  $\alpha$  can be determined from (1.8) by differentiating the phase of the transformed field:  $\alpha = d \arg E(p) / dp$  (*Gorbunov, 2002 (c)*). Note, that in this case the BP method can be a subject of multi-path distortions. In reality only the centers of the local spherical symmetry may exist for different parts of the ray trajectories in the ionosphere and atmosphere. In this case the phase of the field transformed by the GIO, CT and BP methods may contain distortions connected with horizontal gradients in multi-path situation.

### 1.3. RESULTS OF COMPARISON OF RADIO HOLOGRAPHIC METHODS

The derivation made above has an advantage to indicate the approximations and features inherent in different radio holographic methods. The reference signal in the RFSA method accounts for the relative motion of the GPS transmitter and LEO receiver. Thus RFSA method is valid for arbitrary form of the satellites orbits and moving GPS transmitter. RFSA method can resolve the different rays in the multi-path situation and restore the field in physical space between transmitter and receiver, thus having feasibility to obtain radio image of the ionosphere, atmosphere and the Earth's surface. This has been demonstrated when the reflections were detected in the first time in GPS/MET and then in CHAMP RO data (*Igarashi et al. 2001, Beyerle and Hocke, 2001*). The 1D radio images obtained by RFSA method have been used to set an upper limit on the vertical resolution of GPS RO method ~ 70 m (*Igarashi et al. 2001, Pavelyev et al. 2002 (a, b), Pavelyev et al. 2004*).

The GIO, CT and BP methods are needed in general case of the arbitrary satellites orbits in the recalculation of the field to account for the transmitter motion. The BP method is useful in the case of absence of multi-path propagation and thus have limited application because possible phase distortions in multi-path situation. Note, that BP method has an important feasibility to estimate location of the ionospheric disturbances because BP method restores the field in physical space. The position of a disturbance can be determined by BP method as a location in space where the amplitude scintillations in the restored field have minimum value (*Sokolovskiy, et al. 2002*). The same feasibility has RFSA as a method, which allows restoration of the field in physical space. Because this feasibility RFSA and BP method share the common property to locate inhomogeneities along with tomographic methods derived earlier (e.g., *Kunitsyn et al. 1994; Heise et al. 2002*).

The GIO and CT method can disentangle multi-path rays and to find the dependence of the refraction angle on the impact parameter in the case when the modified refractivity index is monotonic function of height. GIO transform has some advantage because the CT method is valid for the specific case when  $\gamma=0$  and the orbit of the LEO satellite is perpendicular to direction PG (Fig. 1.1) (Gorbunov, 2002 (c)). The GIO transform is valid for general case of any inclination of the orbit of LEO satellite relative to direction GP. Both GIO and CT method present the field in the abstract space and require the knowledge of localization of the center of global spherical symmetry of the medium.

## 2. AMPLITUDE OF RO SIGNAL AS RADIO HOLOGRAPHIC INDICATOR OF THE IONOSPHERIC DISTURBANCES

### 2.1. LOCAL MECHANISM OF RO AMPLITUDE VARIATIONS AND PROBLEM OF LOCATION OF THE IONOSPHERIC DISTURBANCES

The radio signals emitted at two frequencies  $f_1=1575.42$  and  $f_2=1227.6$  MHz by Global Positioning satellite System (GPS) are used for the RO investigations of the F- and E-layers of the ionosphere (Hajj and Romans, 1998, Vorob'ev et al. 1999, Igarashi et al. 2001, Sokolovskiy et al. 2002, Liou et al. 2002). During a RO experiment the ray linking a receiver installed on a low earth orbit (LEO) satellite to a GPS satellite (marked by point L and G in Fig. 2.1, respectively) immerses sequentially into the ionosphere and atmosphere, and its direction (Fig. 2.1) is changed by the bending angle  $\xi(p)$ , depending on the impact parameter  $p$  because the refraction effect (Fig. 2.1). The main contribution to the amplitude of the RO signal in the case of the quiet ionosphere is introduced by relatively small area along the ray GTL with center at the tangent point T (Fig. 2.1), where the ray trajectory is perpendicular to the local gradient of the refractivity. If precise orbital data are given,

the height  $h$  of point T can be evaluated under assumption of the spherical symmetry with center at point O (Fig. 2.1). For some RO experiments strong amplitude scintillations have been observed at height interval above the neutral atmosphere and below the E-layer of the ionosphere (Sokolovskiy *et al.* 2002). Also sporadic amplitude scintillations have been indicated at GPS frequencies in satellite-earth links (Yeh and Liu, 1982, Karasawa *et al.* 1985). Karasawa *et al.* 1985, showed that

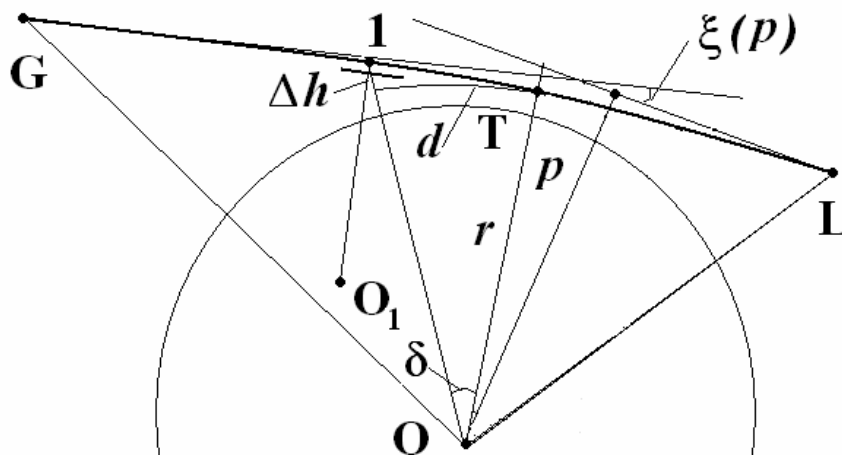


Fig. 2.1. Geometry of propagation in satellite-satellite path.

sporadic amplitude scintillations can be caused by plasma disturbances in the ionospheric E- and F- layers.

In this section we indicated that the inclined plasma layers in the ionosphere can be an additional source of the sporadic amplitude scintillations in satellite-satellite and satellite-earth links. We show also that the sporadic amplitude scintillations observed in the RO experiments in the height interval  $h$  40-80 km are containing important information concerning the seasonal, geographical and temporal distributions of the ionospheric disturbances on a global scale.

In the absence of the global spherical symmetry a new tangent point 1 can appear in the ionosphere, where sharp gradient of the electron density in an inclined plasma layer is perpendicular to the ray trajectory GTL (Fig. 2.1). This point can appear on

both sides of the ray GTL (GT or TL) according to which part of the ray trajectory is occupied by an inclined sporadic plasma layer. In this case the height  $h(T)$  of the observed RO amplitude variations depends on inclination  $\delta$  of the inclined plasma layer relative to the local horizontal direction (Fig. 2.1). As a consequence the apparent height displacement  $\Delta h$  can arise in the estimated value of the altitude of the inclined plasma layer (Fig. 2.1). The layer's inclination  $\delta$  and its horizontal displacement relative to point T  $d$  can be evaluated using Fig. 2.1

$$\delta=(2\Delta h/r)^{1/2}, \quad d=(2\Delta hr)^{1/2}, \quad \Delta h=d^2/(2r), \quad (2.1)$$

where  $r$  is the distance OT (Fig. 2.1).

Below we describe the amplitude variations of the RO signal connected with ionospheric influence by magnitude of the  $S_4$  scintillation index (Yeh and Liu, 1982):

$$S_4=2[<(A(t)-<A>)^2>/<A>^2]^{1/2} \quad (2.2)$$

where  $\langle \rangle$  is the average relevant to the height interval  $h(T)$  40-80 km,  $A(t)$  is the amplitude of the RO signal. For analysis we used the amplitude data obtained during CHAMP RO experiment described by Wickert *et al.* 2001.

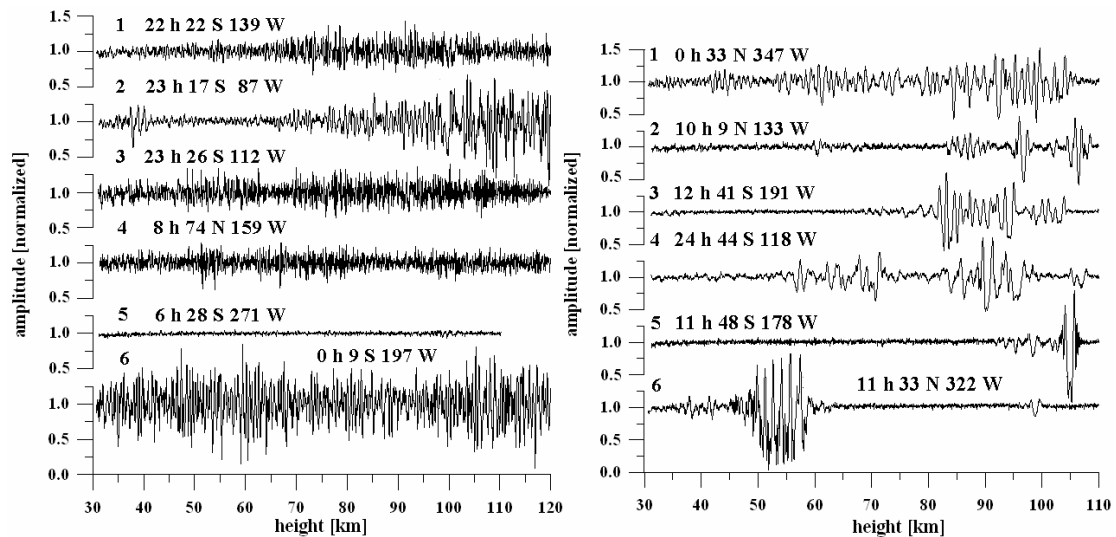


Fig. 2.2. Left panel: C-type noisy amplitude scintillations of RO signal. Right panel: S-type quasi-regular amplitude variation. Legends indicate the local time (LT) and the geographical co-ordinates of RO experiments.

The CHAMP RO amplitude variations for some RO events, which can be recognized as C- and S- types of the amplitude scintillations observed earlier by *Karasawa et al.* 1985, in the communication Inmarsat link at frequency 1.5 GHz are shown in Fig. 2.2.

The noisy C- type amplitude variations in the RO signals are given in Fig. 2.2, left panel. These scintillations have been observed in the equatorial region at local evening during RO events No. 0051, November 19; No. 0053, July 05; No. 0069, February 24; No. 0135, July 04, 2003 year. Average values of the  $S_4$  index are equal to 0.19, 0.32, 0.20, 0.50 (curves 1,2,3,6, respectively). Event 0159 corresponds to local morning (May 03), in the polar ionosphere with  $S_4=0.16$  (curve 4). Curve 4 corresponds to the noisy event near the north geomagnetic pole. Curve 5 relates to the quiet nighttime ionosphere with  $S_4=0.03$  (event No. 0198, May 03), when the amplitude fluctuations in the height interval  $h(T)$  30-110 km were caused by receiver noise. The geographical position and local time of the noisy RO events correspond to the same parameters of the noisy amplitude scintillations observed previously in satellite-earth links (e.g. *Yeh and Liu*, 1982). Noisy scintillations can be associated with small-scale plasma irregularities in the F- or E- layers of the ionosphere (*Yeh and Liu*, 1982, *Karasawa et al.* 1985).

Quasi-regular amplitude variations are shown in Fig. 2.2, right panel. Curves 1, 2, 4 correspond to the CHAMP RO events No. 0093, 0239, 0010, February 24 (mid-latitude nighttime and equatorial daytime ionosphere); curves 3, 5 relate to events No. 0050, 0171, November 19; and curve 6 corresponds to event No. 0246, July 05, 2003 (daytime mid-latitude ionosphere).

Inclined plasma layers in the E- or F-region of the ionosphere can be a cause of the quasi-regular amplitude variations in the RO signals. One can apply equation

(2.1) to estimate the inclination  $\delta$  and horizontal displacement  $d$  of the layer relative to point T (Fig. 2.1) if the apparent displacement  $\Delta h$  in the height of a plasma layer is known. However the uncertainty in the sign of the horizontal displacement  $d$  and inclination  $\delta$  exists because the ionospheric disturbance can be located at the same distance  $d$  from point T on the part GT or LT of the ray trajectory GTL (Fig. 2.1). Note that application of BP method as shown by *Sokolovskiy et al.* 2002, gives a promise to solve in special cases the task of localization of the ionospheric disturbances.

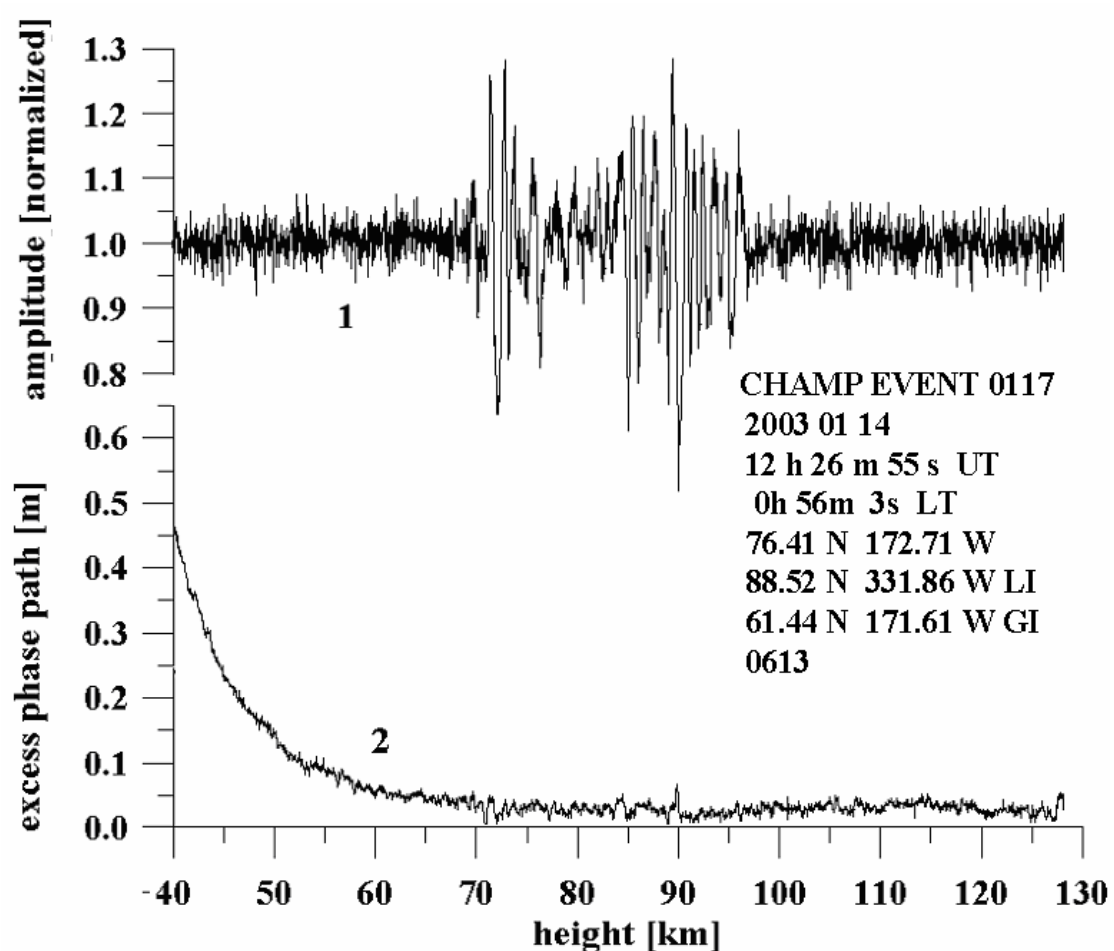


Fig. 2.3. Amplitude of the CHAMP RO signal (curve 1) and phase path excess at combined frequency F0 (curve 2) as functions of the height of the tangent point T (Fig. 2.1).  $S_4$  index was equal to 0.12. This value of the  $S_4$  index corresponds to disturbed ionosphere.

Estimation of location of the inclined layers can be provided also by RFSA method. For demonstration we will use CHAMP RO event (January 14, 2001, 0 h 56 m LT, 76.4 N, 172.7 W) with strong quasi-regular amplitude variations.

In Fig. 2.3 the amplitude variations in the CHAMP RO signal are compared with the phase path excess at combined frequency  $F_0$ . As seen from Fig. 2.3 the amplitude variations are contained in the interval  $0.6 < A < 1.3$ . The form of the amplitude variations indicates that the ionospheric disturbance consists of two connected patches which are responsible for the maximums in the amplitude changes in the 72-76 km and 84-96 km intervals of  $h(T)$ . In the 76-84 km interval of  $h(T)$  the amplitude variations are notable; however they are not so strong. Existence of the amplitude variations in this height interval indicates that the considered ionospheric disturbance is a unified structure distributed in the horizontal and vertical directions. The phase variations at frequency  $F_0$ , as seen in Fig. 2.3, are small. This reveals good quality of the ionospheric correction provided by usual method of subtracting ionospheric influence from the phase path excesses measured at frequencies  $F_1$  and  $F_2$ . This indicates also that the ray paths in the ionosphere for frequency  $F_1$  and  $F_2$  are nearly the same.

One can retrieve the electron density distribution and its gradient from amplitude variations of the RO signal by using method described by *Liou et al.* 2002.

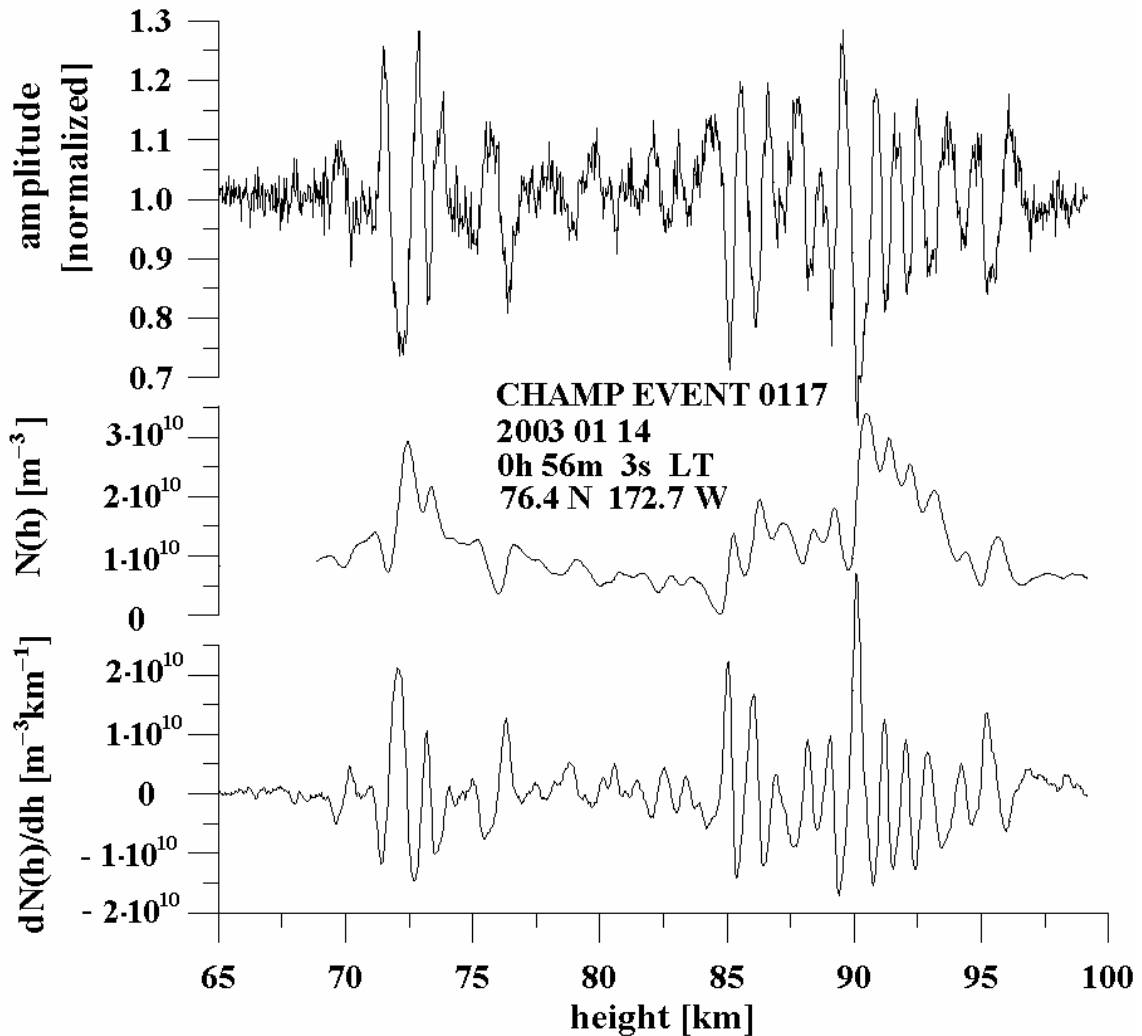


Fig. 2.4. The amplitude variations (top curve), the electron density distribution  $N(h)$  (middle curve) and the gradient of the electron density distribution  $dN(h)/dh$  (bottom curve) as functions of height  $h$  of the tangent point T (Fig. 2.1).

The results of restoration are shown in Fig. 2.4. As follows from Fig. 2.4, the electron density variations are concentrated in the interval  $0 < N(h) < 3.5 \cdot 10^{10}$  [electrons/m<sup>3</sup>]. These magnitudes of  $N(h)$  are somewhat below the usual values of  $N(h)$  for sporadic E-layers. The height interval of the amplitude variations is nearly equal to height interval of the variations in the electron density and its gradient. Two patches of the ionospheric layer are clearly seen in Fig. 2.4. The first one is located in the 84.5- 96 km interval; the second one is concentrated in the 70-76 km interval of  $h(T)$ . The 70-76 km interval for the second patch is unusual. This indicates, that in reality the height

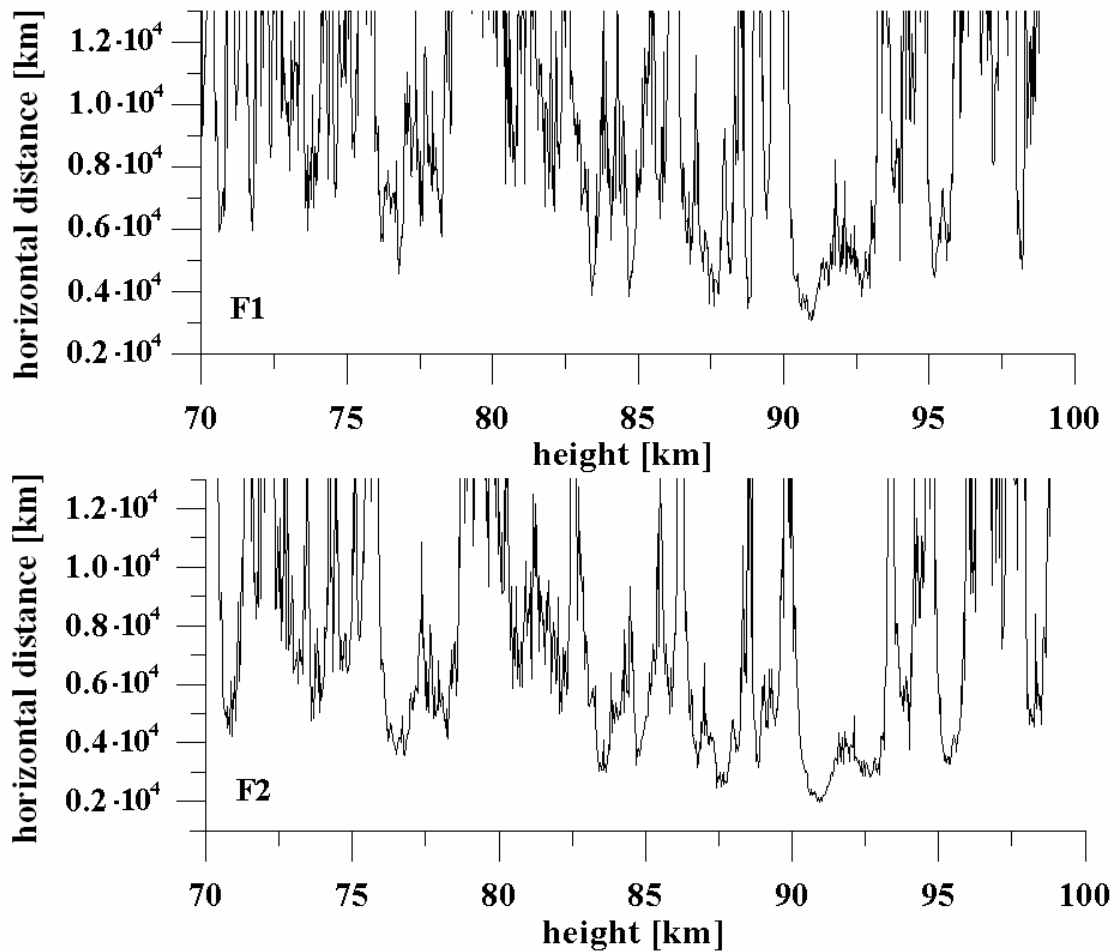


Fig. 2.5. Results of estimation of the horizontal distance  $D$  at frequency F1 (upper panel) and F2 (bottom panel).

of this patch is not equal to the altitude of point T and must be corrected by value  $\Delta h$  (Fig. 2.1). Also some correction  $\Delta h$  must be introduced in the height of the first patch. For correction one can use the third equation (2.1). If the horizontal distance  $d$  of the patch from point T is known, one can estimate the value  $\Delta h$  and the inclination  $\delta$  of the patch relative to the horizontal direction.

RFSA method can be applied to estimate location of the ionospheric disturbance. RFSA method can find the temporal dependence of the curvature radius of the wave front along the LEO orbit and then estimate the horizontal distance  $D$  from the receiver up to the ionospheric disturbance. Results of determination of the horizontal distances  $D_1(h)$ ,  $D_2(h)$  as function of the height of point T (Fig. 2.1) are shown for

considered event in Fig. 2.5. The upper panel in Fig. 2.5 corresponds to the horizontal distance  $D_1(h)$  at frequency F1, the bottom panel in Fig. 2.5 relates to the horizontal distance  $D_2(h)$  at frequency F2. Only the values of the horizontal distance below 13000 km are shown in Fig. 2.5. The minimal values of the horizontal distance  $D$  are important for location of the ionospheric disturbance. The noise in minimal values of the horizontal distance  $D$  at the first frequency is of greater intensity than that at the second frequency. This is connected with dispersion effect because the plasma refractivity at the first frequency is of about 1.65 times below that at the second frequency. For location of the inclined layer the data at the frequency F2 have been used as more sensitive to plasma perturbations. As follows from Fig. 2.5 the minimal values of the horizontal distance  $D_2(h)$  measured at frequency F2 are located in the 2400-2600 km interval for the height  $h(T)$  about of 91-92 km. For these values  $h(T)$  the distance LT (Fig. 2.1) was equal to 2100 km in the considered RO event. It follows from this analysis that the ionospheric layer has been located in the entrance part of the ionosphere between point G and T (Fig. 2.1) at the distance  $d$  changing in the interval 300 – 500 km. The corresponding values  $\Delta h$  changes in the 8-24 km interval. Thus the first patch of the layer is located on line GT at a distance 300 km from point T. It is concentrated in the 92-104 km interval with negative inclination to horizontal direction  $\delta$  of about  $3^\circ$ . The second patch is located on the line GT in the 94-100 km interval at the distance 500 km relative to the tangent point T (Fig. 2.1) with negative inclination of about  $5^\circ$ . Between two patches the plasma density is small. As follows from this analysis the amplitude variations in the 70-96 km interval of altitude  $h(T)$  are connected with sporadic E-layer located along the line GT at the height 92-104 km at the distance 300-500 km relative to point T. The inclination of the sporadic E-layer is changed along the line GT from  $3^\circ$  up to  $5^\circ$ . Thus RFSA

method can resolve the uncertainty in location of the inclined layer between the part GT and LT of the ray trajectory.

Note, that the procedure suggested above for location of the inclined ionospheric layers requires additional validation by analysis of the CHAMP data and comparison with ground-based ionosonde information for validation.

## 2.2. GEOGRAPHICAL DISTRIBUTION OF INTENSE IONOSPHERIC DISTURBANCES AS FUNCTION OF TIME.

The geographical distribution of the strong ionospheric events (with an  $S_4$  index greater than 0.2), for all types of amplitude scintillations, in the CHAMP RO signals at 1575.42 MHz is illustrated in Fig. 2.6, 2.7. The distribution of the ionospheric events indicates that they are concentrated in some regions (e.g., the equatorial and geomagnetic North and South polar zones in Fig. 2.6 and 2.7). Strong activity in some equatorial regions may be connected with the evening ionospheric disturbances that arise after sunset, 20-24 hours of local time, in accordance with earth-based measurements reviewed earlier (e.g. *Yeh and Liu, 1982*). As seen in Fig. 2.6, 2.7, the number of strong ionospheric events and their intensity decreases as time going on from September 2001 to January 2004.

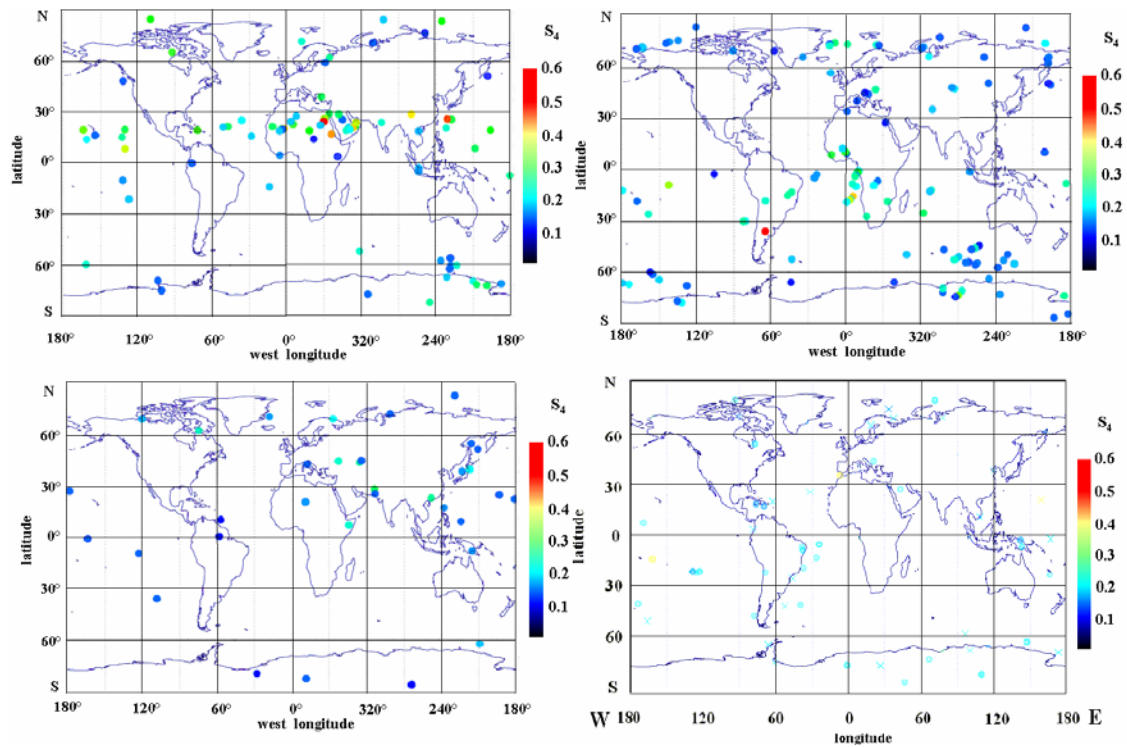


Fig. 2.6. Maps of strong ionospheric events, with  $S_4$  index greater than 0.2, for September 2001 (left top panel), September 2002 (right top panel), September 2003 (left bottom panel), January 2004 (right bottom panel). The circles show the geographical position of the tangent point T (Fig. 2.1). The number of CHAMP RO events with strong amplitude variations is diminishing with time; see also *Wickert et al.* 2004.

This may correspond to a decrease in the level of solar activity. One interesting fact is the seasonal displacement of the region with intense ionospheric events in the south and north directions during the periods from May-July (Fig. 2.7, top panel) - September 2001, (Fig. 2.6, top panel), and May-July - December 2001 (Fig. 2.7, top and bottom panels). The number of intense ionospheric events increases in the North Polar Region with time changing from May – July 2001 to November – December 2001. Also the number of strong ionospheric events increases in the south equatorial region for the same time interval. These changes indicated two important mechanisms governing the ionospheric disturbances. The first one is connected with processes of ionizations caused by energetic electrons in the Polar Regions; the second is due to

solar radiation. The influence of solar radiation has a seasonal

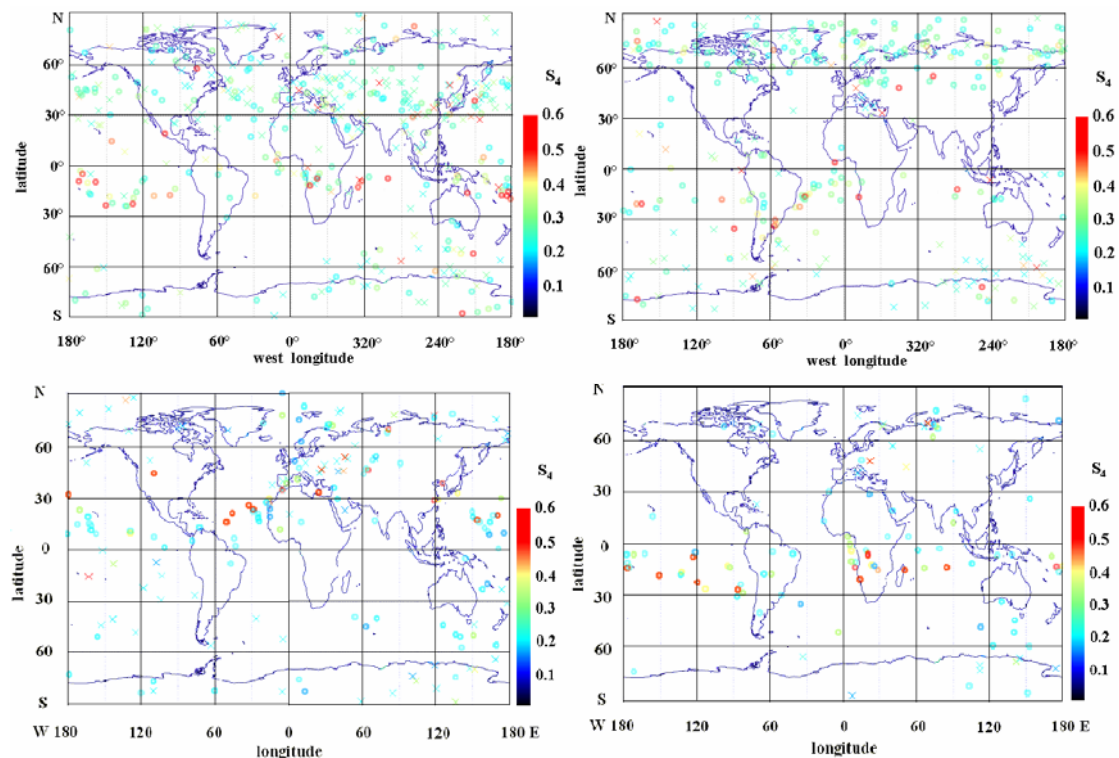


Fig. 2.7. Seasonal dependence of the global distribution of CHAMP RO events with strong amplitude variations (with magnitude of  $S_4$  index greater than 0.2) for periods May 14 –July 14, 2001, (left top panel), November–December 2001 (right top panel), October 2003 (left bottom panel), April 2004 (right bottom panel). The day time events are marked by crosses (local time 08 – 20 hours), the night-time events are indicated by circles (local time 20 – 08 hours), see also *Wickert et al.* 2004.

character because ionization in the ionosphere increases in the summer periods. It follows from analysis of data shown in Fig. 2.6, 2.7 that the seasonal, geographical and temporal distributions of the CHAMP RO events with high  $S_4$  index values observed during the years 2001-2003 indicate their dependence on solar activity. The number of RO events with  $S_4$  index higher than 0.2 is a good indicator of the ionospheric disturbances.

The possible mechanism of this dependence is the electron ionization, which is more concentrated in the Polar Regions and strongly influenced by the solar activity.

This follows from results of measurements made by PEM instrument onboard UARS satellite shown in Fig. 2.8, 2.9.

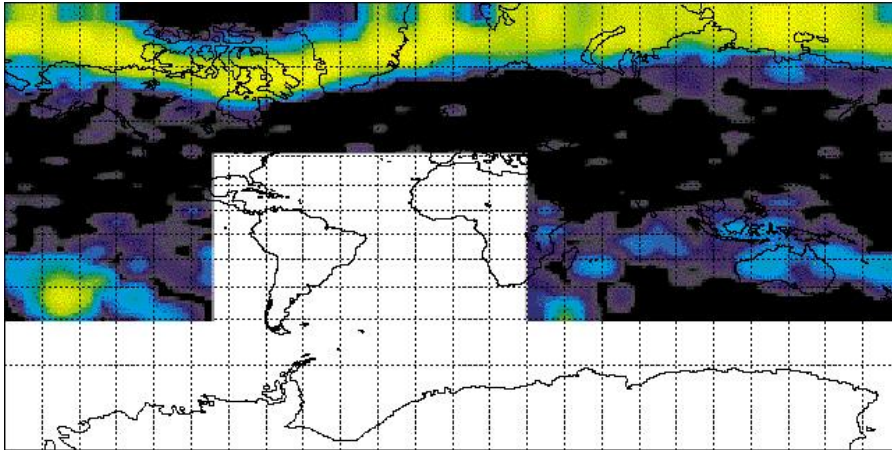


Fig. 2.8. The atmospheric ionization rate measured by PEM near the peak of solar cycle 22. The ionization is caused by fast downward-moving electrons from the magnetosphere impacting air molecules. Green and yellow present larger amounts of ionization; blue and black present smaller amounts of ionization. Published on website address <http://code916.gsfc.nasa.gov/Public/Analysis/UARS/urap/home.html>.

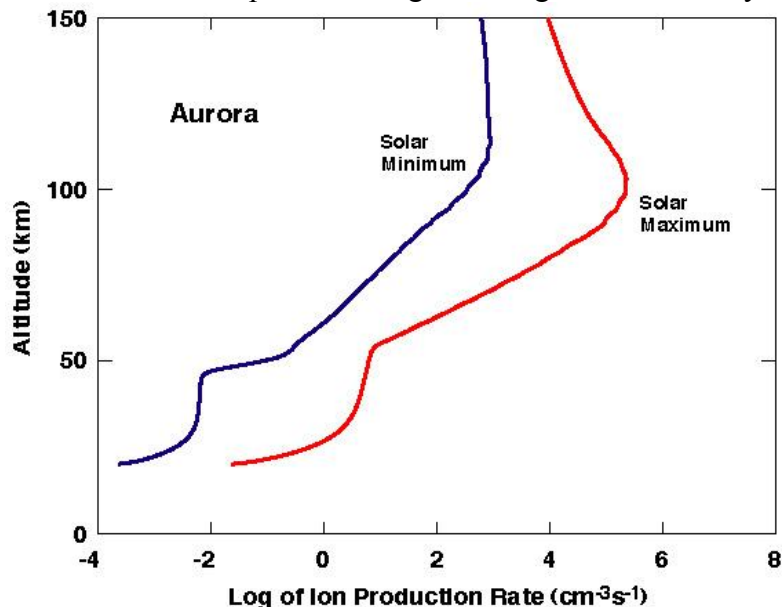


Fig. 2.9. The change in ion production rate from energetic particles as measured by PEM over an 11-year solar cycle. Fast downward-moving electrons from the magnetosphere create ions. The ion production rate varies by a factor of 50 to 200 near solar minimum (blue line) to near solar maximum (red line). The high-energy electrons can cause ozone decreases in the polar mesosphere by producing nitrogen and hydrogen radicals. Published on the website address <http://code916.gsfc.nasa.gov/Public/Analysis/UARS/urap/home.html>.

In Fig. 2.8, obtained by UARS research team (published at the website address

<http://code916.gsfc.nasa.gov/Public/Analysis/UARS/urap/home.html>) the atmospheric

ionization rate measured by analyzer PEM installed on the UARS satellite is shown

for the time near the peak of solar cycle 22 (1992). The ionization is caused by fast

downward-moving electrons from the magnetosphere impacting air molecules. Green and yellow colors in Fig. 2.8 present larger amounts of ionization; blue and black colors mark the smaller amounts of ionization. It is seen in Fig. 2.8 that the ionization is mainly concentrated in the Polar Region and near the geomagnetic equator.

In Fig. 2.9 the temporal behavior of the ionization rate by fast electrons is shown for period of maximum and minimum of solar activity. The ion production rate varies by a factor of 50 to 200 near solar minimum (blue line) to near solar maximum (red line). The data shown in Fig. 2.8, 2.9 are supporting the main conclusion following from analysis of the geographical and temporal distribution of the RO event with strong amplitude variations. The ionospheric disturbances which are the cause of the strong RO amplitude variations are developing because two mechanisms: (1) ionization owing to the fast electron moving in downward direction from the magnetosphere and (2) solar radiation. The considered data reveal effectiveness of the RO amplitude variations for estimation of the parameters of the ionospheric disturbances and their localization. Thus the amplitude part of the RO signals can be considered as a radio hologram, which is appropriate for finding the spatial distribution of the electron density and for localization of the ionospheric disturbances.

### 3. INFORMATIONAL CONTENT OF THE PHASE PART OF RO HOLOGRAM

#### 3.1. CONNECTION BETWEEN THE PHASE OF RO SIGNALS AND TEMPERATURE VERTICAL PROFILES

In the case of spherical symmetric medium the RO signals propagate in the RO plane GOL, and the RO ray can be described by a plane curve GTL with constant impact parameter  $p$ . The straight line GDL is the ray trajectory in free space with the free space impact parameter  $p_s$  (Fig. 3.1).

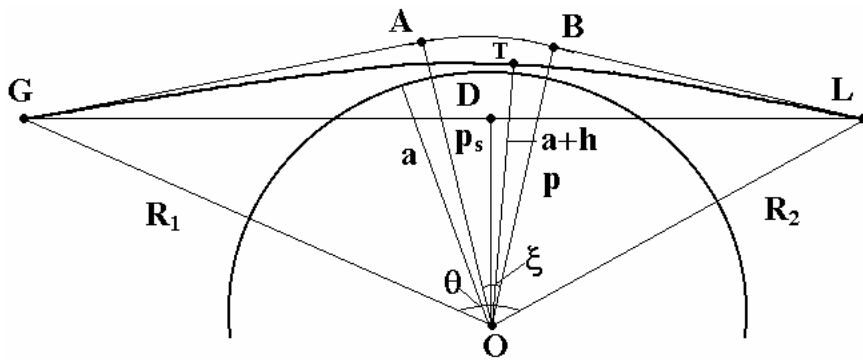


Fig. 3.1. Ray path configuration in a spherical symmetric media during a RO experiment.

The phase path excess  $\Phi(p)$  associated with the RO ray GTL (Fig. 3.1) can be presented in the form:

$$\Phi(p) = L(p) + \kappa(p) + \delta(p); \quad (3.1)$$

$$\delta(p) = (n^2(R_2)R_2^2 - p^2)^{1/2} + (n^2(R_1)R_1^2 - p^2)^{1/2} - [(R_2^2 - p^2)^{1/2} + (R_1^2 - p^2)^{1/2}], \quad (3.2)$$

$$L(p) = (R_2^2 - p^2)^{1/2} + (R_1^2 - p^2)^{1/2} - [(R_2^2 - p_s^2)^{1/2} + (R_1^2 - p_s^2)^{1/2}] + p\xi(p), \quad (3.3)$$

$$\xi(p) = \sin^{-1}(p/n(R_1)R_1) + \sin^{-1}(p/n(R_2)R_2) - [\sin^{-1}(p_s/R_1) + \sin^{-1}(p_s/R_2)], \quad (3.4)$$

$$\kappa(p) = -\int_{r_o}^{R_2} n'(r)/n (n^2 r^2 - p^2)^{1/2} dr - \int_{r_o}^{R_1} n'(r)/n (n^2 r^2 - p^2)^{1/2} dr, \quad (3.5)$$

where  $\delta(p)$  is the local refractivity part of the phase path excess depending on the plasma density at points G and L,  $\delta(p)=0$ , if the refraction indexes  $n(R_2)$ ,  $n(R_1)$  at the point G and L are equal to unity;  $p_s$  is the impact parameter corresponding to the free

space ray GDL (Fig. 3.1),  $L(p)$  is the geometrical part of the phase path excess equal to the difference between the geometrical lengths of the curve GABL and straight line GDL (Fig. 3.1),  $\kappa(p)$  is the main refractivity part of the phase path excess depending only on the vertical distribution of the refractivity. The main refractivity part of the phase path excess  $\kappa(p)$  is connected with the bending angle  $\xi(p)$  by a relationship

$$-d\kappa(p)/dp = \xi(p) \quad (3.6)$$

The refraction angle  $\xi(p)$  is connected with the central angle  $\theta$  by equation

$$\theta = \pi + \xi(p) - \sin^{-1} p/[n(R_1)R_1] - \sin^{-1} p/[n(R_2)R_2], \quad (3.7)$$

Under assumption  $n(R_1) = n(R_2) = 1$ ,  $\delta(p) = 0$ , and equations (3.1), (3.3), (3.4), (3.6), (3.7) can be reduced to system of the relationships

$$\Phi(p) = (R_2^2 - p^2)^{1/2} + (R_1^2 - p^2)^{1/2} - [(R_2^2 - p_s^2)^{1/2} + (R_1^2 - p_s^2)^{1/2}] + p\xi(p) + \kappa(p); \quad (3.8)$$

$$\xi(p) = \sin^{-1}(p/R_1) + \sin^{-1}(p/R_2) - [\sin^{-1}(p_s/R_1) + \sin^{-1}(p_s/R_2)], \quad (3.9)$$

$$\kappa(p) = \int_p^{\infty} \xi(x) dx \quad (3.10)$$

Equations (3.8)-(3.10) contain the measured function  $\Phi(p)$ , which is the phase path excess at the combined frequency  $F_0$  produced in the CHAMP phase data after usual method of the ionospheric correction:

$$\Phi(p) = [f_1^2 \Phi_1(t) - f_2^2 \Phi_2(t)] / (f_1^2 - f_2^2) \quad (3.11)$$

where  $\Phi_1(t)$ ,  $\Phi_2(t)$  are the phase path excesses measured at frequencies  $f_1$  and  $f_2$ .

Geometrical parameters  $\theta$ ,  $p_s$ ,  $R_1$ ,  $R_2$  are known precisely from orbital data. As a consequence, the relationships (3.8)-(3.10) can be used for determination of the refraction angle  $\xi(p)$  as a function of the impact parameter  $p$  under assumption of one-ray propagation in the atmosphere. This assumption is usually valid for the upper and middle stratosphere when the ionospheric conditions are quiet.

Usual way to obtain the temperature vertical profile consists in using the Doppler frequency  $F_d$  found by temporal differentiating the phase path excess (eikonal)  $\Phi(p)$  (e.g., *Pavel'yev et al.* 2002(a)):

$$F_d = \lambda^{-1} d\Phi(p)/dt = \lambda^{-1} [pd\theta/dt + R_1 dR_1/dt (R_1^2 - p^2)^{-1/2} + R_2 dR_2/dt (R_2^2 - p^2)^{-1/2}] \quad (3.12)$$

where  $\lambda$  is the wavelength. Equation (3.12) can be written for the free space path GDL having the impact parameter  $p_s$ :

$$F_{ds} = \lambda^{-1} d\Phi_s(t)/dt = \lambda^{-1} [p_s d\theta/dt + R_1 dR_1/dt (R_1^2 - p_s^2)^{-1/2} + R_2 dR_2/dt (R_2^2 - p_s^2)^{-1/2}] \quad (3.13)$$

where  $\Phi_s(p_s)$  is the path length GDL (Fig. 3.1)

From (3.12), (3.13) one can obtain equation to determinate  $p - p_s$  using measured difference  $\Phi(p) - \Phi_s(p_s)$

$$\begin{aligned} \Delta F = F_d - F_{ds} = d[\Phi(p) - \Phi_s(p_s)]/dt = \lambda^{-1} \{ (p - p_s) d\theta/dt + R_1 dR_1/dt [(R_1^2 - p^2)^{-1/2} - (R_1^2 - p_s^2)^{-1/2}] \\ + R_2 dR_2/dt [(R_2^2 - p^2)^{-1/2} - (R_2^2 - p_s^2)^{-1/2}] \} \end{aligned} \quad (3.14)$$

Equation (3.14) can be solved using known values of  $\Delta F$ ,  $p_s$ ,  $R_1$ ,  $R_2$  to find the difference  $p - p_s$ . The refraction angle  $\xi(p)$  can be found from Taylor expansion of the right part of equation (3.9) (*Liou and Huang*, 2000). Abel' transform may be applied to find the vertical distribution of the refractive index  $n(h)$  from known function  $\xi(p)$  (*Hocke*, 1997):

$$\begin{aligned} \ln[n(h)] = -1/\pi \int_p^\infty \xi(x) \ln[x/p + (x^2/p^2 - 1)^{1/2}] dx, \quad n(h) = 1 + N(h) \cdot 10^{-6}, \\ h = p/n(h) - a, \end{aligned} \quad (3.15)$$

where  $N(h)$  is the refractivity as a function of height, and  $a$  is the distance between the center of local spherical symmetry (point O in Fig. 2.1) and the Earth surface in the RO region. Equations (3.15) give the refractivity  $N(h)$  (N-units) and height  $h$  from the phase part of the radio hologram  $\Phi(p)$  and orbital data, which are described as functions of time  $\theta$ ,  $p_s$ ,  $R_1$ , and  $R_2$ .

The temperature vertical profile  $T(h)$  can be obtained using the refractivity profile  $N(h)$  if initial values  $T(h_\infty)$ ,  $N(h_\infty)$  are known at some height  $h_\infty$ :

$$T(h) = T(h_\infty)N(h_\infty)N^{-1}(h) + T_x N^{-1}(h) \int_{h_\infty}^h N(h) dh \quad (3.16)$$

$$T_x = gM/k \quad (3.17)$$

where  $g$  is the gravity acceleration depending on height  $h$  and latitude  $\varphi$

$$g = g_o(1 - 0.0002644 \cos^2 \varphi)(1 - 0.000314h); \quad g_o = 9.80616 \text{ m/sec}^2, \text{ if } \varphi = 45^\circ, h = 0 \text{ km}, \quad (3.18)$$

$M$  is the molecular mass of dry air  $M = kR$ ,  $R$  is the gas constant,  $R = 2.8704 \cdot 10^6$  [erg/gK<sup>-1</sup>],  $k$  is the Boltzmann constant. It follows from (3.17), (3.18) that the parameter  $T_x$  is equal to

$$T_x = 34.16 \text{ g/g}_o \text{ K/km}. \quad (3.19)$$

Shortcoming of the described method is increasing of noise owing to differentiating when the Doppler frequency is evaluated on known dependence of the phase path excess  $\Phi(p)$ . This difficulty prevents obtaining the vertical temperature profile in the height interval 35-65 km without auxiliary model describing expected dependence of the temperature on height in the stratosphere. For example, ECMWF model may be used to obtain the vertical temperature profiles at the heights above 35 km by method of the statistical optimization (*Sokolovskiy and Hunt, 1996, Rocken et al. 1997, Hocke, 1997*).

Alternative approach consists in numerical solution of the system of equations (3.8) – (3.10), (3.16) which exclude the operation of differentiation of the phase path excess.

### 3.2. COMPARISON OF THE TEMPERATURE PROFILES OBTAINED BY THE TRADITIONAL PHASE METHOD AND UPGRADED PHASE METHOD

As shown earlier (*Pavelyev, 1990*), there exist many solutions of a given inverse problem. These solutions have different values of the instability index and different forms of the analytic presentation. The task consists in finding such analytical or numerical method of solution of the nonlinear system (3.8)-(3.10), (3.16), which has minimal value of the instability index and produces minimal level of systematic and statistical errors in the refraction angle  $\xi$ , impact parameter  $p$ , refractivity  $N(h)$ , and temperature  $T(h)$ . For solution of the system (3.8)-(3.10), (3.16) we used an iteration method based on the initial approximation of the functional dependence  $\xi(p)$ . For iterations we used the radio physical model of the refractivity described earlier (*Pavelyev, 1998*) under control of the regime of one- ray propagation.

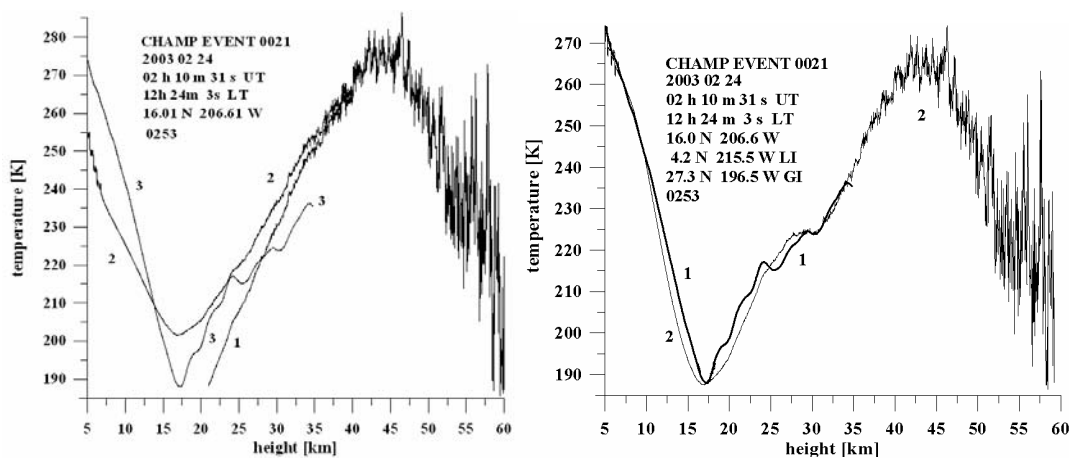


Fig. 3.2. Left panel: comparison of two approximate solution of the system (3.8)-(3.10), (3.16), (3.16) (curves 1, 2) with temperature vertical profile (curve 3) obtained from the phase RO data by CHAMP scientific team (Internet web site: <http://www.gfz-potsdam.de/gasp>). Right panel: comparison of the temperature vertical profile obtained from the phase RO data by CHAMP scientific team (curve 1) with the final solution of the system (3.8)-(3.10), (3.16), (3.16) (curve 2).

The RO event number, geographical co-ordinates and time of RO experiment are given in the insert. The bottom line in the insert indicated the rms of the amplitude variations  $\sigma = [ \langle (A(t) - \langle A \rangle)^2 \rangle / \langle A \rangle^2 ]^{1/2}$  multiplied by 10000.  $S_4$  index was equal to 0.05; systematic ionospheric influence has been observed in the phase path excess at frequency F0 in the 80-90 km interval.

Results of solution of the system (3.8) - (3.10), (3.16) are shown in Fig. 3.2-3.7 for CHAMP RO events occurred on February 24, 2003. Two temperature profiles obtained from approximate solutions of the system (3.8)-(3.10), (3.16) are shown in Fig. 3.2 (left panel) by curves 1 and 2. Both curves coincide in 40-60 km interval. Discrepancy between the curve 1 and 2 is increasing below 35 km. The curve 2 has better agreement than curve 1 with curve 3 obtained by CHAMP scientific team by means of analysis of the phase data. The best approximation of the curve 2 to curve 3 is observed in the 21 – 25 km interval. The difference between curve 2 and 3 changes in the 0-15 K interval near tropopause and then varied from 0 K up to –18--20 K in the height interval 5-14 km. We conclude from consideration of the Fig. 3.2 (left panel) that the second iteration is better than the first one for obtaining the vertical temperature profiles in the 35-60 km interval. The CHAMP temperature profile obtained from analysis of the phase data can be used in the height interval below 35 km as a tool for parameterization and correcting the results of UPM method. In the Fig. 3.2 (right panel) the results of corrected temperature profile obtained by UPM method are shown. Curve 1 corresponds to the CHAMP phase retrieval; curve 2 describes the corrected results obtained by UPM method. It is seen in Fig. 3.2, right panel, that the corrected UPM temperature profile is in good correspondence with the CHAMP retrievals in the 5-35 km interval. Above 35 km the UPM temperature profile is displaced as a result of correction by value of about 10 K. It follows, that the traditional phase method is needed for excluding systematic errors in the UPM method, which are possible owing to the ionospheric influence.

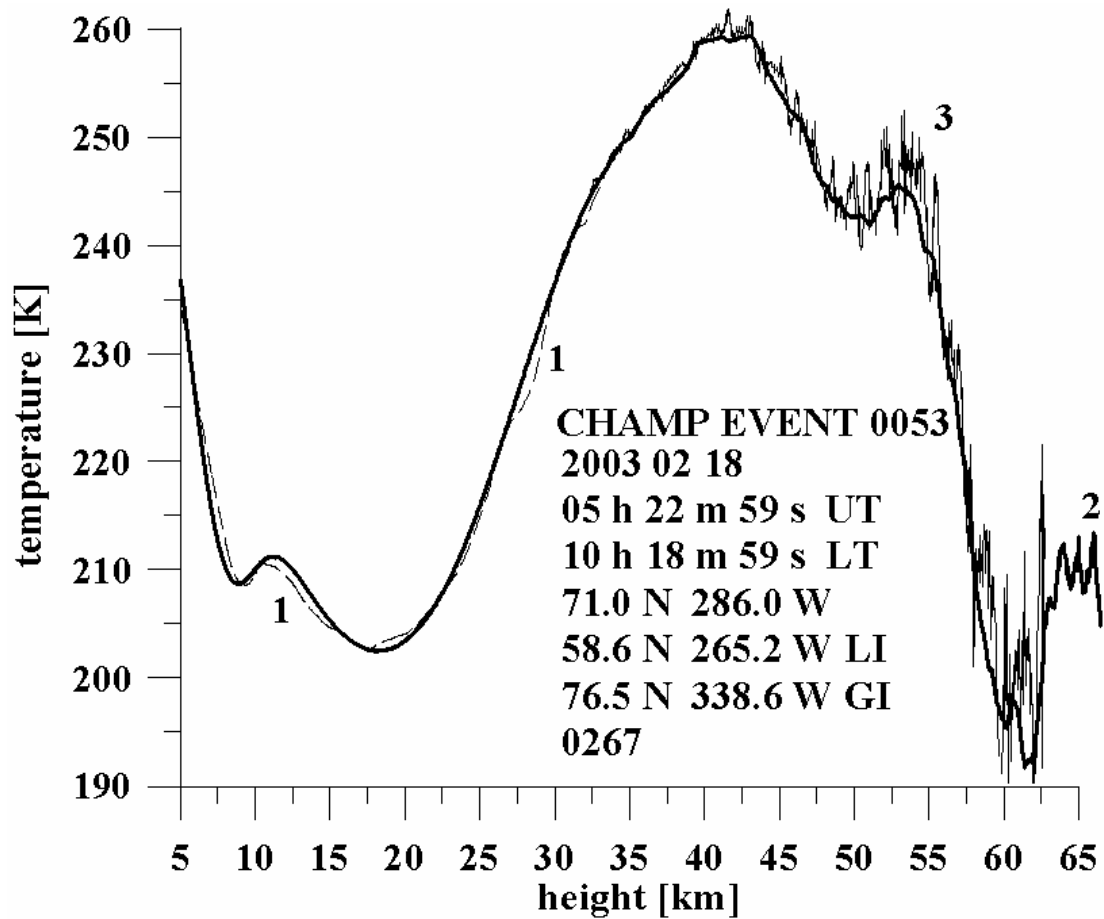


Fig. 3.3. Comparison of the temperature vertical profile (curve 1) obtained from the CHAMP RO phase data (Web site: <http://isdg.gfz-potsdam.de/champ>) applying the Upgraded Phase Method (UPM) (curve 3). Curve 2 indicates results of the temperature retrieval obtained by Upgraded Phase Method with Averaging (UPMA). The insert includes information on the local and universal times (LT, UT) and information of the geographical location of the RO event. Also the geographical coordinates of the exit and entrance point of the RO ray trajectory in the F-layer of the ionosphere at the height 280 km are shown.  $S_4$  index of the amplitude variations was equal to 0.05, which corresponds to the case of slightly perturbed ionosphere.

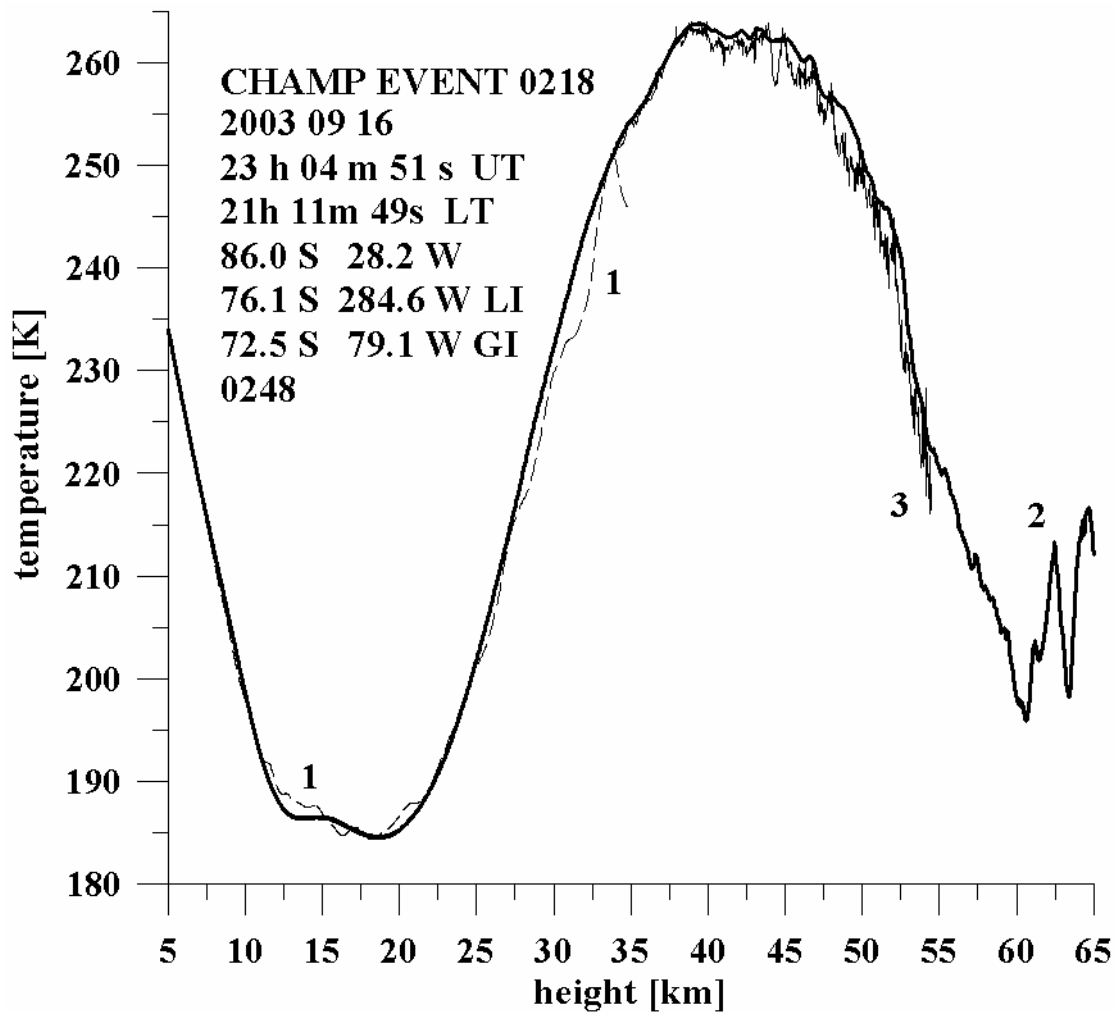


Fig. 3.4. Temperature profile in the upper troposphere and stratosphere near the South Pole (CHAMP RO event 0218, September 16, 2003). Good correspondence of the results obtained by upgraded method (curve 2) with CHAMP data (curve 1) is seen in the height interval 5-35 km. Near the tropopause the difference between the traditional phase analysis (curve 1) and upgraded method (curve 2) is about of 1-2 K.  $S_4$  index of the amplitude variations was equal to 0.05, which corresponds to the case of slightly perturbed ionosphere.

The vertical temperature profiles for north and south Polar Regions are shown in Fig. 3.3, 3.4, respectively. Curve 1 corresponds to CHAMP phase analysis, curve 2 relates to the upgraded phase method. The boundary condition, which has been used to obtain the temperature profiles, has been chosen at height 75 km,  $T_{75} = 200$  K. As follows from approximate estimation deflections in the magnitude  $T_{75}$  by  $\pm 50$  K introduces the temperature changes  $\pm 5$  K and  $\pm 1$  K at altitude 60 km and 45 km, respectively. These values are essentially below the level of the statistical error at the considered altitudes.

The increasing of the random error from  $\pm 0.3$  K (at level 33 km) up to  $\pm 3$  K (at level 60 km) is clearly seen in Fig. 3.3, 3.4. The coincidence between both methods can be seen in the height interval 5-35 km. The distinction between two methods is achieved 1-5 K at the heights 5-35 km in both Fig. 3.3 and Fig. 3.4.

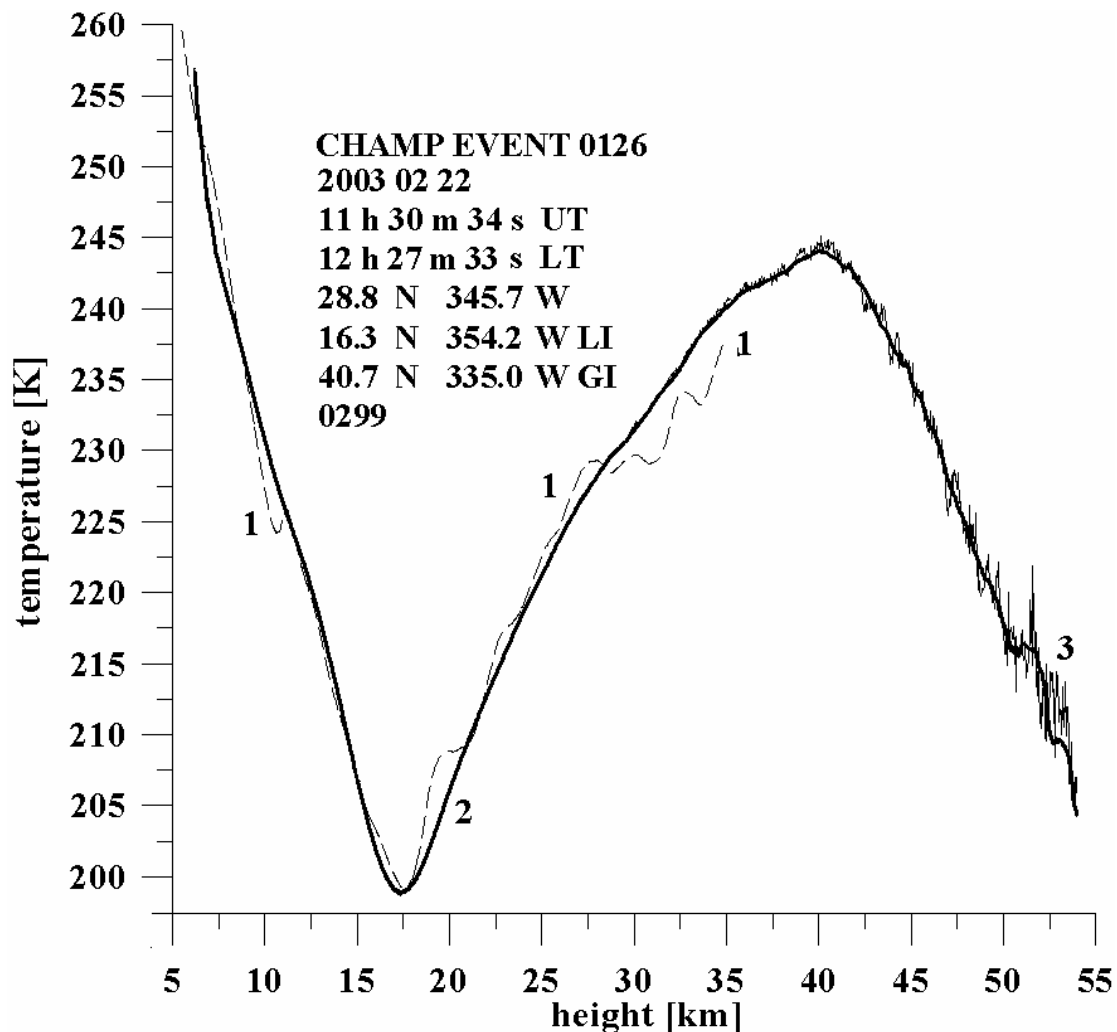


Fig. 3.5. Temperature profile in the upper troposphere and stratosphere in the north tropical area (CHAMP RO event 0126, February 22, 2003). Good correspondence of the results obtained by upgraded method (curve 2) with CHAMP data (curve 1) is seen in the 18-35 km interval. Near the tropopause the difference between the traditional phase analysis (curve 1) and upgraded method (curve 2) is about of 1-4 K. In the middle troposphere the difference between two methods is about of 2-3 K.  $S_4$  index of the amplitude variations was equal to 0.06, which corresponds to the case of slightly perturbed ionosphere.

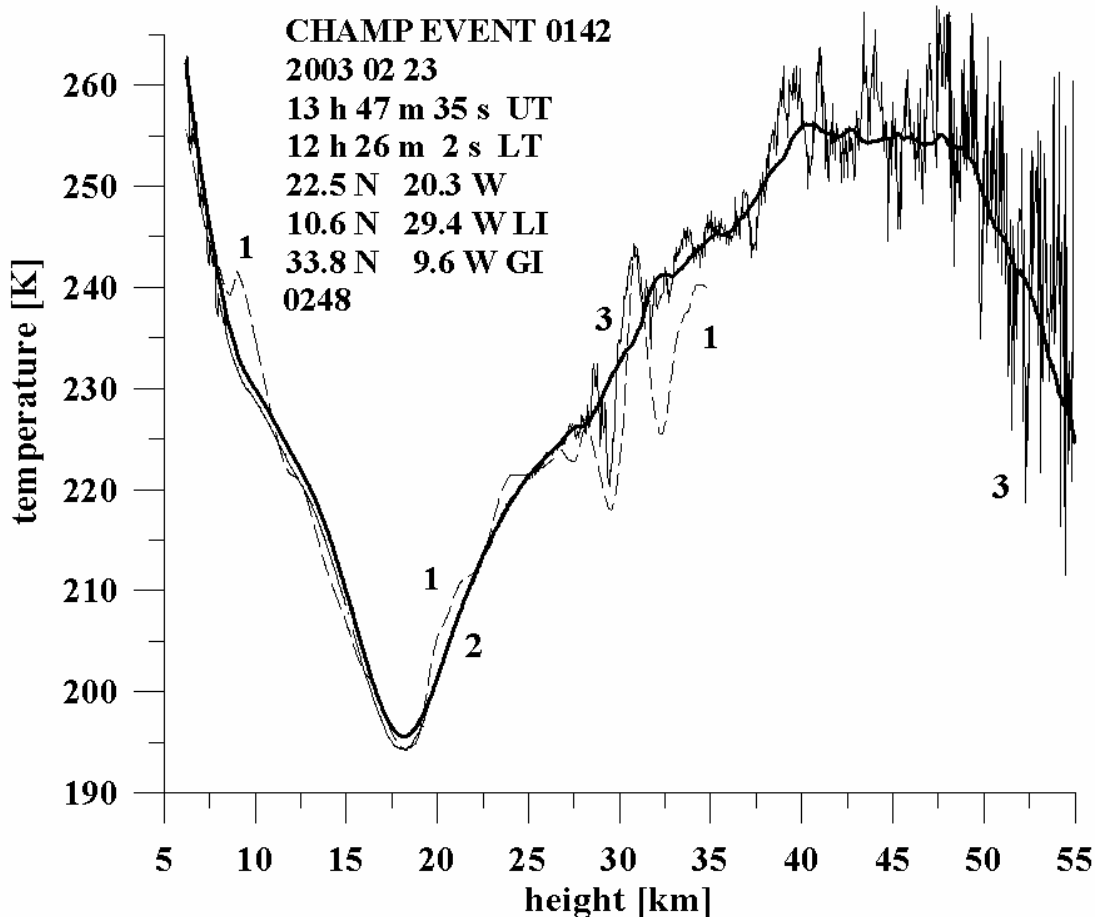


Fig. 3.6. Temperature profile in the upper troposphere and stratosphere in the north tropical area (CHAMP RO event 0142, February 23, 2003). Good correspondence of the results obtained by upgraded method (curve 2) with CHAMP data (curve 1) is seen in the 12-35 km interval. Near the tropopause the difference between the traditional phase analysis (curve 1) and upgraded method (curve 2) is about of 2 K. In the middle troposphere the difference between two methods is about of 5-6 K.  $S_4$  index of the amplitude variations was equal to 0.05, which corresponds to the case of slightly perturbed ionosphere.

In Fig. 3.5, 3.6 the temperature profiles obtained by conventional (curve 1) and upgraded phase methods (curve 2) are shown for two north tropical regions. Good correspondence of the results obtained by upgraded method (curve 2) with CHAMP data (curve 1) is seen in the 6-32 km interval. Near the tropopause the difference between the traditional phase analysis (curve 1) and upgraded method (curve 2) is about of 1-2 K. In the middle troposphere the difference between two methods is about of 1-5 K. As follows from data in Fig. 3.3-3.6 the UPM method has a promise to be effective to obtain temperature profiles in the upper stratosphere. The

conventional methods are needed in auxiliary model to obtain reliable results in the upper stratosphere using statistical optimization approach (*Sokolovskiy and Hunt, 1996*). Hence UPM can be used as a method for prolongating the temperature profiles obtained by conventional methods to the upper stratosphere.

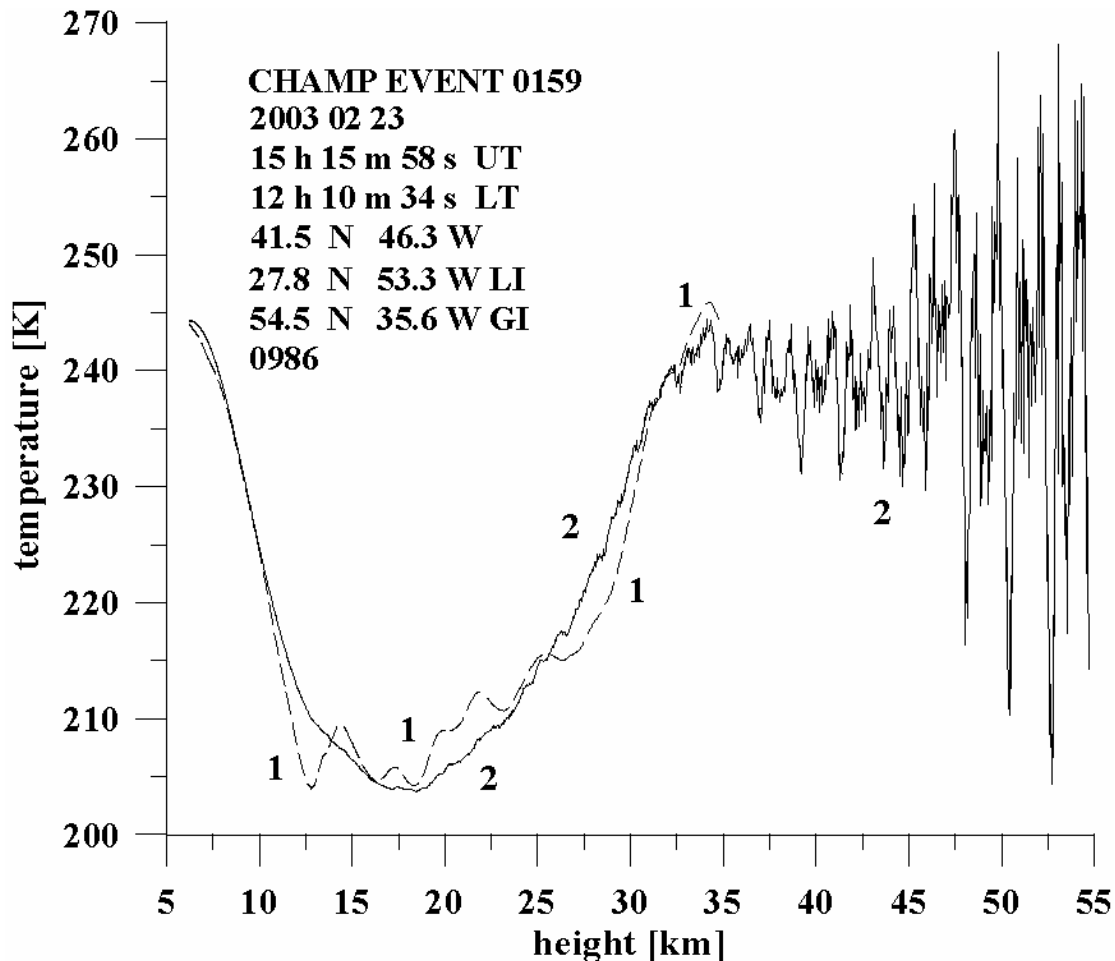


Fig. 3.7. Temperature profile in the upper troposphere and stratosphere in the north middle latitude (CHAMP RO event 0159, February 23, 2003). Good correspondence of the results obtained by upgraded method (curve 2) with CHAMP data (curve 1) is seen in the 6-35 km interval. Near the tropopause the difference between the traditional phase analysis (curve 1) and upgraded method (curve 2) is about of 3-5 K. The sharp variations in temperature above 35 km are connected with spikes in the phase at the frequency F2.  $S_4$  index of the amplitude variations was equal to 0.2, which corresponds to the case of the disturbed ionosphere.

The UPM method depends on the ionospheric correction and on the quality of the phase data at the frequencies F1 and F2. In Fig. 3.7 an example is given when the phase path excess at the second frequency has been interfered by quasi-periodical sharp spikes. In this case the UPM method gives the result shown by curve 2 in Fig.

3.7. Below 35 km the influence of the spikes on the temperature profile is practically not seen in the CHAMP team result (curve 1) and in the result obtained by UPM method (curve 2). However above 35 km the amplitude of quasi-periodical temperature variations is growing thus indicating the role of systematic errors in the phase path inversion by UPM method. Thus results shown in Fig. 3.7 are useful for estimation systematic errors caused by specific receiver interferences.

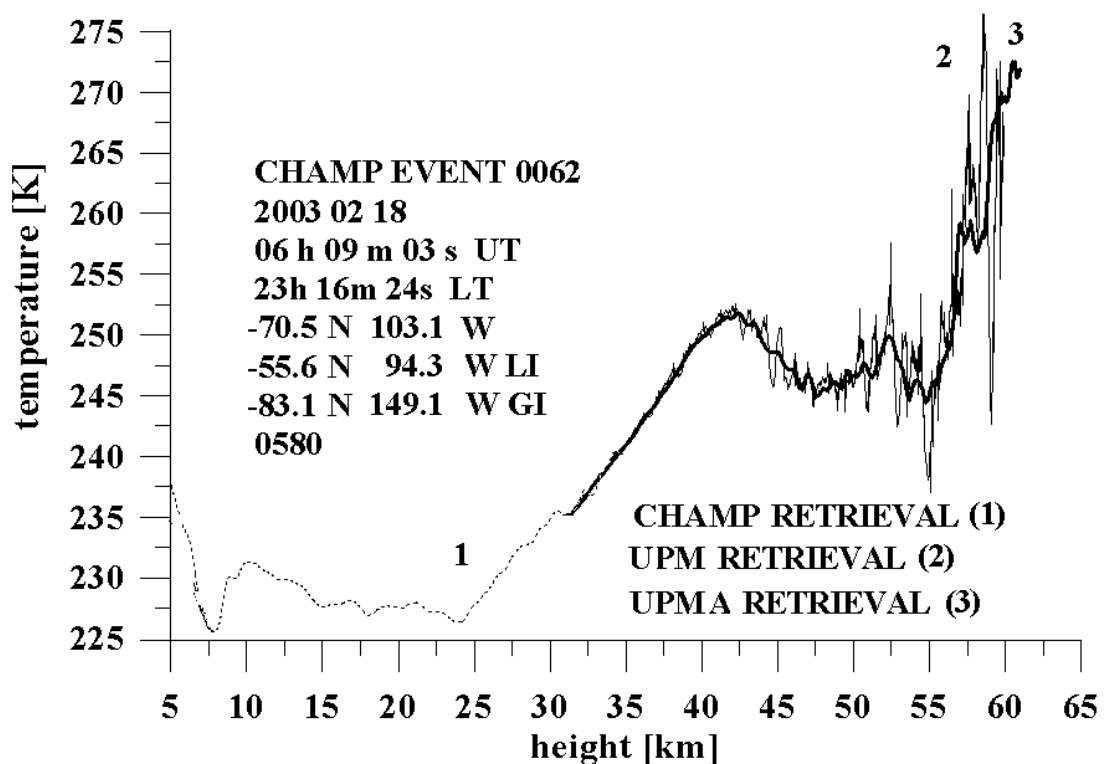


Fig. 3.8. The temperature vertical profile (curve 1) obtained from the phase RO data by CHAMP scientific team, UPM (curve 2) and UPMA methods (curve 3). RO event number, geographical co-ordinates and time of RO experiment are given in the insert. The geographical co-ordinates of the points of entrance and exit of the RO ray trajectory in the F-layer of the ionosphere are shown in the second and third line from bottom in the insert.  $S_4$  index of the amplitude variations was equal to 0.12, which corresponds to the case of the perturbed ionosphere.

Example of the phase inversion by UPM and traditional method is given in Fig. 3.8.

The curve 1 corresponds to the CHAMP temperature restoration; curve 2 describes the UPM and UPMA results. As seen in Fig. 3.8, the results of both retrievals are the same in the 30-35 km interval. However above 35 km the UPM method gives

additional information on the temperature profile showing the minimums and maximums in the stratospheric temperature distribution. UPM and UPMA methods indicate the maximum in temperature profile at 42 km equal to 252 K, the minimum at the height 47.5 km equal to 246 K and then demonstrate increasing of the temperature up to value 273 K at altitude 62 km. Thus UPM method offers a promise as a processing tool for RO data analysis in the current and future missions.

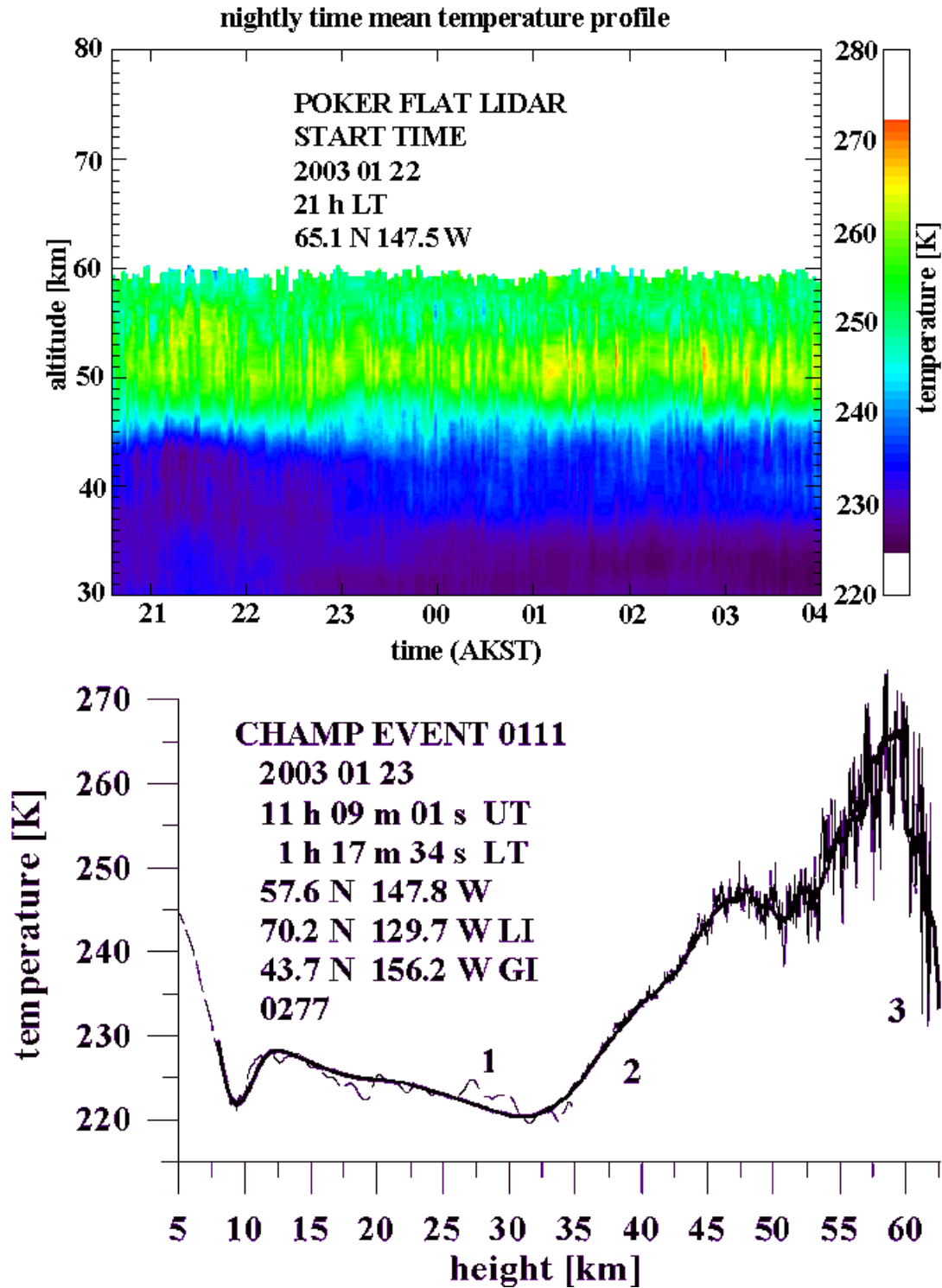


Fig. 3.9. Comparison of the temperature profiles measured by Earth-based lidar in Poker Flat (Alaska) (upper panel) on January 22-23, 2003, and CHAMP temperature retrieval (bottom panel). Curve 1 indicates the temperature in the 5-35 km interval obtained from analysis of the phase data by CHAMP Science Team. Curve 2 and 3 show the temperature profile obtained by UPM and UPMA retrieval.

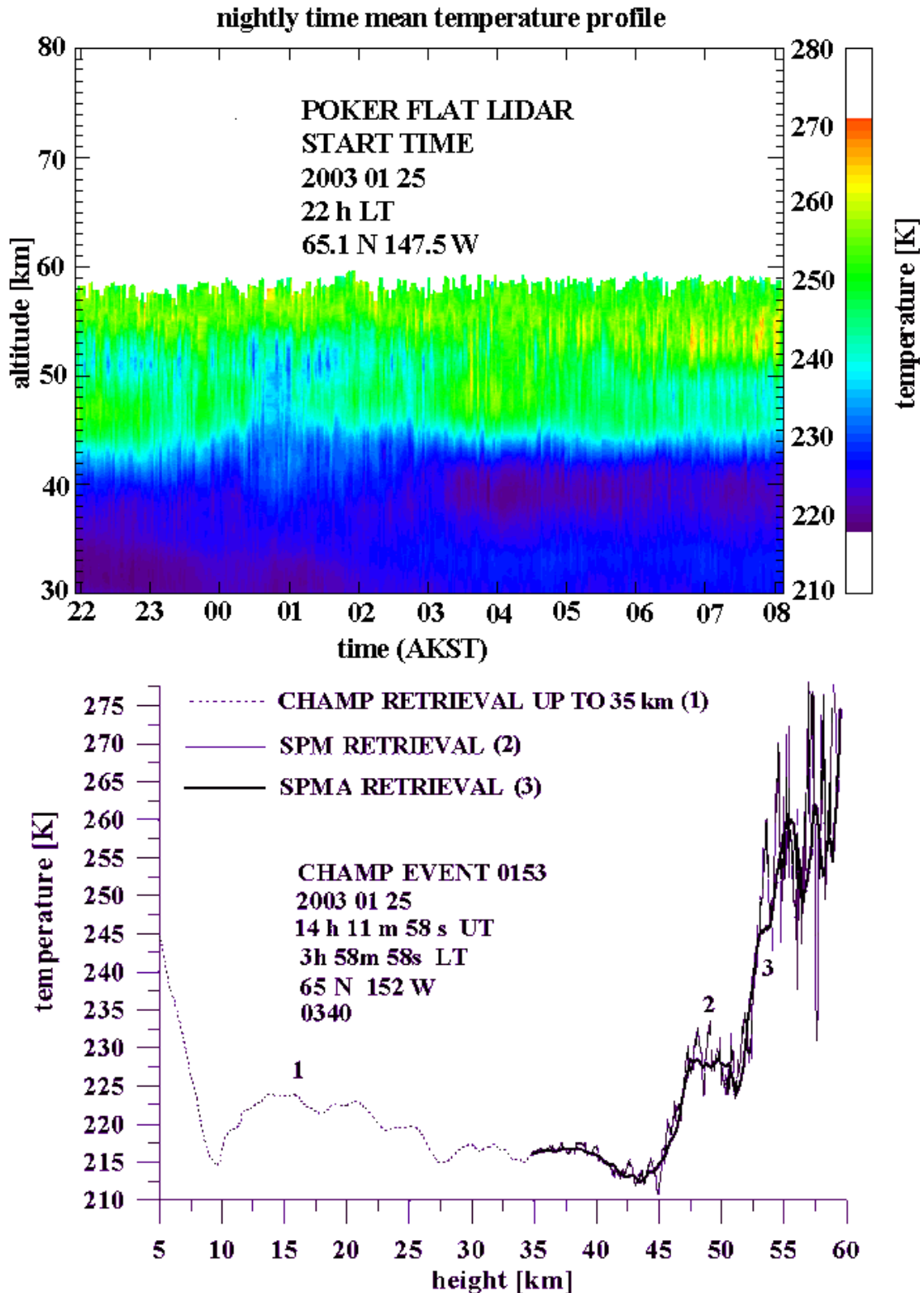


Fig. 3.10. Comparison of the temperature profiles measured by Earth-based lidar in Poker Flat (Alaska) on January 25-26, 2003, (upper panel) and CHAMP temperature retrieval (bottom panel). The designations are the same as in Fig. 3.9.

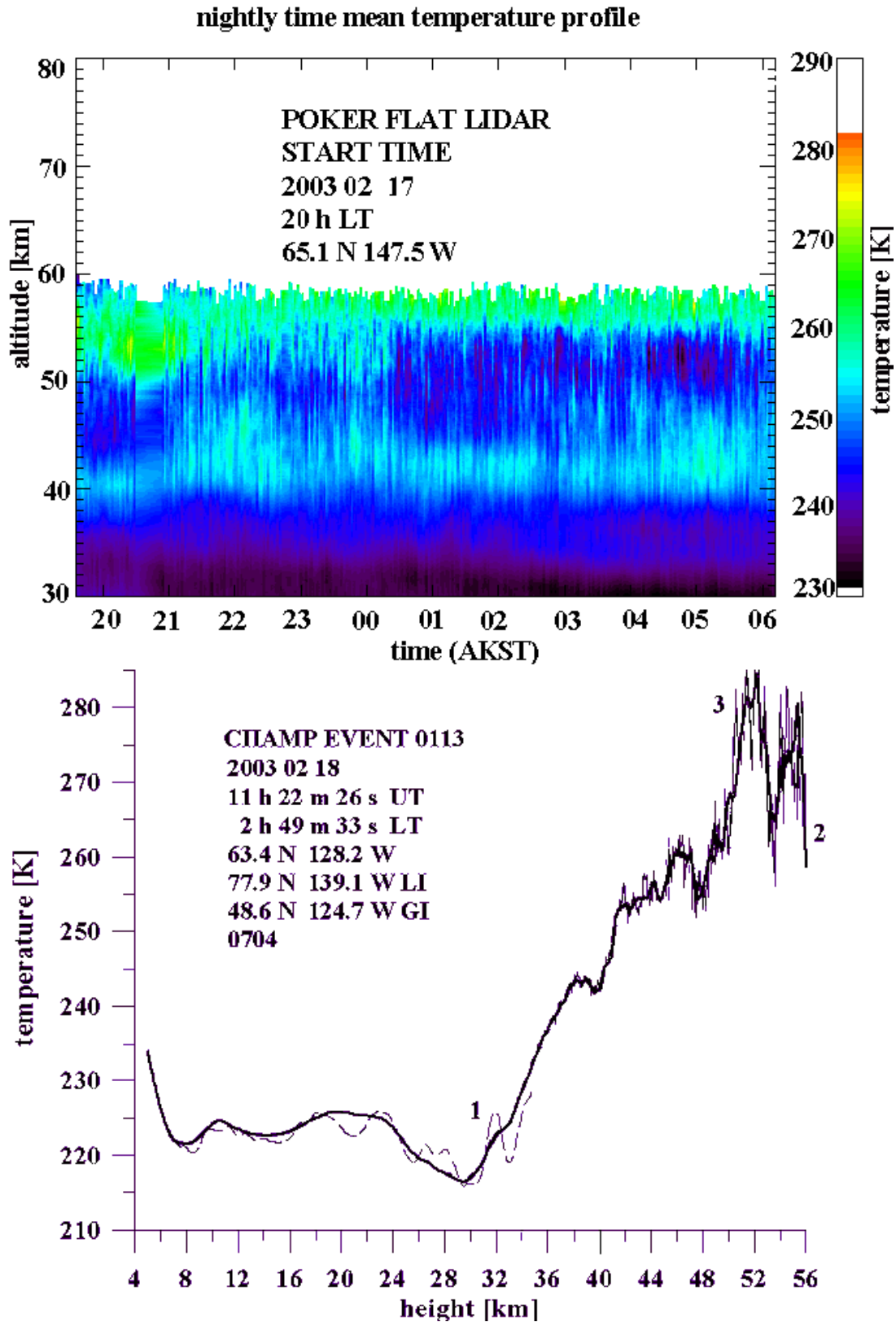


Fig. 3.11. Comparison of the temperature profiles measured by Earth-based lidar in Poker Flat (Alaska) on February 17-18, 2003, (upper panel) and CHAMP temperature retrieval (bottom panel). The designations are the same as in Fig. 3.9.  $S_4$  index of the amplitude variations was equal to 0.14, which corresponds to the case of the disturbed ionosphere.

The results of the CHAMP and UPM retrievals can be compared with Earth-based lidar data. Such a comparison can be made using data shown in Fig. 3.9 – 3.11. In Fig. 3.9-3.11 (bottom panel) curve 1 indicates the temperature in the 5-35 km interval obtained from analysis of the phase data by CHAMP Team. Curve 2 and 3 show the temperature profile relevant to UPM and UPMA retrievals. The upper panel in Fig. 3.9-3.11 demonstrates the temperature profiles in the stratosphere obtained by Earth-based lidar. The location of RO region in Fig. 3.9 was nearly 750 km in the south direction relative to the lidar installation. The time of RO experiments was nearly the same as the lidar data. Despite the difference in the geographical location the temperature profiles obtained by conventional method, UPM method and lidar are very similar. The UPM curve shows temperature increase in the height interval 47-60 km, which corresponds to behavior of the lidar temperature profile in this altitude interval. The maximum in the temperature profile obtained by UPM method is displaced by two km relative to the lidar data in Fig. 3.9.

The location of RO region for the second case (Fig. 3.10) was nearly 250 km in west direction relative to the lidar installation. The time of RO experiments was about 18 hour earlier than the lidar data. Despite this difference in the geographical location and in time the temperature profiles obtained by conventional method, UPM method and lidar are very similar. The UPM curve shows temperature increase in the height interval 47-60 km, which corresponds to behavior of the lidar temperature profile in this altitude interval.

In the third example (Fig. 3.11) the temperature profiles obtained by lidar and UPM methods are compared for the same time, nearly the same latitude, however the RO region is located by 850 km in the east direction relative to the lidar installation. Once again it can be see good correspondence between the CHAMP and lidar data. Thus

UPM method of estimation of the vertical temperature profiles in the stratosphere is a tool for remote sensing control of the stratosphere using GPS RO data.

#### 4. GW PROPAGATION THEORY AND ITS APPLICATION FOR RO MEASUREMENTS OF GW STRUCTURES IN THE EARTH'S ATMOSPHERE

##### 4.1. PROBLEM STATEMENT

RO sounding of the Earth's atmosphere using the radio signals of Global Positioning System (GPS) can be valuable source of information about atmospheric variables. Using measurements of the phase (or frequency) and amplitude perturbations of the signal from the GPS satellite during RO experiments it is possible to retrieve the vertical refractivity profiles. The refractivity profiles are used together with knowledge about the chemical composition of the atmosphere to calculate the profiles of the density, pressure, temperature and water vapor. It is possible to extract from the RO measurements the information about atmospheric winds. The background wind, that exists when pressure gradient forces are balanced by Coriolis forces, is called the geostrophic wind. The geostrophic wind equations (*Pedlosky, 1982*) describe the motion of a parcel of air that is initially moving from a high pressure area to a low pressure area. The motion is sufficiently slow, however, because the Coriolis force deflects the air into a motion that is parallel to the isobars. The RO retrievals of the atmosphere parameter profiles may be used together with the geostrophic wind equations to find the components  $(u_0, v_0, 0)$  of the background wind. The temporary departures from a stable stratified background state can lead to oscillations relative to mean state with periods of minutes or more. These oscillations are atmospheric Gravity Waves (GW).

Internal GW play a main role in the dynamical state and temperature regime of the atmosphere. The wind speed fluctuations and the variations of density, pressure,

and temperature can be caused by GW influence. RO amplitude method is a new tool to estimate the GW activity on a global scale. From the RO amplitude data it is possible to retrieve the density, temperature and pressure variations.

On the base of the linear inviscid theory of GW propagation we will obtain the relations between the characteristics of GW and parameters of dynamical and thermodynamical state of the atmosphere. These relations will be useful and convenient for study of internal GW by RO method.

#### 4.2. PERTURBATIONS OF THERMODYNAMICAL PARAMETERS OF THE ATMOSPHERE AND THEIR CONNECTION WITH THE GW ACTIVITY

RO measurements of the density and temperature variations connected with the internal GW contain the information concerning perturbations of dynamical state of the atmosphere. One of the most important parameters of dynamical state is the horizontal wind velocity. To determine the perturbations of horizontal wind velocity by RO method it is necessary to establish the relation of these perturbations with the measured variations of thermodynamical parameters. Earlier in the report 2 we used a rotating Cartesian co-ordinate system in which the local orientations of the axes are east, north and local zenith, respectively. Let us consider the transform of the projections of the wind velocity perturbation vector  $U_h'$  from the old co-ordinate system  $(x, y, z)$  to new Cartesian co-ordinate system  $(x', y', z)$ . The direction of the  $x'$ -axis is along the horizontal component of the GW propagation vector  $K_h$ . The new system  $(x', y', z)$  is the result of turning of the co-ordinate system  $(x, y, z)$  around  $z$  axis on the angle  $\beta$  in the horizontal  $xy$  plane,  $\beta$  is the angle between the  $x$  axis and  $K_h$  vector. The wave numbers  $k$  and  $l$  determine completely the  $\beta$  angle:

$$\cos\beta = k/(k^2 + l^2)^{1/2} \text{ and } \sin\beta = l/(k^2 + l^2)^{1/2},$$

the projections of the  $\mathbf{U}_h'$  vector in the old basis –  $(u', v')$  are connected with new ones  $(u_n', v_n')$  as follows:

$$u_n' = \cos\beta u' + \sin\beta v', \quad (4.1)$$

$$v_n' = -\sin\beta u' + \cos\beta v', \quad (4.2)$$

where  $u_n', v_n'$  and  $u', v'$  are the complex perturbations of the horizontal wind velocity in the new  $(x', y', z)$  and old  $(x, y, z)$  Cartesian co-ordinate systems respectively.

After substituting in (4.1), (4.2) the magnitudes  $\cos\beta$  and  $\sin\beta$  one obtains:

$$u_n' = [u'k/(k^2 + l^2)^{1/2} + v'l/(k^2 + l^2)^{1/2}], \quad (4.3)$$

$$v_n' = [-u'l/(k^2 + l^2)^{1/2} + v'k/(k^2 + l^2)^{1/2}]. \quad (4.4)$$

It may be noted that  $u_n'$  is the perturbation of the horizontal velocity component along the  $\mathbf{K}_h$  vector, and  $v_n'$  is the perturbation of the horizontal wind velocity component along the constant phase lines of the waves.

Using amplitudes  $A_u$  and  $A_v$  introduced in the report 2 (equations (22) and (23)) one can find:

$$u_n' = [\omega(k^2 + l^2)^{1/2} A_p / (\omega^2 - f^2) \exp(i(kx + ly + mz - \sigma t) + z/(2H))], \quad (4.5)$$

$$v_n' = [-if(k^2 + l^2)^{1/2} A_p / (\omega^2 - f^2) \exp(i(kx + ly + mz - \sigma t) + z/(2H))]. \quad (4.6)$$

Let us analyze the obtained polarization relations (4.5) and (4.6) for the projections  $(u_n', v_n')$  of the vector  $\mathbf{U}_h'$  of the horizontal wind perturbations. These equations show that  $u_n'$  and  $v_n'$  are connected by relationship:

$$(u_n')^2 + (v_n')^2 \omega^2 / f^2 = \omega^2 (k^2 + l^2) |A_p|^2 \exp(z/H) / (\omega^2 - f^2)^2. \quad (4.7)$$

Equation (4.7) shows that the horizontal wind perturbations vector draws an ellipse when the variation in time or height is plotted into hodograph. The major ellipse axis –  $2a$  is located along the  $\mathbf{K}_h$  vector, and the minor axis –  $2b$  lies at the perpendicular direction

along the constant phase lines. The expression for the major and minor semiaxes can be derived from (4.7)

$$a = \omega(k^2 + l^2)^{1/2} |A_p| \exp(z/(2H)) / (\omega^2 - f^2), \quad (4.8)$$

$$b = af/\omega = f(k^2 + l^2)^{1/2} |A_p| \exp(z/(2H)) / (\omega^2 - f^2). \quad (4.9)$$

The values  $a$  and  $b$  define the maximums of the wind velocity perturbations in the directions of  $\mathbf{K}_h$  vector and along the constant phase lines, respectively. Since  $f/\omega < 1$ ,  $b < a$ , and the velocity perturbation maximum in the direction of  $\mathbf{K}_h$  vector (i. e. along the pressure gradient) is more than the maximum of velocity perturbations directed along the constant phase lines which are, at the same time, the pressure perturbation isobars. Therefore, the fluid motion is directed mainly along the pressure perturbation gradient. It follows from equations (4.8) and (4.9) that  $a, b \sim \exp(z/(2H))$  and this means the exponential growth with height of the amplitude of the horizontal projections of the perturbation vector. Since the module of  $\mathbf{U}_h'$  vector is equal to  $|\mathbf{U}_h'| = ((u_n')^2 + (v_n')^2)^{1/2}$  then, using the expressions for  $u_n'$  and  $v_n'$  from (4.5) and (4.6), respectively, one can obtain:

$$|\mathbf{U}_h'| = a[(1 + f^2/\omega^2)/2 + (1 - f^2/\omega^2)/2 \cos(2(kx + ly + mz - \sigma t + \varphi_0))]^{1/2}, \quad (4.10)$$

where  $a$  is defined by (4.8). As it follows from (4.10), the  $|\mathbf{U}_h'|$  values are confined within limits  $a \geq |\mathbf{U}_h'| \geq af/\omega = b$ , and the average value of the  $\mathbf{U}_h'$  vector module over the oscillation period is equal to  $a[(1 + f^2/\omega^2)/2]^{1/2}$ .

Let us consider the special case when the Earth rotation may be ignored, i. e.  $\omega \gg f$ . In this case, as it follows from (4.7),  $v_n' \rightarrow 0$ , and the vector  $\mathbf{U}_h'$  has only one component in the  $\mathbf{K}_h$  direction which may be found from (4.5). The module of  $\mathbf{U}_h'$  vector is equal to:

$$|\mathbf{U}_h'| = |u_n'| = a |\cos(kx + ly + mz - \sigma t + \varphi_0)|, \quad (4.11)$$

where  $u_n'$  and  $a$  are defined from (4.5) and (4.8) respectively.

Relations (4.5) and (4.6) connect the horizontal wind perturbations with pressure perturbations. One can find under assumption of small variations using results of the report 2 the relationships connecting the density perturbations  $\rho'/\rho_0$  with the horizontal wind perturbations:

$$u_n' = ((k^2 + l^2)^{1/2}/\omega)(1 - \omega^2/N^2)/(1 - f^2/\omega^2)(g/m)/(1 + tg^2 \psi)^{1/2} [\rho'/\rho_0 \exp(i(\pi/2 - \psi))], \quad (4.12)$$

$$v_n' = (f/\omega)((k^2 + l^2)^{1/2}/\omega)(1 - \omega^2/N^2)/(1 - f^2/\omega^2)(g/m)/(1 + tg^2 \psi)^{1/2} [\rho'/\rho_0 \exp(i(-\psi))], \quad (4.13)$$

$$\psi = \text{Arctg}((\Gamma_u/m)(\gamma - 2\omega^2/N^2)/(2 - \gamma)). \quad (4.14)$$

If  $\omega/N \ll 1$ , then according to (4.14), we have  $tg \psi \rightarrow tg \psi_0 = (\Gamma_u/m)\gamma/(2 - \gamma)$  and, as it follows from (4.12), (4.13) one can obtain the following equations

$$u_n' \cong (g/N)/(1 - f^2/\omega^2)^{1/2} [\rho'/\rho_0 \exp(i(\pi/2 - \psi_0))], \quad (4.15)$$

$$v_n' \cong (f/\omega)(g/N)/(1 - f^2/\omega^2)^{1/2} [\rho'/\rho_0 \exp(i(-\psi_0))], \quad (4.16)$$

$$\psi_0 = \text{Arctg}((\Gamma_u/m)\gamma/(2 - \gamma)) = \text{Arctg}(1/(2Hm)). \quad (4.17)$$

As it may be seen from (4.15) and (4.16), the wind perturbations  $u_n'$  and  $v_n'$  grow with the frequency decrease when  $\omega \rightarrow f$  while the amplitude values of the velocity perturbations in the wave propagation direction and in perpendicular direction along the constant phase lines are approximately equal. According to (4.15) and (4.16), the phase difference between the velocity perturbations  $u_n'$  and the density oscillations is equal to  $(\pi/2 - \psi_0)$ , and the phase difference between the density oscillations and the velocity perturbations  $v_n'$  is equal to  $\psi_0$ . If it is assumed that  $(\Gamma/m)\gamma/(2 - \gamma) = (\Gamma_u/m)(7/3) \ll 1$ , then the angle  $\psi_0$  approaches zero, since  $\psi_0 \cong tg \psi_0 = (\Gamma_u/m)\gamma/(2 - \gamma) = 1/(2Hm) \ll 1$ , and the phase difference between the velocity perturbations  $u_n'$  and the density oscillations or velocity perturbations  $v_n'$  is equal to  $\pi/2$ . Then, from the equations (4.15) and (4.16), one obtains

$$u_n' \cong (g/N)/(1-f^2/\omega^2)^{1/2} (i\rho'/\rho_0), \quad (4.18)$$

$$v_n' \cong (f/\omega)(g/N)/(1-f^2/\omega^2)^{1/2} (\rho'/\rho_0). \quad (4.19)$$

Now, we consider the additional limitation  $f/\omega \ll 1$ . In this case, the asymptotic expressions for  $u_n'$  and  $v_n'$  take extremely simple forms:

$$u_n' \cong (g/N) [\rho'/\rho_0 \exp(i(\pi/2 - \psi_0))], \quad (4.20)$$

$$v_n' \cong (f/\omega)(g/N) [\rho'/\rho_0 \exp(i(-\psi_0))]. \quad (4.21)$$

When condition  $f/\omega \ll 1$  is valid, the velocity perturbations  $v_n'$  approach zero:  $v_n' \rightarrow 0$ . If the condition  $\psi_0 \cong (\Gamma_w/m)\gamma/(2-\gamma) = 1/(2Hm) \ll 1$  is also applicable to this case, then the angle  $\psi_0$  can be neglected, and equation (4.20) can be further simplified to:

$$u_n' \cong (g/N) (i\rho'/\rho_0). \quad (4.22)$$

When  $\omega/N \cong 1$  (high frequency case) we have  $\text{tg}\psi \rightarrow \text{tg}\psi_1 = -\Gamma_w/m$ . In this case the next relationships can be obtained

$$u_n' \cong (g/N)(1-\omega^2/N^2)^{1/2} [\rho'/\rho_0 \exp(i(\pi/2-\psi_1))], \quad (4.23)$$

$$v_n' \cong (f/N)(g/N)(1-\omega^2/N^2)^{1/2} [\rho'/\rho_0 \exp(i(-\psi_1))], \quad (4.24)$$

where the angle  $\psi_1$  is equal to:

$$\psi_1 = \text{Arctg}(-\Gamma_w/m) = -\text{Arctg}(\Gamma_w/m) = -\text{Arctg}[(2-\gamma)/(2Hm\gamma)]. \quad (4.25)$$

One may see from (4.23) and (4.24) that in the high frequency case, when  $\omega \rightarrow N$ , both components  $v_n'$  and  $u_n'$  are negligible. This corresponds to the case when the pressure perturbation amplitude  $A_p$  approaches zero.

The RO temperature variations, which are connected with internal GW, may serve as the indicator of wave activity in the atmosphere, also. To establish the relation between the GW parameters and the temperature variations one can use the results published in the report 2. For low- frequency case when  $\omega \rightarrow f$  ( $\omega \ll N$ ) one

can obtain the next relationships connecting the horizontal wind perturbations with temperature variations  $T'$

$$u_n' \cong (g/N)/(1-f^2/\omega^2)^{1/2} [T'/T_0 \exp(i(-\pi/2 + \delta_0))], \quad (4.26)$$

$$v_n' \cong (f/\omega)(g/N)/(1-f^2/\omega^2)^{1/2} [T'/T_0 \exp(i(-\pi + \delta_0))], \quad (4.27)$$

where angle  $\delta_0$  is equal to:

$$\delta_0 = \psi_0 = \text{Arctg}((\Gamma_u/m)\gamma/(2-\gamma)) = \text{Arctg}[1/(2Hm)]. \quad (4.28)$$

The function  $T_0$  is the background temperature depending on the altitude.

For the medium – frequency case  $N \gg \omega \gg f$  one can obtain

$$u_n' \cong (g/N) [T'/T_0 \exp(i(-\pi/2 + \delta_0))], \quad (4.29)$$

$$v_n' \cong (f/\omega)(g/N) [T'/T_0 \exp(i(-\pi + \delta_0))] \rightarrow 0. \quad (4.30)$$

The angle  $\delta_0$  can be neglected provided that the following condition will be valid:

$\delta_0 \cong \text{tg} \delta_0 = (\Gamma_u/m)\gamma/(2-\gamma) = 1/(2Hm) \ll 1$ . In this case, from the equation (4.29), one obtains:

$$u_n' \cong (g/N) (-iT'/T_0). \quad (4.31)$$

Equation (4.31) has been used as polarization relationship for obtaining connections between the temperature variations and the horizontal wind perturbations (*Liou et al.* 2003). The relationship (4.31) has been used earlier by *Pfiester et al.* 1993 for the case analysis of GW activity in the tropical cyclone.

For the high frequency waves:  $\omega \rightarrow N$  ( $\omega/N \cong 1$ ) and one can obtain

$$u_n' \cong (g/N)(1-\omega^2/N^2)^{1/2} [T'/T_0 \exp(i(-\pi/2 + \delta_1))] \rightarrow 0, \quad (4.32)$$

$$v_n' \cong (f/N)(g/N)(1-\omega^2/N^2)^{1/2} [T'/T_0 \exp(i(-\pi + \delta_1))] \rightarrow 0. \quad (4.33)$$

where angle  $\delta_1$  is equal to:

$$\delta_1 = -\psi_1 = \text{Arctg}(\Gamma_u/m) = \text{Arctg}[(2-\gamma)/(2Hm\gamma)]. \quad (4.34)$$

The advantage of this derivation consists in the absence of the assumption on the isothermic atmosphere. The background temperature  $T_0$  in the equations (4.31)-(4.35) can change as function of the altitude. This result is supported also by elaboration made earlier (*Lindzen, 1981*). Another feature of this elaboration is the connection between the relative density variations and the horizontal wind perturbations (4.22). Using (4.22) one can obtain directly the GW polarization relationship between the refractivity variations  $\delta N$  relative to the background refractivity profile  $N_0(h)$ , and the horizontal wind perturbations for medium frequency case:

$$u_n' \cong (g/\omega_b) (i\delta N/N_0), \quad (4.35)$$

where  $\omega_b$  is the Brunt-Vaisala frequency,  $g$  is the gravity acceleration. The polarization relationship (4.35) is important for analysis of RO data in the troposphere, stratosphere and mesosphere.

## 5. AMPLITUDE OF GPS RO SIGNALS AS RADIOHOLOGRAPHIC IMAGE OF GW IN THE ATMOSPHERE

### 5.1. GW IN THE ATMOSPHERE: BACKGROUND

GWs play a decisive role in affecting the atmospheric circulation and temperature regime (*Fritts and Alexander, 2003*). For theoretical studies of the GWs phenomena it is important to have the experimental data showing the phase and amplitude dependence of the GWs on height. Radiosonde and rocketsonde GWs measurements, balloon soundings, radar observations, and lidar studies have been limited to the ground-based sites (*Eckermann et al. 1995*) mainly over specific land parts of the Northern Hemisphere.

Recently a few high-resolution stratospheric satellite instruments have been used to detect GWs (*Eckermann and Preusse, 1999*). However the time for observations has been limited. This raises the problem of insufficient data for

establishing wave climatology for a global scale, despite the good results from many of the ground-based and space-borne instruments (*Steiner and Kirchengast, 2000*).

The radio occultation (RO) experiments appear to be a new tool for studying the variations caused by GW on a global scale. Analysis of the temperature variations found from the RO phase data furnishes an opportunity to measure the statistical characteristics of the GWs in the atmosphere as shown by *Tsuda et al. 2000, Steiner and Kirchengast, 2000, Tsuda and Hocke, 2002. Tsuda et al. 2000*, investigated global morphology of the GW activity in the stratosphere. *Steiner and Kirchengast, 2000*, produced and analyzed the mean vertical wave number spectra of the normalized temperature fluctuations found from the RO phase data in the low, middle and high latitude's bands within the lower stratosphere (~15-30 km), where the data accuracy was proven the highest. *Tsuda and Hocke, 2002*, determined a vertical wave number spectrum of the normalized temperature fluctuations found from the phase data of the GPS/MET RO events during three periods in June/July 1995, October 1995, and February 1997. They estimated seasonal and latitudinal variations of the potential energy of the GW per unit mass.

The amplitude channels of the RO signal give new potential and capability for the observation of and research on the atmospheric waves (*Igarashi et al. 2000*). As shown by *Igarashi et al. 2000, 2001, Pavelyev et al. 2002, Liou et al. 2002*, the amplitude channels of the radio holograms contain important information on the vertical gradients of the temperature and refractivity in the atmosphere and electron density in the mesosphere. Quasi-regular structures are often seen in the amplitude data at the heights corresponding to the tropopause and lower stratosphere. These structures are changing owing to geographical position and having vertical periods in the interval 0.8-4 km. The structures with small vertical periods are possibly

associated with the GW transmitting the energy and momentum through the troposphere to the stratosphere (*Steiner and Kirchengast, 2000, Tsuda and Hocke, 2002*).

The polarization and dispersion relationships for GW (e.g., *Fritts and Alexander, 2003*) can be exploited as shown by *Liou et al. 2003*, to study the regular parameters associated with the GW in the clusters observed in the RO amplitude and phase data. For example, the vertical distribution of the horizontal wind perturbations can be inferred by analyzing the temperature variations. Thus the radio occultation method appears very promising to measure the regular characteristics of the GW and the vertical distribution of the horizontal wind perturbations. The aim of this section is (1) to demonstrate the possibility of measuring the regular characteristics of atmospheric waves (their phase and amplitude as function of height) and (2) to define the horizontal wind perturbations and its vertical gradients associated with GW using the amplitude of the RO signals (thereafter called the amplitude method).

## 5.2 AMPLITUDE METHOD OF GW ANALYSIS

For the refraction attenuation of the RO signal intensity we use the formulas obtained previously by *Pavelyev and Kucherjavenkov, 1978*,

$$X(p) = p R_0^2 [R_1 R_2 (n^2(R_2) R_2^2 - p^2)^{1/2} (n^2(R_1) R_1^2 - p^2)^{1/2} \sin \theta]^{-1} \left| \frac{\partial \theta}{\partial p} \right|^{-1}, \quad (5.1)$$

$$\theta = \pi + \xi(p) - A(p),$$

$$\frac{\partial \theta}{\partial p} = -p^{-1} \frac{\partial \Phi}{\partial p} = d\xi/dp - 1/[n^2(R_2) R_2^2 - p^2]^{1/2} - 1/[n^2(R_1) R_1^2 - p^2]^{1/2} \quad (5.2)$$

where  $R_0$  is the distance GDL (Fig. 3.1). Relationships (5.1), (5.2) connect the phase path excess and refraction attenuation. It follows from (5.1), (5.2) that one can determine, in principle, the refraction attenuation using the phase path excess data because connections (5.2) between the partial derivatives on the impact parameter  $p$  of the phase path excess  $\Phi(p)$ , central angle  $\theta(p)$  and refraction angle  $\xi(p)$ . As a

consequence, equations (5.1), (5.2) indicate that the refraction attenuation and the amplitude data contain all necessary information needed for retrieving the vertical refractivity profiles. The refraction attenuation  $X(p)$  can be written in more simple form (Pavelyev *et al.* 1997):

$$X(p) = p/p_s [(R_2^2 - p_s^2)^{1/2} (R_1^2 - p_s^2)^{1/2}] / [(n^2(R_2)R_2^2 - p^2)^{1/2} (n^2(R_1)R_1^2 - p^2)^{1/2}] \left| \frac{\partial \theta}{\partial p_s} \right| / \left| \frac{\partial \theta}{\partial p} \right| \approx \left| \frac{\partial \theta}{\partial p_s} \right| / \left| \frac{\partial \theta}{\partial p} \right|, \frac{\partial \theta}{\partial p_s} = -1/(R_2^2 - p_s^2)^{1/2} - 1/(R_1^2 - p_s^2)^{1/2} = -B(p_s) \quad (5.3)$$

The refraction attenuation  $X(p)$  (5.3) depends mainly on the derivative of the refraction angle  $d\xi(p)/dp$  because in the decimeter frequency range changes in the impact parameters  $p$ ,  $p_s$  are relatively small in the RO experiments and concentrated in the interval  $\pm 2\%$ . As a consequence, the refraction attenuation  $X(p)$  practically does not depend on the geometrical part of the phase path excess  $L(p)$  and on the local refractivity part  $\delta(p)$ . The refraction attenuation  $X(p)$  depends mainly on the second derivative of the main refractivity part of the phase path excess  $\kappa(p)$ :

$$X(p) = [1/(R_2^2 - p_s^2)^{1/2} + 1/(R_1^2 - p_s^2)^{1/2}] / \left[ \frac{d^2 \kappa / dp^2 + 1/[n^2(R_2)R_2^2 - p^2]^{1/2} + 1/[n^2(R_1)R_1^2 - p^2]^{1/2}}{d^2 \kappa / dp^2 + 1/[n^2(R_2)R_2^2 - p^2]^{1/2} + 1/[n^2(R_1)R_1^2 - p^2]^{1/2}} \right] \quad (5.4)$$

The amplitude of the RO signal mostly depends on the second derivative of the main phase path excess  $\kappa(p)$  (3.6), (3.10). However the amplitude data depend on the technical shortcomings including the receiver noise, multi-path antenna effect, instability in the transmitter's power and receiver's gain. Despite these technical errors the amplitude of the RO signal is valuable source of information on the ionospheric and atmospheric parameters (Pavelyev *et al.* 2002 (a), 2002 (b), Liou *et al.* 2002).

The amplitude variations may be used to obtain the temporal dependence of the refraction attenuation  $X(t)$  and then the height distribution of the vertical gradient of the refractivity. The next connections exist between  $p$ ,  $X(t)$  and  $p_s$ :

$$p dp/dt = X(t) p_s dp_s/dt \quad (5.5)$$

Approximate solution of equation (5.5) may be presented for the case of circular orbits in an integral form (Kalashnikov et al. 1986):

$$p - p_0 = \int_{p_{s0}}^{p_s} X[t(p_s)] dp_s \quad (5.6)$$

Equation (5.6) gives a temporal dependence of the impact parameter  $p(t)$  if initial values  $p_0 = p(t_0)$ ,  $p_{s0} = p_s(t_0)$  at the time instant  $t_0$  are known. Supposing  $p \approx p_s$  one may obtain:

$$X(t) \approx [\partial\theta(p_s)/\partial p_s] / \partial\theta(p)/\partial p; \quad d\xi/dp = [1 - 1/X(t)] B(p_s) \quad (5.7)$$

The second equation of (5.7) gives the temporal dependence of  $d\xi/dp$ . Thus the amplitude data may be used for the restoration of the impact parameter  $p(t)$ , refraction angle  $\xi(t)$  (from known value  $p$  using the first equation (5.2)) and derivative  $d\xi/dp(t)$ . These temporal dependencies may be used to find the vertical distribution of the vertical gradient of the refractivity  $dN(h)/dh$  (Liou et al. 2002):

$$dN(h)/dh = -n^2(h) J(p) / \{p[1 + J(p)]\}; \quad J(p) = 1/\pi \int_0^{\infty} \xi(x) / dx^2 (x^2 - p^2)^{1/2} dx; \\ p = n(h)(a+h), \quad n(h) = 1 + N(h) * 10^{-6}, \quad d\xi(p)/dp = B(p)(X-1)/X, \quad X = A^2/A_0^2. \quad (5.8)$$

Equations (5.8) can be applied for solution of the direct and inverse problems: to find the amplitude variations for given refractivity profile (direct problem) and to find the refractivity distribution from given amplitude variations. Pavelyev and Yeliseev, 1989, Pavelyev et al. 1996, 1997, Pavelyev, 1998, described the details of solution of the direct problem and ray tracing technology for both single ray and multi-beam propagation. The inverse problem may be solved under an assumption of one ray propagation, which may be examined by the radio holographic method for any given radio occultation event.

The amplitude information may be used to retrieve the vertical gradient of the temperature profile. As shown by *Liou et al.* 2002, for the case of a wet atmosphere a connection exists between the vertical gradients of the temperature and refractivity:

$$[dT^*(h)/dh]/T^*(h) = -[N(h)]^{-1} dN(h)/dh - T_x/T_a(h), \quad (5.9)$$

$$T^*(h) = T(h) / \{1 + 4810e(h)/[P(h)T(h)]\}, \quad T_x \approx 34.16 \text{ K/km},$$

$$T_a(h) = T(h)[1 + 0.378e(h)/P(h)], \quad (5.10)$$

where  $T(h)$  is the temperature of the atmosphere [K],  $T^*(h)$  is the “wet” temperature of the atmosphere depending on the water vapor pressure  $e(h)$  and atmospheric pressure  $P(h)$  [hPa], respectively. Equations (5.9) and (5.10) connect the vertical gradient of the logarithm of the refractivity with the vertical gradient of logarithm of the “wet” temperature  $T^*(h)$ . At the height above 10 km equations (5.9), and (5.10) may be used to find the vertical gradient of the temperature profile if the refractivity gradient is known. Integration of equation (5.9) may give the vertical profile  $T(h)$  if an initial condition is known at some height  $h_\infty$ :

$$T^*(h) = T^*(h_\infty) N(h_\infty) N^{-1}(h) + T_x N^{-1}(h) \int_{h_\infty}^h N(h) dh / \{ (1 + 0.378e/p) [1 + 4810e/(pT)] \} \quad (5.11)$$

Equation (5.11) gives the vertical temperature profile  $T(h)$  for the general case of the wet atmosphere. For the case of dry atmosphere  $e(h)=0$  and two more simple equations may be obtained for two boundary conditions:

$$T(h) = T_x N^{-1}(h) \int_h^\infty N(h) dh; \quad (5.12)$$

Equation (5.12) has been published by *Hocke*, 1997.

In Fig. 5.1-5.3 the amplitude variations A1, and A2 at two frequencies F1, and F2 are compared with the retrieved perturbations in the vertical gradient of the refractivity  $dN(h)/dh$  [K/km] (curves G1, and G2) for GPS/MET RO events: 0537; 0564; 0648 (June 19, 1995). Fig. 5.1-5.3 describe the variations of the magnitude

$dN(h)/dh$  for two low latitude regions with co-ordinates 16.3 N, 104.6 W; 13.7 N, 131.9 W, and one moderate latitude area with co-ordinates 48.1 S, 333.7 W. The amplitude data A1, and A2 are normalized relative to the free space conditions and displaced for comparison. Curves G1, and G2, that describe the variations of  $dN(h)/dh$  measured at frequencies F1, and F2, are also displaced in Fig. 5.1-5.3 for comparison. Fig. 5.1-5.3 consist of two parts to describe the variations of  $dN(h)/dh$  in the height intervals 2-20 and 20-40 km, respectively, with the aim to show in the appropriate scale the variations of the refractivity gradient at the high altitudes. The retrieved vertical refractivity gradients G1, and G2 revealed quasi-regular variations at the tropopause altitudes both in the low latitude and moderate latitude areas. Typical values of

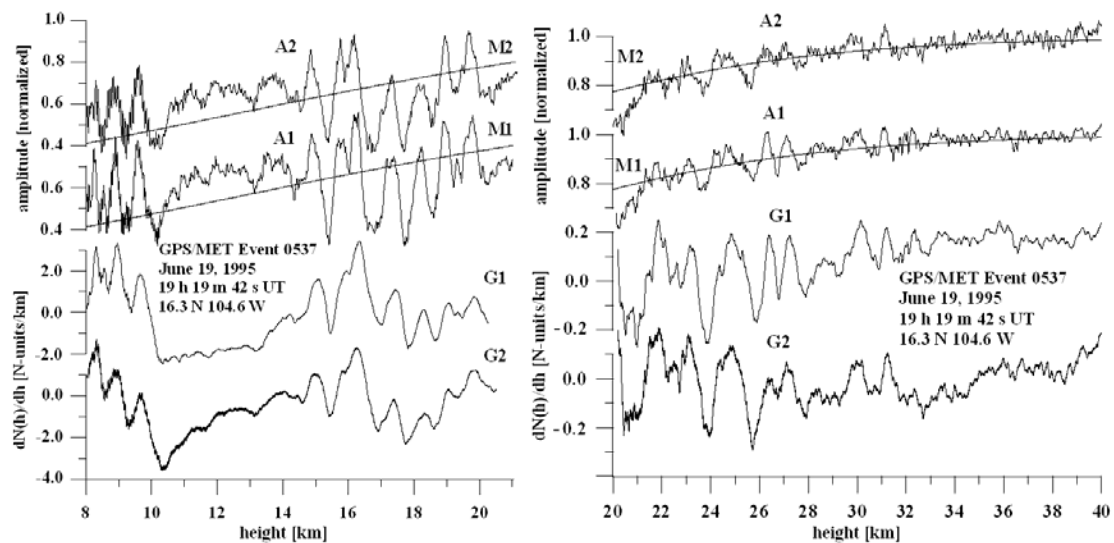


Fig. 5.1. The vertical gradients of the refractivity G1, and G2 (perturbed part) in the low latitude troposphere retrieved from the amplitude channels A1, and A2 of the radio hologram at the frequencies F1, and F2 (GPS/MET radio occultation data, event 0537). The curves M1, M2 indicate the refraction attenuation corresponding to the refractivity model in the RO region.

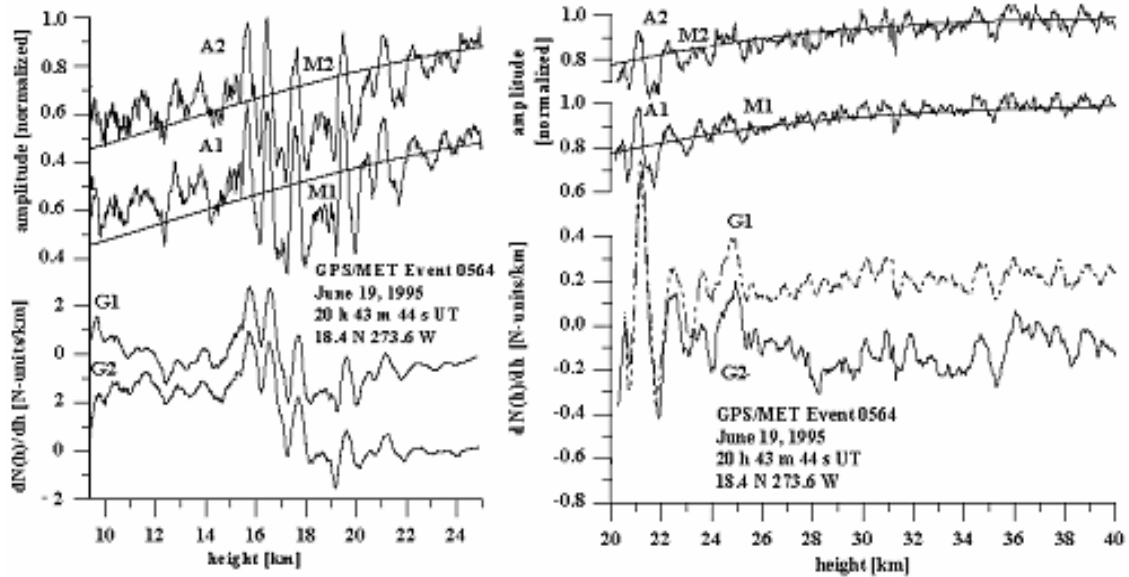


Fig. 5.2. The vertical gradients of the refractivity G1 and G2 (perturbed part) in the low latitude troposphere and stratosphere above India (GPS/MET radio occultation data, event 0564). The designations are the same as in Fig. 5.1.

these variations are about  $\pm 4$ -6 N-units/km and typical vertical periods are 0.8-2.5 km.

Changes in the vertical gradients of the refractivity may be connected with the GW propagating through the tropopause areas and, consequently, may correspond to the sharp changes in the horizontal wind velocity. The changes of  $dN(h)/dh$  below

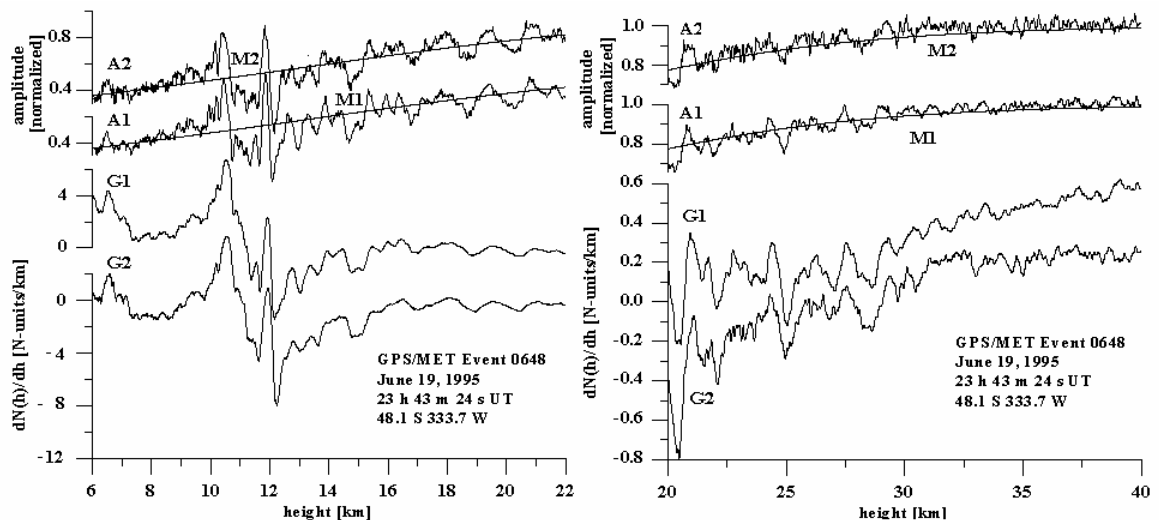


Fig. 5.3. The vertical gradients of the refractivity G1 and G2 (perturbed part) in the middle latitude troposphere and stratosphere above Europe (GPS/MET radio occultation data, event 0648). The designations are the same as in Fig. 5.1.

tropopause altitudes may be connected with water vapor influence and clouds structures. In the stratosphere region the wave-like structures can be seen in Fig. 5.1-5.3 (right parts) also. Typical values of these variations are about  $\pm 0.2$ - $0.6$  N-units/km and typical vertical periods are 1-3 km. As follows from the radiosondes observations

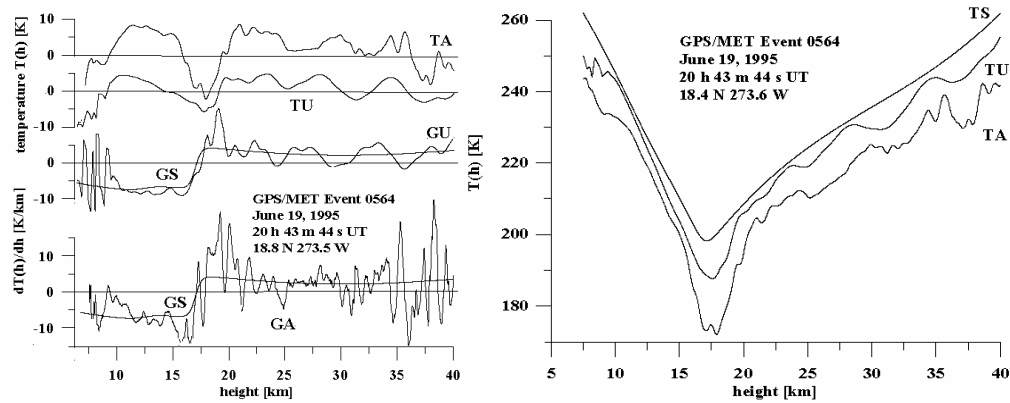


Fig. 5.4. Temperature vertical profile (right panel), its perturbations and vertical gradient (left panel) retrieved from the amplitude (curves TA, GA) and phase RO data (curves TU, GU) at two frequencies F1, and F2 (GPS/MET RO event 0564). Curve TS (right panel) corresponds to smooth approximation of the temperature TU. Curves TA, TS (right panel) are displaced by  $\pm 5$  K for comparison with the UCAR temperature profile TU. Curve GS (left panel) corresponds to smooth approximation of the vertical temperature gradient GU.

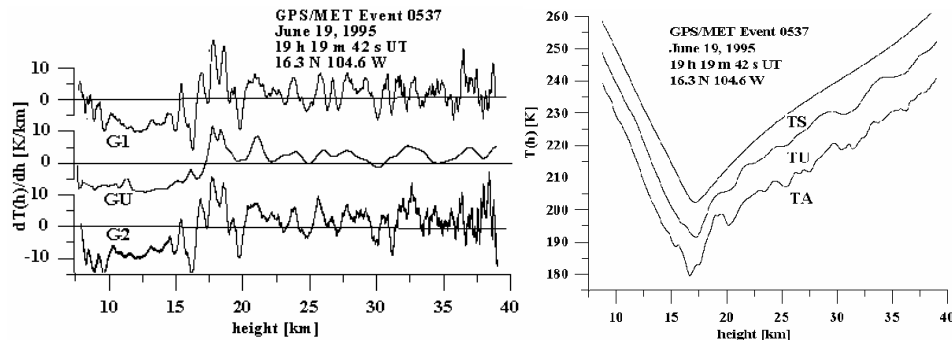


Fig. 5.5. Temperature vertical profile (right panel) and its gradient (left panel) retrieved from the amplitude (curves TA, GA) and phase RO data (curves TU, GU) at two frequencies F1, and F2 (GPS/MET RO event 0564). Curves G1, G2 (left panel) correspond to the temperature vertical gradient retrieved from the amplitude A1, A2 of the RO signal. Curve TS (right panel) corresponds to smooth approximation of the temperature TU. Curves TA, TS (right panel) are displaced by  $\pm 5$  K for comparison with the UCAR temperature profile TU.

(Tsuda *et al.* 2000) these variations may correspond to the GW propagation through the stratosphere. Statistical analysis of these variations may give important

information on the dynamics of the atmosphere circulation in the stratosphere as shown by *Tsuda et al. 2000, and Steiner and Kirchengast, 2000.*

The vertical gradients of the refractivity can be applied to retrieve the vertical distribution of the temperature  $T(h)$  and its gradient  $dT(h)/dh$ . The restored vertical profiles of  $T(h)$  and  $dT(h)/dh$  are shown in Fig. 5.4-5.6 for the considered GPS/MET RO events. The curves TU in Fig. 5.4-5.6 present the results obtained by the UCAR (University Consortium for Atmospheric Research) science team (*Ware et al. 1996 and Rocken et al. 1997*) and published at the Internet site: <http://www.cosmic.ucar.edu/gpsmet/feedback.html>. The curves TU describe the retrieved vertical temperature profiles obtained by analysis of the phase RO data. The profiles of the average temperature  $T_a = (T_1+T_2)/2$  retrieved from the amplitude data are shown in Fig. 5.4-5.6 by curves TA. In general the trends of the retrieved temperatures TA are consistent with those provided by UCAR. Curves TA give the same tropopause height at 16 - 18 km for the low latitude areas similar to UCAR data and at 10 – 12 km for the high and moderate latitudes (Fig. 5.4-5.6). As follows from Fig. 5.4-5.6 the temperature vertical profiles found from the amplitude data are close to corresponding UCAR data with accuracy  $\pm(2-4)$  K. Curves GU in Fig. 5.4-5.6 are obtained from the UCAR temperature profile TU by numerical differentiating. The temperature gradient retrieved from the amplitude data reveals better spatial variations with vertical periods 0.4-5 km than the UCAR temperature gradient or higher frequency variation. Sharp variations in the vertical gradients corresponding to the tropopause region from  $-10\dots-12$  K/km up to  $10\dots14$  K/km are visible in Fig. 5.4-5.6. These changes are better seen in the gradients restored from the amplitude data. The corresponding temperature variations have amplitudes  $\pm(5\dots8)$  K in the tropopause and  $\pm(2\dots4)$  K in the stratosphere. The variations of the vertical gradient

in the stratosphere revealed wave-like structures with vertical periods of about 0.8...2 km and amplitude of about  $\pm(4...6)$  K/km. Observation of the vertical gradients of the refractivity in the tropopause by means of analysis of the amplitude variations in the RO signal shows the usefulness of the suggested method to study the natural processes in the atmosphere.

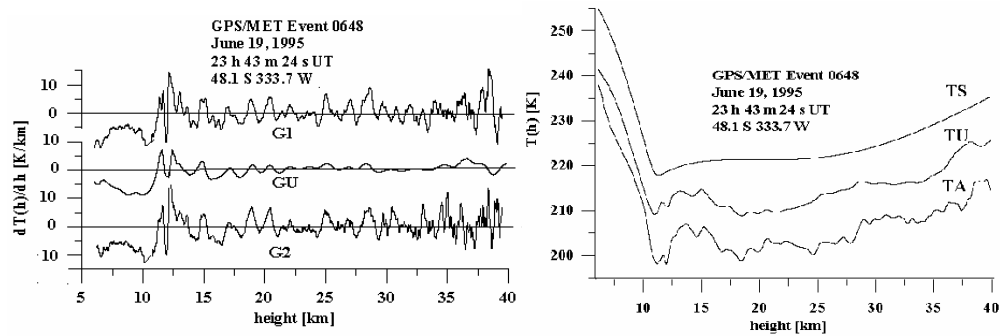


Fig. 5.6. Temperature vertical profile (right panel) and its gradient (left panel) retrieved from the amplitude (curves TA, GA) and phase RO data (curves TU, GU) at two frequencies F1 and F2 (GPS/MET RO event 0648). Curves G1, G2 (left panel) correspond to the temperature vertical gradient retrieved from the amplitude A1, A2 of the RO signal. Curve TS (right panel) corresponds to smooth approximation of the temperature TU. Curves TA, TS (right panel) are displaced by  $\pm 5$  K for comparison with the UCAR temperature profile TU. A difference between the moderate latitude stratosphere (right panel) and low latitude stratosphere (Fig. 5.4, right panel) is clearly seen.

Below we will consider only perturbations in the vertical gradient of temperature with aim to establish connection with wave structures in the atmosphere. The amplitudes of the RO signal are shown in Fig. 5.7 for the CHAMP RO event 0005 (curve A) and GPS/MET RO event 0316 (curves A1, A2). Results of the simulations of the amplitude dependence on height are shown in Fig. 5.7 by the curves M0 and M. For calculating M0 we used the refractivity model  $N(h)=N_o \exp(-h/H)$  with  $N_o=340$  ( $N$ -units) and  $H=6.4$  km, and the analytical connection between the refraction angle  $\xi(p)$ , the refraction attenuation, and the refractivity gradient described above. We applied the same method to obtain the curves M in Fig. 5.7, but the refractivity model was a sum of damped complex

exponentials  $N(h)=\text{Re}[N_j \exp(-\alpha_j h)]$  with real and complex  $N_j$  and  $\alpha_j$ . The parameters  $N_j$  and  $\alpha_j$  have been determined such as to give the amplitude variations, which are better coinciding with the experimental data.

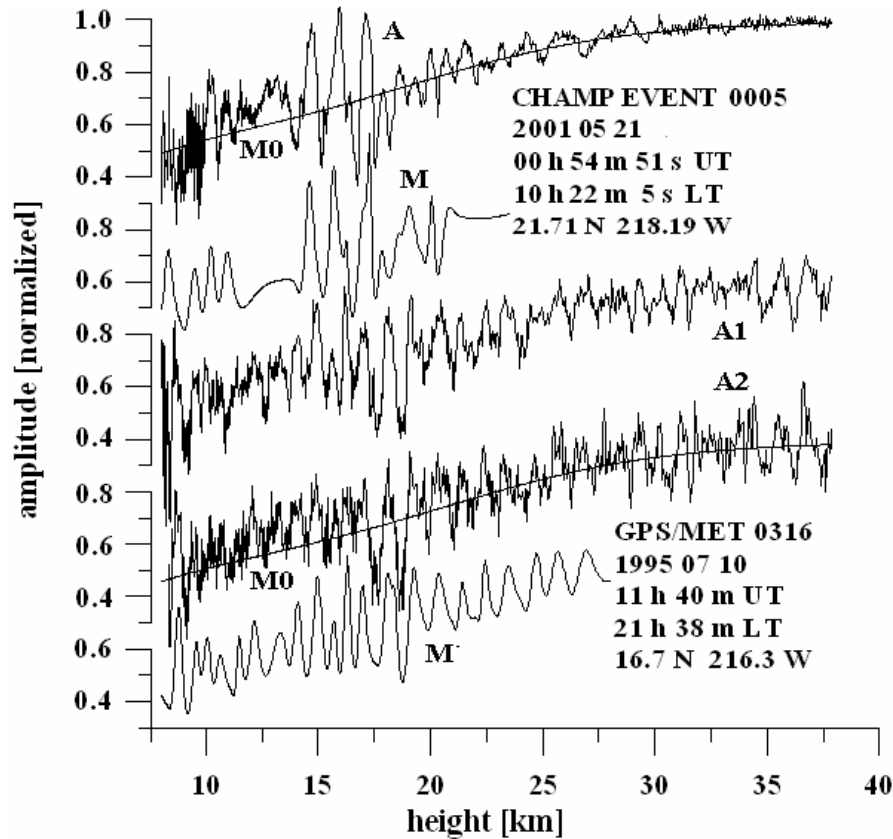


Fig. 5.7. Wave trains in the GPS/MET and CHAMP RO amplitude data. Legend indicates the time of the RO experiments and the geographical co-ordinates of the RO regions.

To obtain the vertical profiles of temperature and its gradient we use the expressions given by *Hocke, 1997*, and *Pavelyev et al. 2002(b)*. The wave train with intense amplitude variations can be noted in the height interval 8-40 km. The wave's vertical wavelength is changing in the range 0.8-2 km. The results of the simulation (the curves M0, M in Fig. 5.7) show a good fit to the experimental data. The result of simulation is in sufficient agreement with the experimental amplitude variations to indicate low level of possible diffraction effect in the considered events. However the diffraction effect can be observed in some cases and upgrading of our model will be

required. The amplitude changes correspond to variations in the refractivity and temperature vertical gradients. The latter can be restored by the amplitude method described by *Kalashnikov et al.* 1986, *Pavelyev et al.* 2002 (a), (b), and *Liou et al.* 2002.

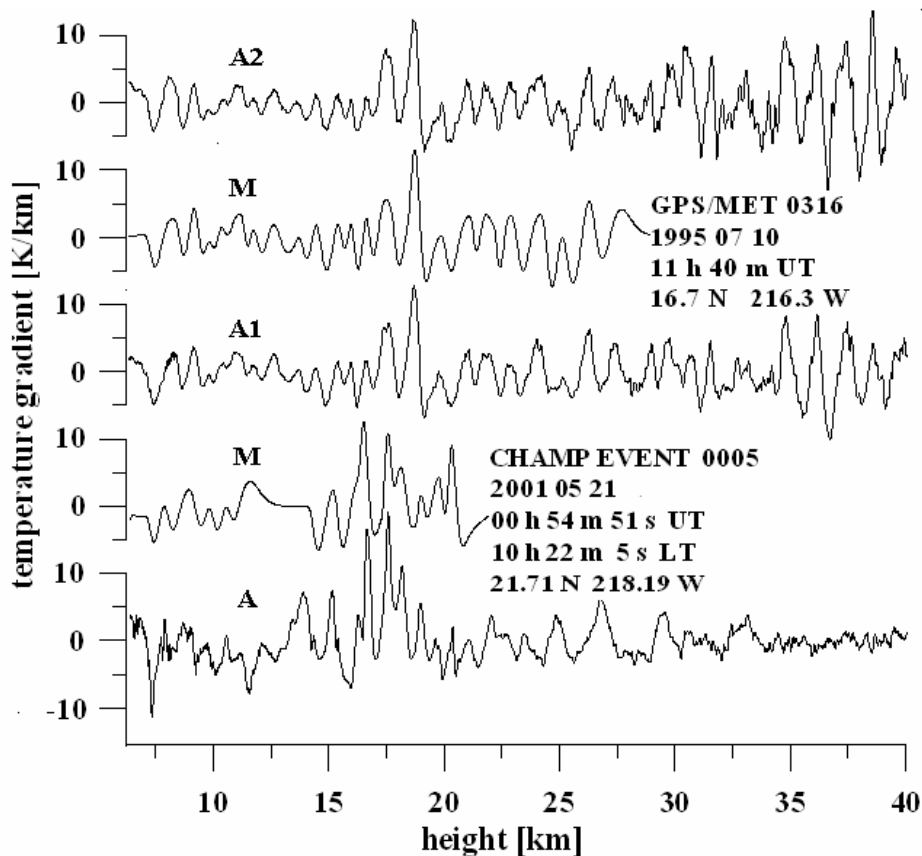


Fig. 5.8. Temperature gradient variations for the GPS/MET and CHAMP RO events.

The vertical gradients of the temperature retrieved from the amplitude data are indicated for CHAMP (the bottom curves A and M) and GPS/MET RO (the upper curves A1, A2 and M) events 0005 and 0316 in Fig. 5.8. Note that in opposition to the case of the GPS/MET RO experiments, in the CHAMP RO experiments only the amplitude variations at the first GPS frequency F1 has been measured. The curves M in Fig. 5.8 indicate the simulation results relating to the CHAMP (the second curve from bottom in Fig. 5.8) and GPS/MET (the second upper curve in Fig. 5.8) RO events, the curves A1, A2, and A describe the vertical temperature gradient variations

restored from the initial amplitude changes shown in Fig. 5.7. It is evident from Fig. 5.8 that the wave activity in the atmosphere is a complex function of height. Maximum of the wave activity is observed in the tropopause region in the height interval 12-17 km. Secondary maxima of the wave activity can be seen in the stratosphere in the height interval 22-27 km. Quasi-regular wave structure with vertical wavelength  $\lambda_v \sim 0.8\text{--}2$  km is previously seen in both experimental and model data. The observed waves in the altitude distribution of the amplitude and vertical temperature gradient can correspond to the GWs activity. If the observed wave structures are caused by the GWs activity then the vertical temperature gradients can be related with horizontal wind perturbations associated using the GWs polarization and dispersion equations.

We will use the polarization relationships, which are valid for the medium-frequency case, when the intrinsic frequency of the GWs is greater than the inertial frequency  $f$ , but is well below the buoyancy frequency  $\omega_b$ . The GWs dispersion relation has the form (Fritts and Alexander, 2003; Eckermann *et al.* 1995)

$$\lambda_v = 2\pi \frac{c - U \cos \varphi}{\omega_b}, \quad (5.13)$$

where  $\lambda_v$  is the vertical wavelength of the GWs,  $U$  is the background wind speed,  $c$  is the ground-based GWs horizontal phase speed, and  $\varphi$  is the azimuth angle between the background wind and the GW propagation vectors. Equation (5.13) connects the vertical wavelength  $\lambda_v$  with the intrinsic phase speed of GW  $v_i = \frac{c - U \cos \varphi}{\omega_b}$ , which can be measured by an observer moving with the background wind velocity (Eckermann *et al.* 1995). A GWs polarization relation has been published previously by Lindzen, 1981. It connects the complex amplitude of the temperature variation,  $t(h)$ , with the horizontal wind perturbations  $v(h)$ , corresponding to the GW influence

$$v = \text{Re}[ig / (T_b \omega_b) t(h)], \quad (5.14)$$

where  $\omega_b^2 = g/T_b \Gamma$ ,  $\Gamma = \partial T_b / \partial h + 9.8^\circ/\text{km}$ ,  $g$  is the gravity acceleration, and  $T_b$  is the background temperature. *Pfister et al.* 1993, applied this relation successfully to the case study of the regular GWs associated with tropical cyclone. *Eckermann et al.* 1995, used it for statistical analysis of the rocketsonde data. One can obtain from (5.14) a connection between the vertical gradients  $dv(h)/dh$  and  $dt(h)/dh$

$$dv(h)/dh = d\text{Re}[ig/(T_b \omega_b)t(h)]/dh \approx \text{Re}[ig/(T_b \omega_b)dt(h)/dh] \quad (5.15)$$

Equation (5.15) is valid assuming that  $T_b(h)$  and  $\omega_b(h)$  are slowly changing at the vertical scales  $\sim \lambda_h$ . The functions  $T_b$  and  $\omega_b$  are known from the model of the atmosphere used for calculating of the refraction attenuation and refractivity in the RO region.

To find the function  $dv(h)/dh$  from the second equation (5.15) one can implement the radio holographic analysis by applying the Hilbert transform (*Rabiner and Gold*, 1978). We suggest that the amplitude variations are a real part of some analytical function. Under this assumption the temperature vertical gradient and the horizontal wind perturbations are also the real parts of the analytical functions, which are connected with the amplitude variations by inversion formulas and polarization relationship (*Liou et al.* 2002). The Hilbert transform is a mathematical tool to find the imaginary part of an analytical function using its real part. Practical implementation of the Hilbert transform gives the analytic presentation of the real signal  $dt(h)/dh$ :

$$dt(h)/dh = \text{Re}\{a_i(h)\exp[i\Phi_i(h)]\}, \quad (5.16)$$

where  $a_i(h)$  and  $\Phi_i(h)$  (real functions) are the amplitude and phase of the vertical gradient of the temperature. Then the function  $dv(h)/dh$  can be restored from (5.15) using the Hilbert transform applied to the experimental and model data, respectively.

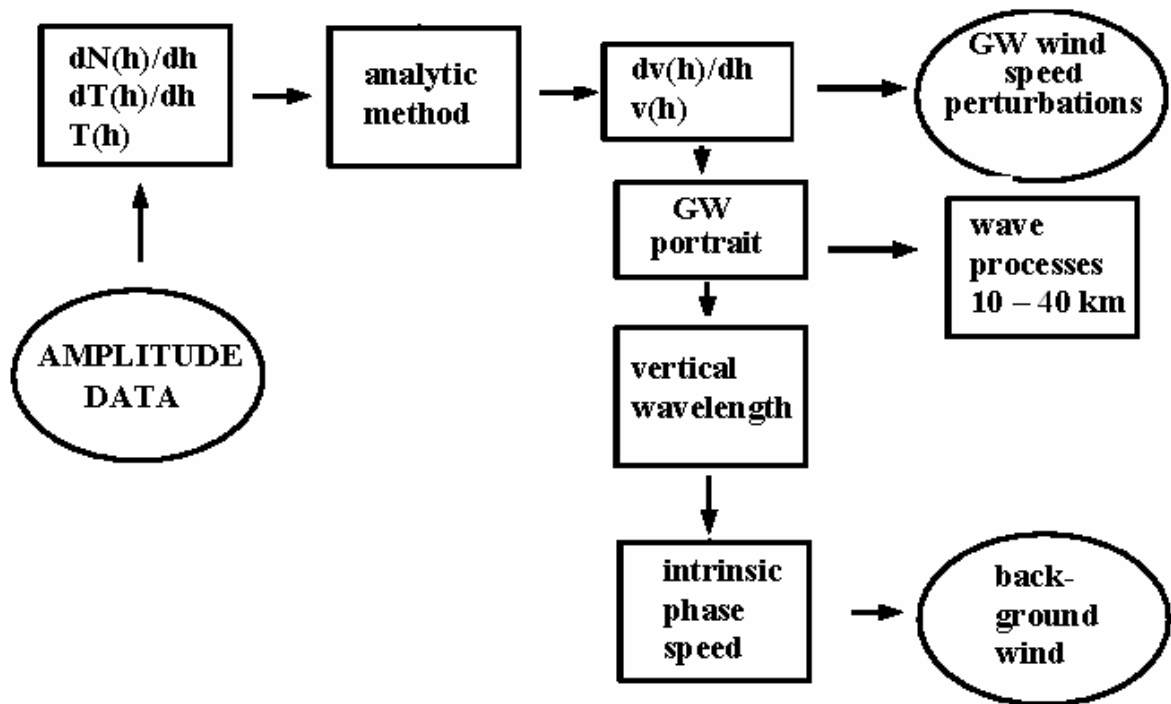


Fig. 5.9. Scheme for determination of the GW parameters using the amplitude of RO signal.

As follows from equations (5.13)-(5.16) the process of obtaining GW parameters consist of 3 stages: (1) evaluation of the vertical profiles of the refractivity, temperature and their gradients using the amplitude variations, (2) using Hilbert transform for estimation of the vertical gradients of the horizontal wind perturbations, (11) estimation of the vertical profiles of the phase and amplitude of GW (obtaining “portrait” or 1-D image of GW). Note, that the RO method gives instantaneously “portrait” of GW because the time of RO event  $\sim 30$  s is small in comparison with the temporal periods of GW. For determination of the direction of the GW propagation it is necessary to have the temporal sequence of the GW “portraits”. Thus from one RO event it is possible to determine only the amplitude of the GW (horizontal wind perturbations). For determination of the sign (or direction of propagation) of these perturbations it is necessary introduce some additional information concerning the

meteorological conditions in the RO region. Below an example of application of this procedure will be shown.

The results of restoration of the vertical gradients of the horizontal wind perturbations are indicated in Fig. 5.10. The upper three curves (A1, A2, M) in Fig. 5.10 are corresponding to the vertical gradient of the horizontal wind perturbations restored for the GPS/MET RO event 0316, while the bottom two curves (M, A) are relating with the CHAMP RO event 0005. The quasi-regular modulation of  $dv/dh$  by the wave structures in the atmosphere is clearly seen both in the experimental and model data. It is important that the vertical period of this modulation is practically the same as seen in the amplitude variations in Fig. 5.7.

After applying the Hilbert transform one can obtain from (5.15) and (5.16) the amplitude  $a(h)$  and phase  $\Phi(h)$  associated with the vertical gradient of the horizontal wind perturbations  $dv(h)/dh = a(h)\cos\Phi(h)$ , where  $a(h)$  and  $\Phi(h)$  are the amplitude and phase of the analytic signal relevant to  $dv(h)/dh$ . The functions  $a(h)$  and  $\Phi(h)$  together present a GWs “portrait”. The height dependence of the GWs phases  $\Phi(h)$  and amplitudes  $a(h)$  are shown in Fig. 5.11 by curves 1, 2 and 3, 4, respectively, for the GPS/MET and CHAMP RO events 0316 and 0005. The phase curves 1, 2 of the GWs

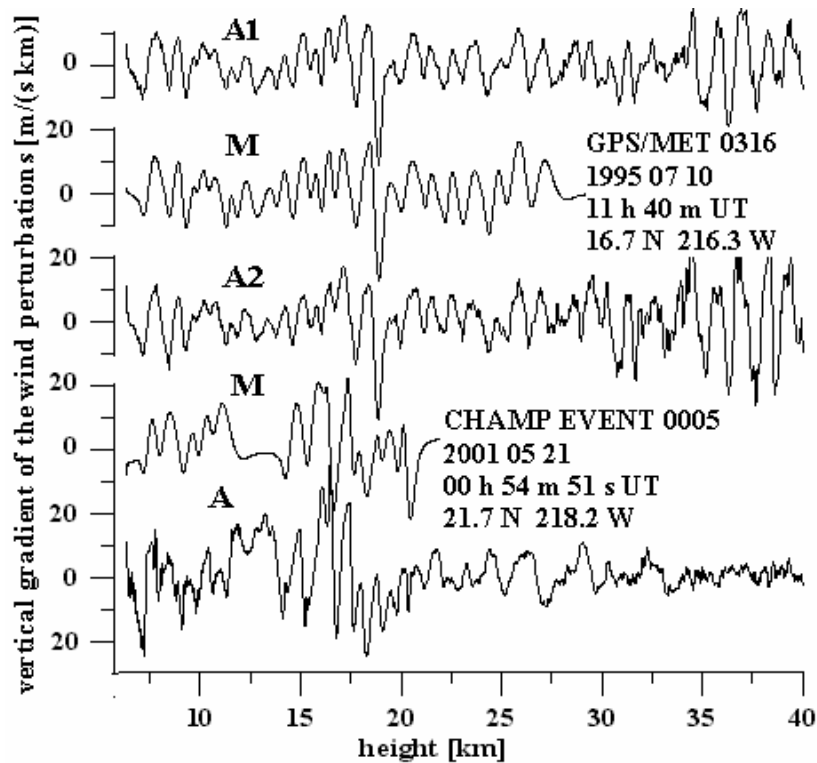


Fig. 5.10. Vertical gradient of the horizontal wind perturbations retrieved on the variations of the vertical temperature gradient for GPS/MET (three upper curves) and CHAMP (two bottom curves) RO events.

“portraits” have different dependence on the height for the GPS/MET and CHAMP RO events. The phase curve 2 is relevant to the CHAMP event.

Another example of the GW activity in the atmosphere is given in Fig. 5.11 for the GPS/ MET RO event 0585. The upper and bottom curves 1, 2 (left panel in Fig. 5.11) demonstrate the height dependence of the phase and amplitude of the GW. The vertical profile  $dv(h)/dh$  (curve 2 in Fig. 5.11) indicates the region where the amplitude of the GW is high: at the heights 14-20 km, 23-25 km, 28-29 km, 31-32 km and low: at the heights 20-22 km, 25-26 km, 33-35 km. The position of the zone where the GW amplitude is low in the height interval 35-37 km is coinciding with the previously satellite observations of the mountain waves activity in the Andes area provided by *Eckermann and Preusse, 1999*.

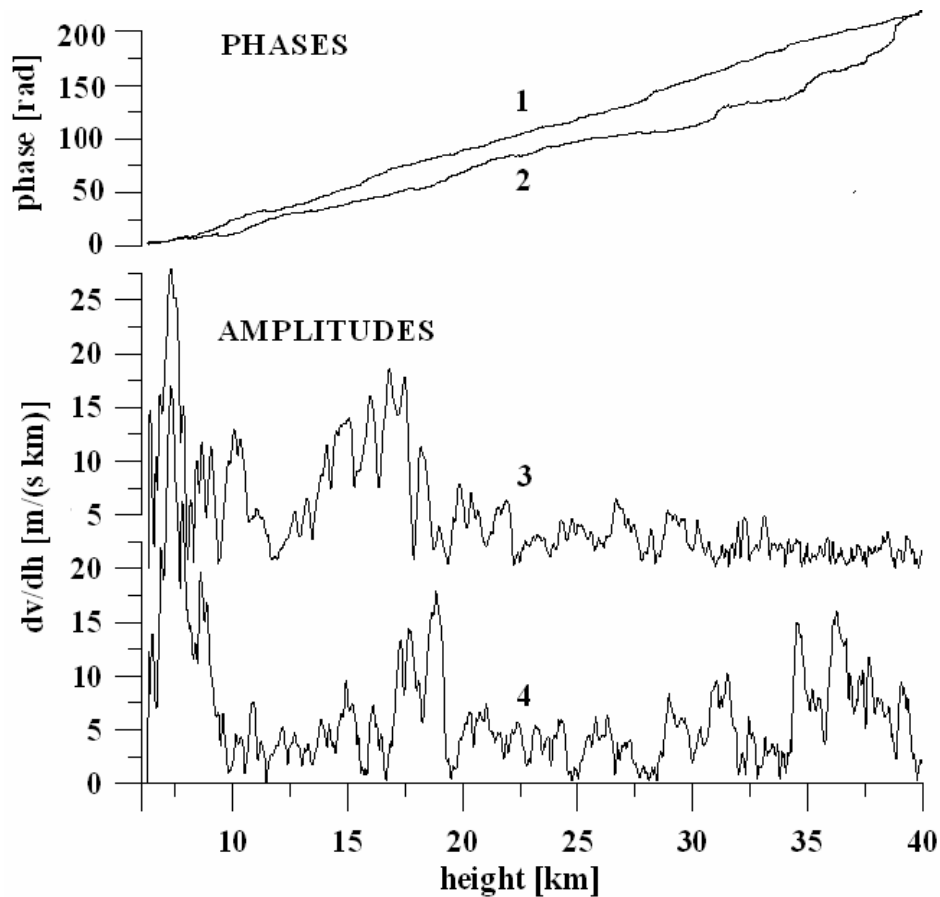


Fig. 5.11. Comparison of the GWs “portraits” found from the wave trains in the amplitude indicates increasing of the spatial frequency of the GW with height. The phase in the GPS/MET event (curve 1) changes monotonically, in average, as a function of the height  $h$ , thus corresponding to monotonically monochromatic GW. The amplitude, relevant to the GPS/MET event (curve 3), demonstrates essential changes in the interval  $0.5 \dots 16 \text{ m/(s km)}$  above 10 km. For this event one can see altitudes with high (17-19 km, 29-31 km, 35-38 km) and low (32-34 km) GW activities. For the CHAMP RO event (curve 4) the amplitude changes are concentrated mainly below 20 km. It follows that the GWs radio images contain important information on the height distribution of the GWs activity in the RO regions.

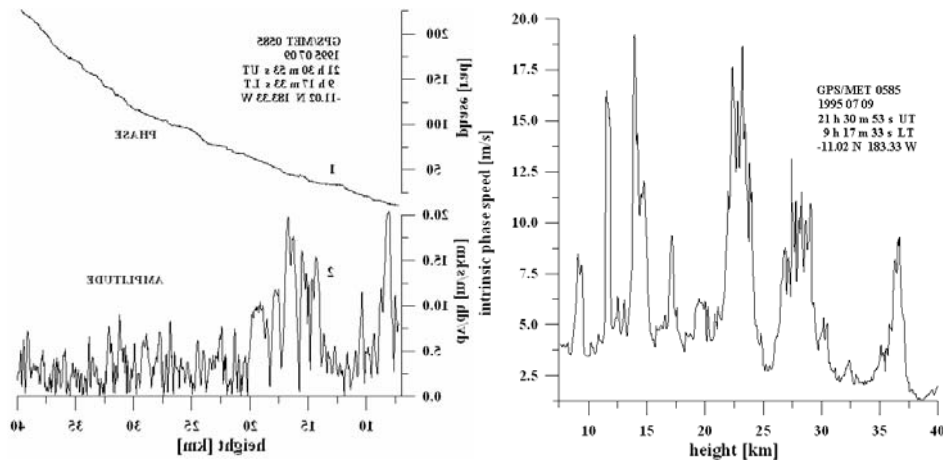


Fig. 5.12. GWs “portrait” for the GPS/MET RO event 0585 with intense variations in the height interval 30-35 km (curves 1, 2). Intrinsic phase speed of the GWs as a function of height for the GPS/MET RO event 0585 (curve 3).

The phase curve 1 in the left panel in Fig. 5.12 reveals in the interval 10-30 km the quasi-linear dependence on the height thus indicating quasi-monochromatic character of the observed wave structure. The detailed information on the height distribution of the spatial frequency of the GW can be obtained by differentiating the phase  $\Phi(h)$  (curve 1 in the left panel in Fig. 5.12). After differentiating one can obtain the spatial frequency  $f$  and the vertical wavelength  $\lambda_h = 1/f$  as functions of height and then estimate the intrinsic phase speed of the GW  $v_i$  (right panel in Fig. 5.12) using the relation (5.13). As seen in Fig. 5.12 (right panel) the value  $v_i(h)$  changes in the range 2-18 m/s. These values of the intrinsic phase speed are similar to the intrinsic phase speed observed by rocketsondes (Eckermann *et al.* 1995) and satellite (Eckermann and Preusse, 1999).

Integration of the vertical gradient  $dv(h)/dh$  can reveal the horizontal wind perturbations  $v(h)$  as a function of height. The function  $v(h)$  is depicted in Fig. 5.13

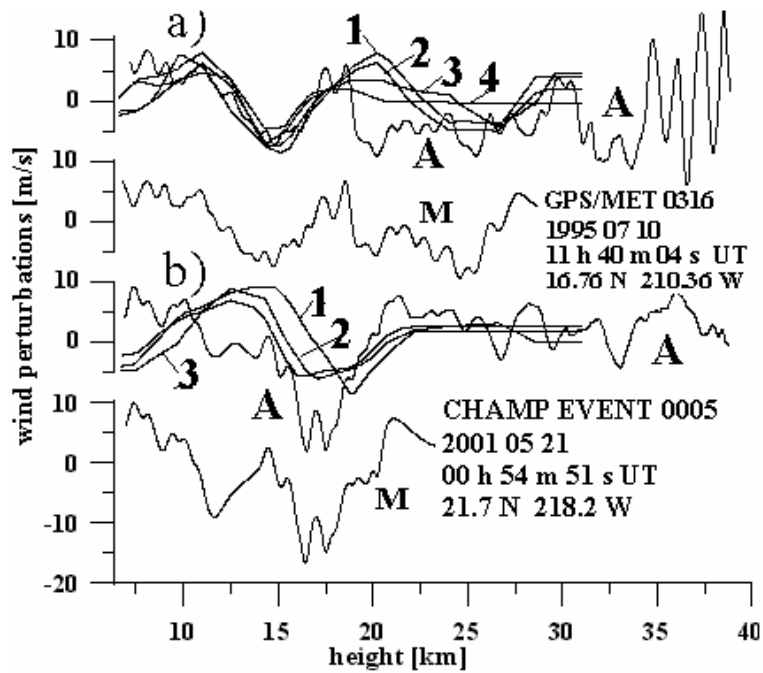


Fig. 5.13. Comparison of the wind perturbations found from GPS/MET and CHAMP RO events with Earth-based radiosondes data.

for two RO events: GPS/MET 0316 (Fig. 5.13, part a)) and CHAMP 0005 (Fig. 5.13, part b)). The curve A in Fig. 5.13, part a) has been obtained by integrating the average wind speed gradient  $dv/dh = [dv_1(h)/dh + dv_2(h)/dh]/2$  (curves A1, A2 in Fig. 5.10) restored from the GPS/MET RO amplitude data. The curve A in Fig. 5.13, part b) has been obtained by integrating the wind speed gradient  $dv/dh$  corresponding to the bottom curve A in Fig. 5.10 restored from the CHAMP RO amplitude data. The curves M (Fig. 5.13, parts a), b)) describes the results of the simulation. The curves 1-4 in Fig. 5.13, part a) indicate the radio sondes (RS) data corresponding to two stations in Taiwan: Hualian (1, 4) ( $24.0^\circ$  N,  $238.4^\circ$  W) and Taipei (2, 3) ( $25.0^\circ$  N,  $238.5^\circ$  W), obtained on July 15, 1995 at 00 h UT (1, 2) and 12 h UT (3, 4), respectively. The curves 1-3 in Fig. 5.13, part b) data correspond to the same stations and indicate the RS data, obtained on May 30, 2001 at 00 and 12 h UT (1, 2) (Taipei) and 12 h UT (3,4) (Hualian), respectively. The difference between the Taiwan Earth-based stations and the GPS/MET RO region latitudes for the event 0316 is about  $8^\circ$ ,

the corresponding value for longitudes is about  $28^\circ$ . The difference between the Taiwan and the CHAMP RO region latitudes for the event 0005 is of about  $3^\circ$ , the corresponding value for longitudes is about  $20^\circ$ . The time difference between the RO events and RS observations has been chosen in accordance with the average background westward wind velocity about 6-10 m/s in the height interval 8-30 km. The RS wind perturbations (curves 1-4 in Fig. 5.13, part a), curves 1-3 in Fig. 5.13, part b)) have been obtained by subtracting the polynomial approximation of the fifth power from the experimental vertical profiles of the horizontal wind speed. As follows from Fig. 5.13, part a) the RS data (1-4) are in fairly good agreement with the results found from the amplitude of the RO signal and simulation (curves A, M in Fig. 5.13, part a), respectively). Some discrepancy of about  $\pm 1-3$  m/s exists in the height interval 19-30 km. The distinction of the CHAMP data (curve A in Fig. 5.13, part b) from the RS data (curves 1-3 in Fig. 5.13, part b)) is greater  $\sim \pm 3-5$  m/s. Note that the RS data do not reveal high-spatial frequencies observed in the RO results. It appears this is due to smoothing effects of the RS measurements. The RO values of  $v(h)$  (curves A in Fig. 5.13) are variable from  $\pm 1$  to  $\pm 12$  m/s at the height interval 10-35 km and indicate some higher magnitudes for the  $v(h)$  as compared with the model's results (curves M in Fig. 5.13). The difference illustrates a current state of the inversion accuracy.

### 5.3. HORIZONTAL WIND PERTURBATIONS RESTORED FROM CHAMP AMPLITUDE DATA

In this section an example of practical application of the amplitude method to CHAMP data analysis will be shown. In Fig. 5.14 a comparison of the amplitude data and perturbations of the vertical gradient of the refractivity are shown for CHAMP RO event 0001, February 23, 2003 for tropical region in

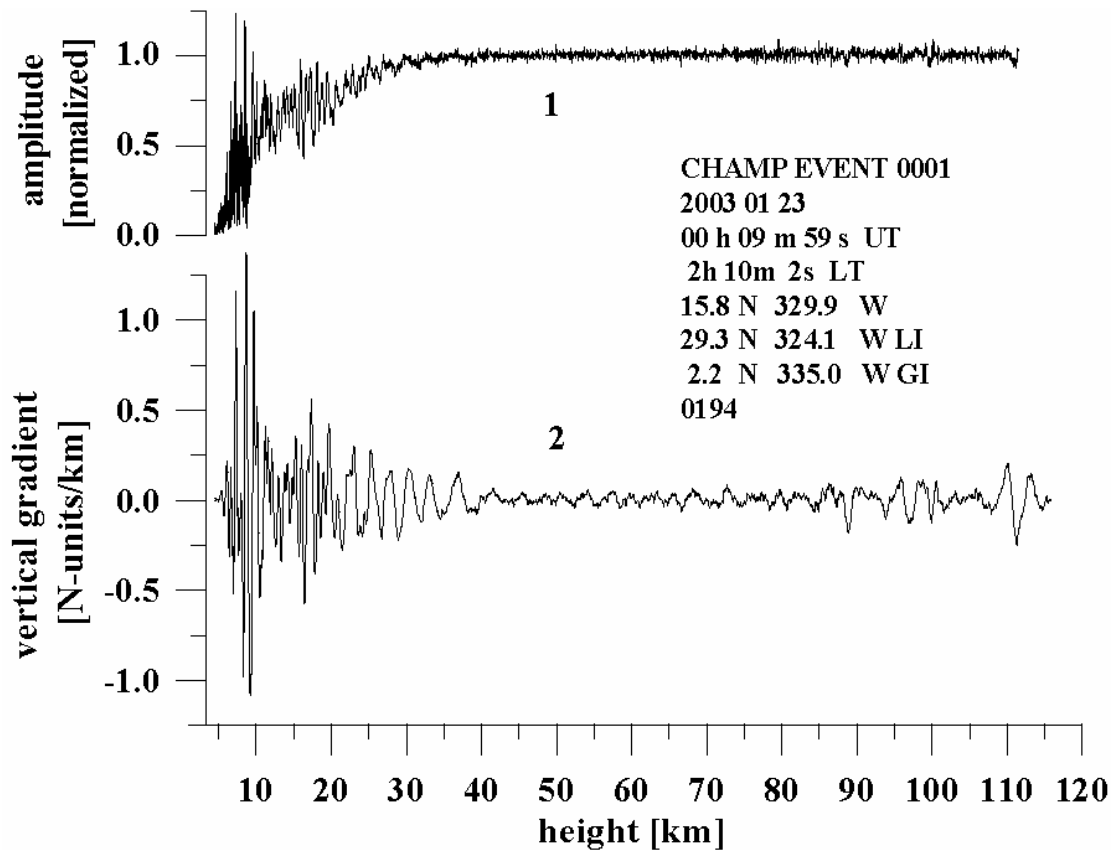


Fig. 5.14. Comparison of the amplitude data (curve 1) and perturbations in the vertical gradient of the refractivity (curve 2). The wave structure is clearly seen in the amplitude data up to height 40-43 km. The wave structure is evident in the perturbations of the vertical gradient of the refractivity below the altitude 40 km. The increasing of the vertical period is observed in the 15-35 km interval.

the Sahara desert. The wave structure is clearly seen in the perturbations of the vertical gradient of the refractivity in the 8-40 km interval. The vertical period of the wave structure is growing from 0.8-1.0 km in the 8-25 km interval up to 3 km in the 30-40 km interval. This corresponds to increasing of the intrinsic phase speed of the GW with height by 3-3.2 times. Above 40 km the amplitude of the vertical gradient perturbations is diminished by 3 times, however the wave structure with changing vertical period is evident in the 40-90 km interval. The ionospheric influence is seen in the 90-120 km interval. The perturbations in the vertical gradient of the refractivity can be recalculated to the temperature gradient variations, temperature variations and then, using the polarization relationships, in the horizontal wind perturbations.

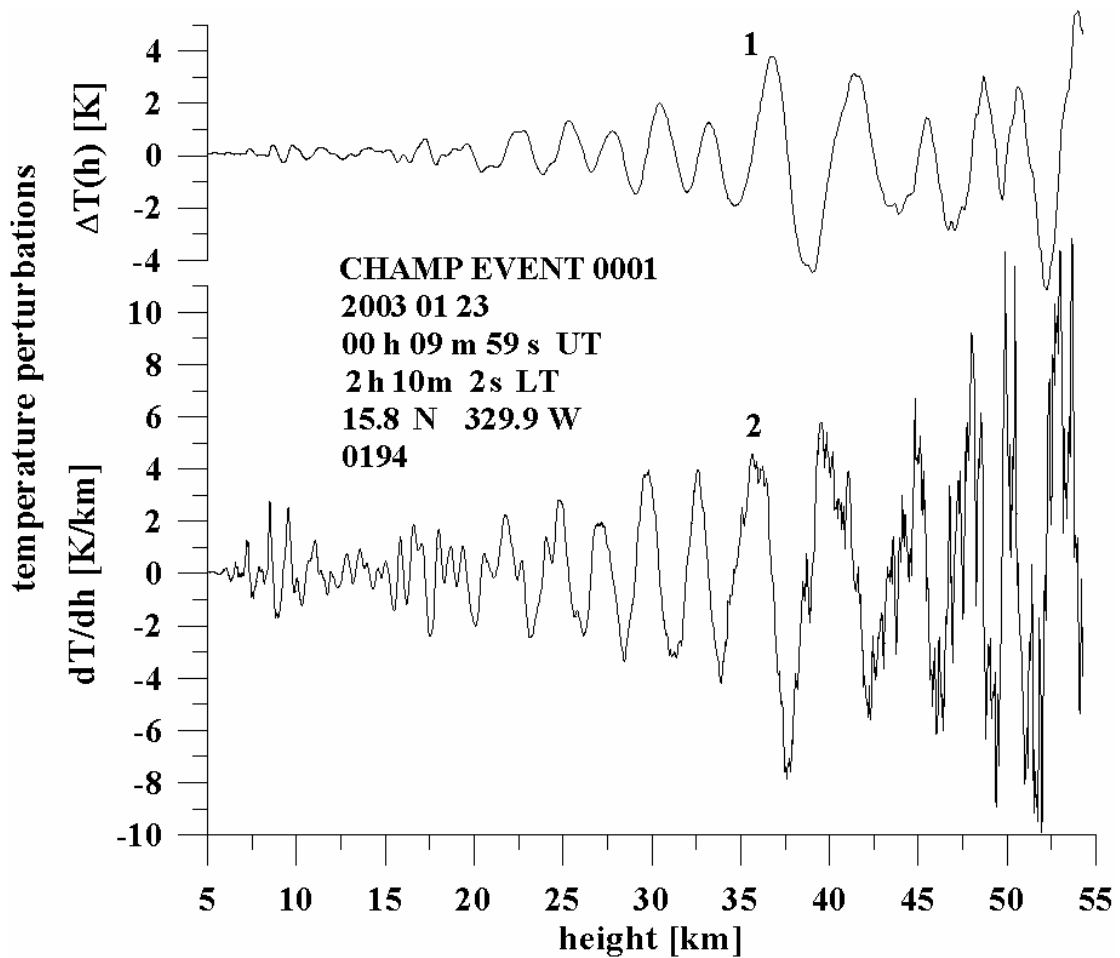


Fig. 5.15. The vertical temperature gradient and temperature perturbations found using the vertical gradient of the refractivity variations.

In Fig. 5.15 the perturbations of the temperature (curve 1) and their vertical gradients (curve 2) are shown. As it seen in Fig. 5.15, the vertical temperature gradient is increasing with height from  $\pm 2$  K/km (8-20 km interval) up to  $\pm 8$  K/km (30-48 km interval). The corresponding temperature variations are changing from  $\pm 0.2 - \pm 1.0$  K (8-20 km interval) up to  $\pm 4$  K (30-48 km interval). The vertical period of the vertical temperature gradient variations is changing from 0.8 km (8-20 km interval) up to 5 km (35-42.5 km interval). In the 49-51 km interval one can note the diminishing of the vertical period up to 2 km. The temperature and its vertical gradient perturbations

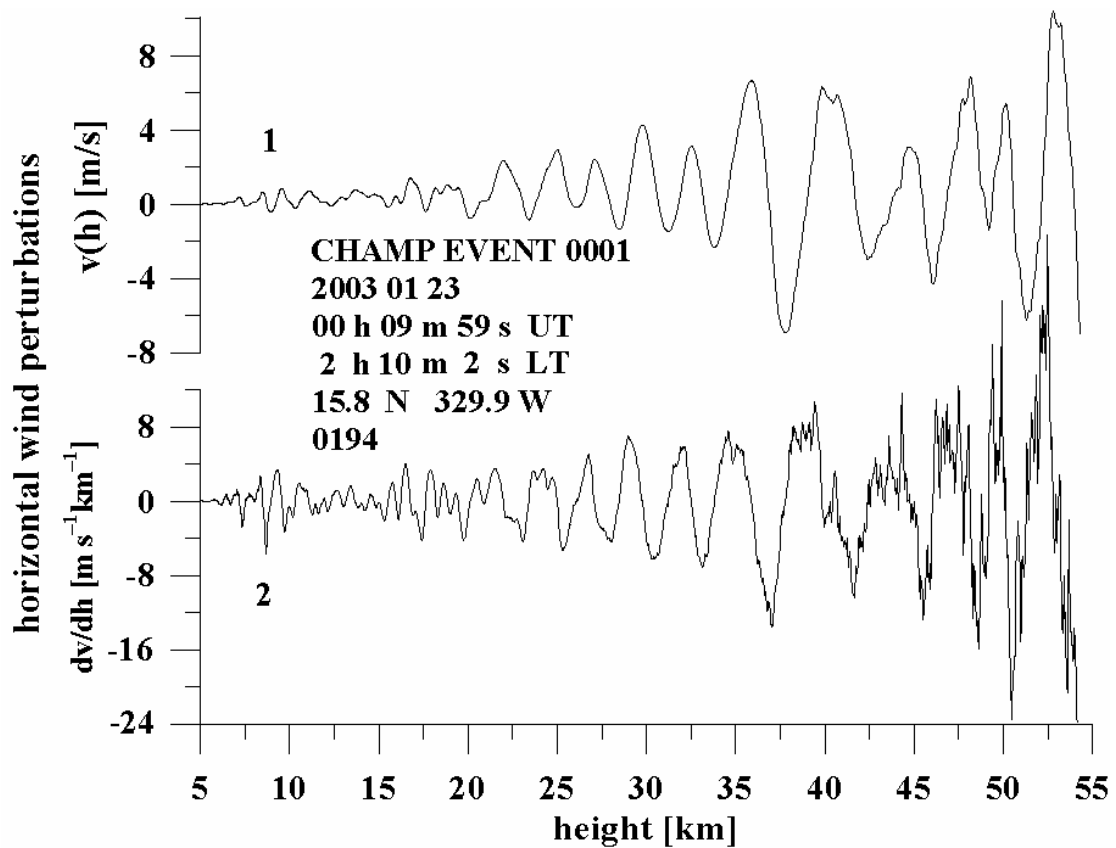


Fig. 5.16. The horizontal wind and its vertical gradient perturbations.

can be recalculated using the GW polarization relationships to the horizontal wind perturbations and its vertical gradient. The results are shown in Fig. 5.16. The amplitude of the horizontal wind perturbations is changing from  $\pm 0.5$  m/s up to  $\pm 5.0$  m/s when the height changes from 10 km up to 40 km (curve 1 in Fig. 5.16). The corresponding values of the vertical gradient of the horizontal wind perturbations is changing from  $\pm 2$   $\text{m s}^{-1}\text{km}^{-1}$  up to  $\pm 8$   $\text{m s}^{-1}\text{km}^{-1}$ , when the height changed from 8-10 km up to 46 km. The changes in the vertical period can be seen in Fig. 5.17, which shows the phase portrait of GW.

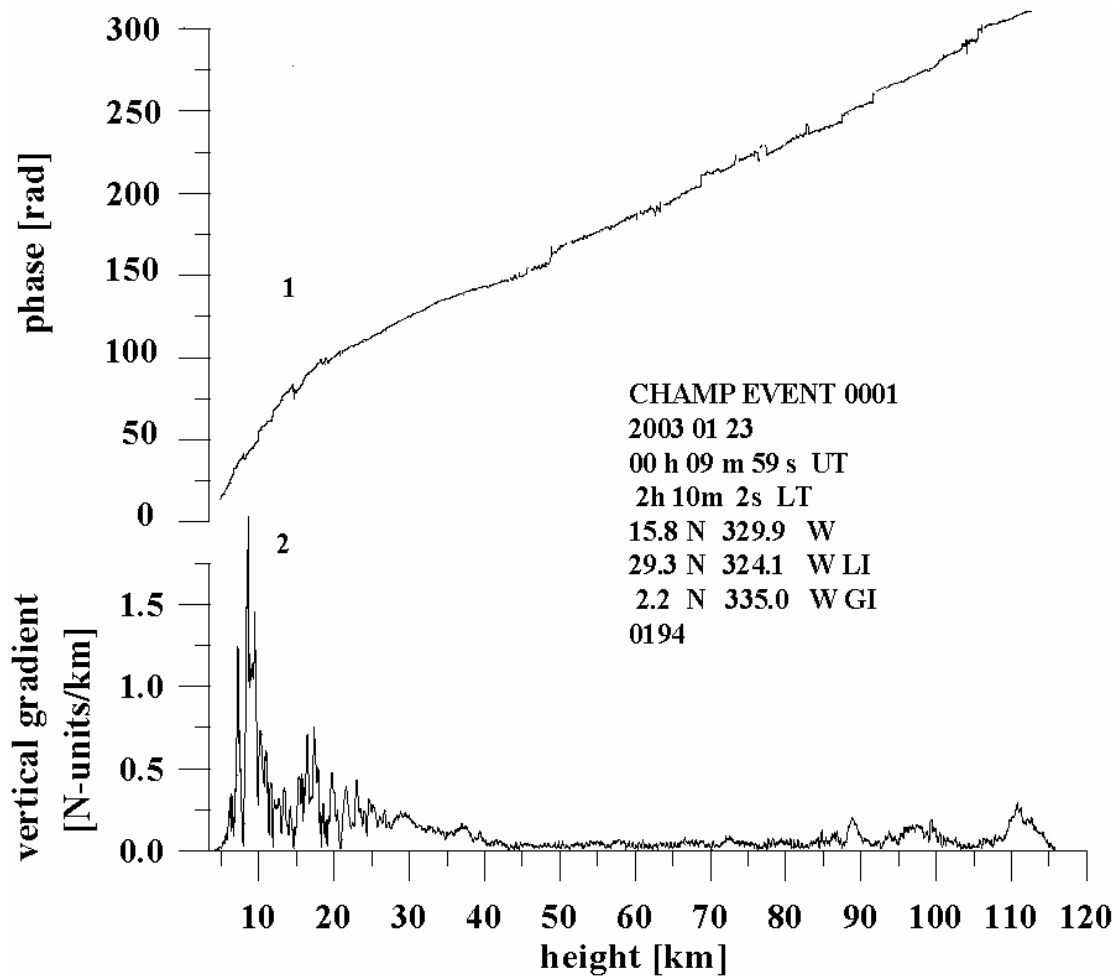


Fig. 5.17. Phase portrait of GW. Curve 1 relates to the phase changes, curve 2 describes the amplitude variations in GW.

General form of the phase of GW as function reveals gradual diminishing of the vertical spatial frequency in GW (this corresponds to increasing in spatial period of GW). The sharp changes in the phase correspond to the height where the amplitude of GW is below the noise level and the coherence in GW is disappeared. These regions can correspond to the boundaries of the wave breaking altitudes where the energy of GW is transmitting to turbulent structures in the stratosphere. The amplitude of GW is maximal in the 8-40 km interval. The height intervals between 43 and 45 km, 59 and 63 km can be considered as the boundaries of the GW breaking areas.

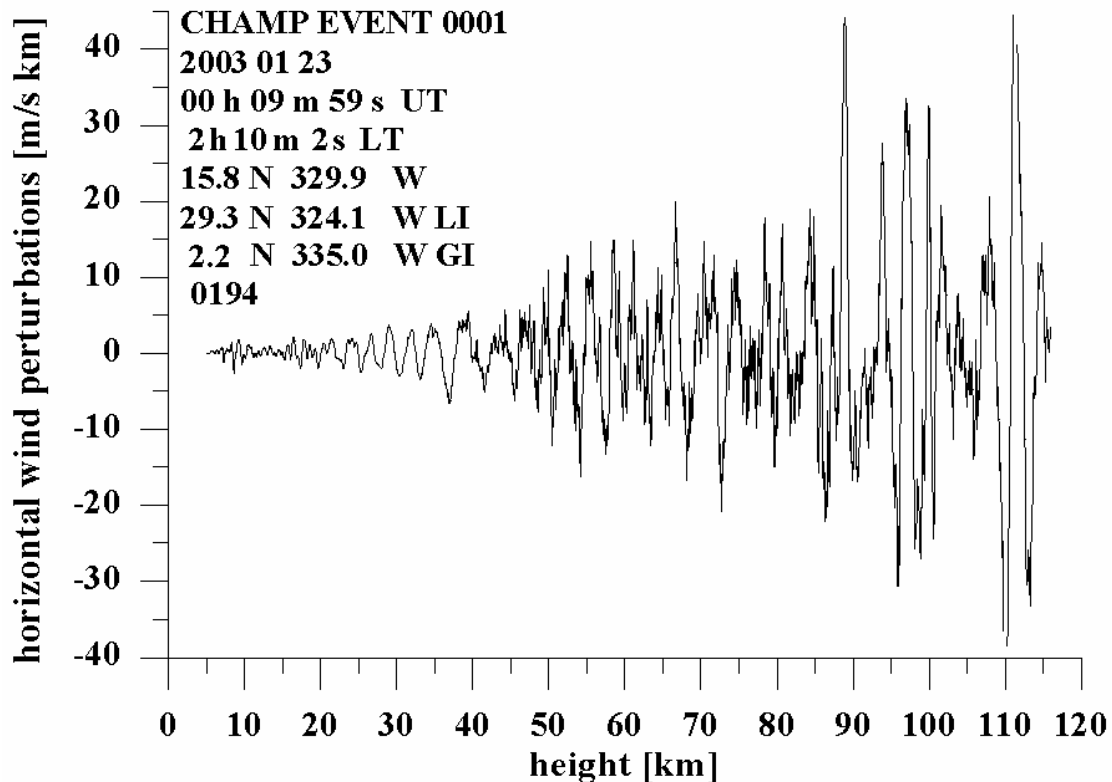


Fig. 5.18. The vertical distribution of the wave structures in the 8-115 km interval. For calculation of  $dv(h)/dh$  equations (5.9), (5.10), (5.15) and (5.16) have been used. For convenience of illustration the function  $dv(h)/dh$  has been multiplied for  $h > 50$  km by the damped exponential  $\exp[-(h-50)/H]$ ,  $H=6.3$  km, to exclude the exponential increasing of  $dv(h)/dh$  in the interval of height greater than 50 km.

The vertical distribution of the wave activity in the height interval 8-115 km is shown in Fig. 5.18. In Fig. 5.18 the height intervals with low wave amplitude: 43-45 km, 62-65 km, 76-78 km can be seen. In these intervals the phase of the wave structures is not continuous. The wave structures do not have coherence properties between these intervals. These intervals isolated the wave structures in different altitude areas. It follows that the 43-45 km, 62-65 km and 76-78 km intervals are the areas where the energy of GW is disappeared in the turbulent eddies. These areas are the regions of GW breaking. The wave structures above 90 km can be connected with ionospheric influence (Fig. 5.18).

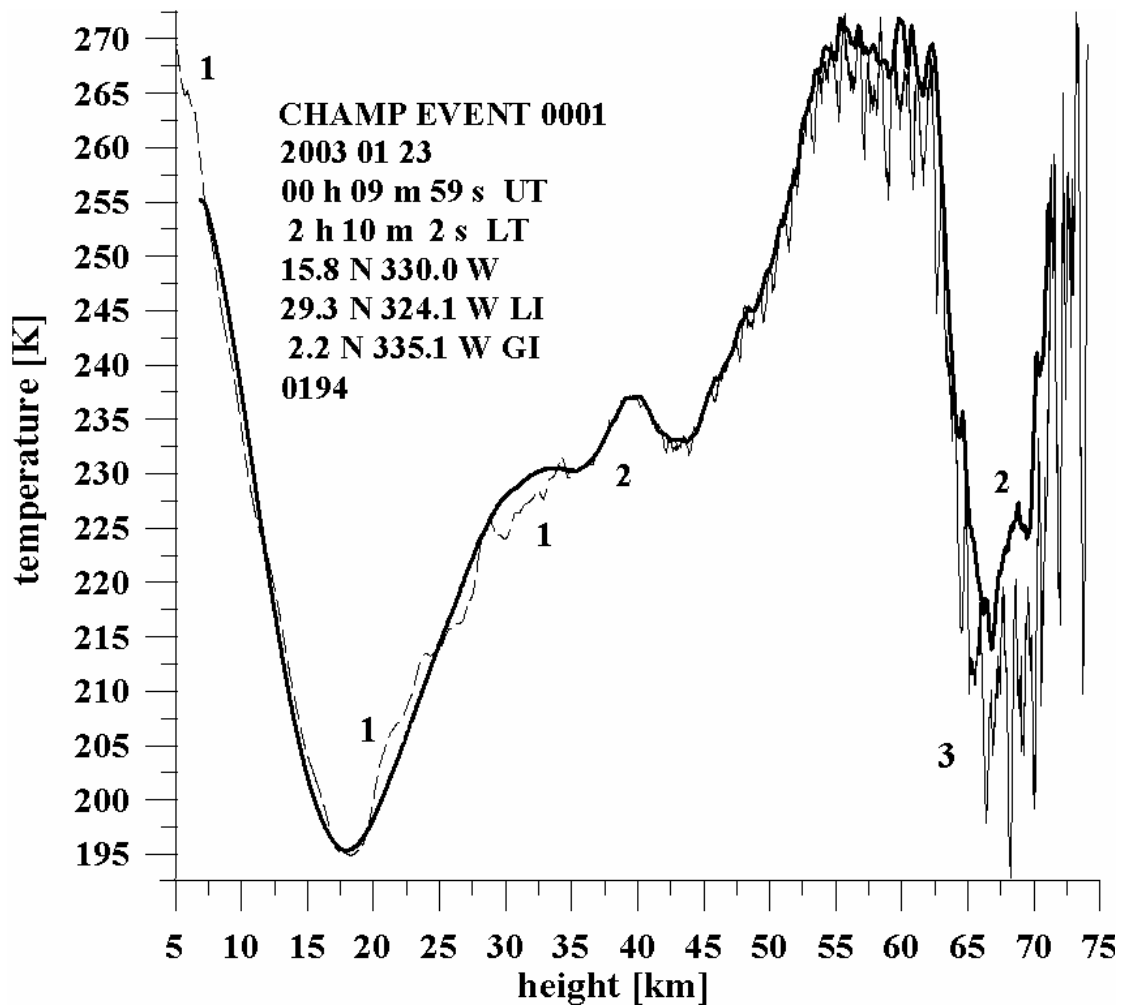


Fig. 5.19. The vertical temperature profile found from the phase data by traditional method (curve 1, dashed), UPMA method (smooth curve 2) and UPM method (curve 3). The sharp changes corresponding to curve 3 are caused by phase excess spikes at frequency F2.  $S_4$  index was equal to 0.04. This value corresponds to the quiet ionosphere.

In Fig. 5.19 the temperature vertical profile  $T(h)$  [K] is shown for the same event as in Fig. 5.16-5.18. The function  $T(h)$  was obtained from the phase data at combined frequency F0 (ionospheric correction has been introduced in the phase path excess) by means of the traditional phase method (shown by dashed curve 1 from 5 km up to 35 km in Fig. 5.19), UPMA method (smooth curve 2) and UPM method (curve 3). There is good correspondence between curves 1-3 in the height interval 6-35 km. The traditional method gives not so smooth  $T(h)$  profile, with deflection about 2-4 K in the 20-35 km interval. This is owing to the operation of differentiation of the phase path excess included in the traditional method. The differentiation allows for obtaining

more details in the temperature profile. However the UPMA and UPM methods reveal the function  $T(h)$  from 35 up 74 km, where the traditional method can give reliable results using statistical optimization method with appropriate model describing expected refractivity profile in the atmosphere. UPM and UPMA methods use the traditional method for parametrization of the temperature profile in the 35-75 km interval. The data in Fig. 5.19 can be compared with data shown in Fig. 5.18. There is a region of possible instability in the atmosphere in Fig. 5.19. This region corresponds to the 60-68 km interval where the temperature vertical gradient is negative and is very near to the adiabatic lapse rate  $-9.8$  K/km. This region corresponds to the 60-68 km interval in Fig. 5.18 where the GW energy is disappearing. Thus we can see a correspondence between the amplitude data and phase data. The amplitude data are more simply for analysis than the phase data because the current phase methods give the temperature profiles, as a rule, only up to height 35 km. The amplitude data are available in a broader interval of heights. Only limitation consists in the ionospheric influence when the ionospheric irregularities introduce difficulties in the deciphering of the amplitude data. This shows importance of the amplitude data at the second GPS frequency for observation GW activity in the atmosphere.

## SUMMARY AND CONCLUSIONS

1. As follows from the consideration of the approximations and features of different radio holographic methods, the RFSA method can resolve the different rays in the multi-path situation and restore the field in physical space between transmitter and receiver, thus having feasibility to obtain radio image of the ionosphere, atmosphere and the Earth's surface. This has been demonstrated when signatures of reflected components were detected at the first time in GPS/MET and also CHAMP RO data.

The 1D radio images obtained by the RFSA method have been used to set an upper limit on the vertical resolution of GPS RO method of  $\sim 70$  m.

The BP method is useful in the case of absence of multi-path propagation and thus has limited application because of possible phase distortions in multi-path situation. BP method has an important feasibility to estimate the location of ionospheric disturbances, because BP method restores the field in physical space. The position of a disturbance can be determined by the BP method as a location in space where the amplitude scintillations in the restored field have minimum value (*Sokolovskiy, et al. 2002*). The same feasibility, as shown in this report, has RFSA, as a method, which allows for the restoration of the field in physical space. Because of this feasibility both, the RFSA and the BP method, share, in principle, the common property to locate inhomogeneities along with tomographic methods derived earlier. However this property must be checked by mass-scale analysis of the RO data and validation by Earth-based ionosondes measurements.

The GIO and CT method can disentangle multi-path rays and find the dependence of the refraction angle on the impact parameter in the case when the modified refractivity index is a monotonic function of the altitude. GIO transform has some advantage because the CT method in the current state is valid for the specific case when the orbit of the LEO satellite is perpendicular to the direction to the GPS satellite. The GIO transform is valid for general case of any inclination of the orbit of the LEO satellite. Both GIO and CT method present the field in the abstract space and require the knowledge of location of the center of global spherical symmetry of the medium.

2. The amplitude of the GPS signal is a radio holographic indicator of ionospheric disturbances in the trans-ionospheric links, including the RO links and satellite-to

Earth links. As it was shown in this report, the amplitude variations of the RO signal in the 40-80 km altitude interval of the tangent point T (Fig. 2.1) are a valuable source of information on the structure of ionospheric disturbances. The classification of amplitude variations of GPS signals is introduced. There are two types of amplitude variations: noisy and quasi-regular. This classification coincides with the types of the amplitude variations previously observed in satellite-Earth trans-ionospheric links. It is established, that quasi-regular amplitude variations can be inverted to obtain electron density distributions and its gradient in inclined ionospheric layers. Moreover, the RFSA method has the capability to establish the location of the inclined ionospheric layers by estimating the curvature radius of the wave front along the LEO orbit. Thus the amplitude part of the RO signals can be used as a radiohologram to find parameters and the localization of the ionospheric disturbances.

The seasonal, geographical and temporal distributions of the CHAMP RO events with high  $S_4$  index values observed during the years 2001-2003 indicate their dependence on solar activity. The number of RO events with  $S_4$  index higher than 0.2 is a good indicator for the presence of ionospheric disturbances. The spatial distributions of the RO events with  $S_4$  index higher than 0.2 revealed seasonal, geographical and temporal dependence of ionospheric disturbances connected with solar activity and indicated two mechanisms of ionization: (1) ionization owing to the fast electron moving in downward direction from the magnetosphere and (2) solar radiation.

3. The phase data contain more information than it is supposed earlier. Usually the phase information has been used to obtain the refraction index, temperature, pressure, humidity in the altitude interval 0-35 km. For extrapolation of the vertical profiles of these physical parameters to the 35-70 km interval usually the

method of the statistical optimization has been applied. This method requires the use of an atmospheric refractivity model in the RO vertical region. We have proposed a new method for this task. This technique uses the data in the 5-35 km interval for the parameterization of the vertical atmospheric profiles. The method is applied to the analysis of the phase data and the results showed good correspondence with Earth-based lidar observations of the vertical temperature profiles. Thus this method holds a great promise to be introduced for RO phase data analysis after careful examination in mass-scale using the RO data.

4. The current GW theory is reconsidered with the goal to be applied for the RO data analysis. The polarization and dispersion relationships are obtained and the approximations and assumptions of the GW theory are revealed. It follows from this consideration, that the polarization relationships can be used for the RO data analysis if the frequency of GW is far above the inertial frequency and far below the Brunt-Vaisala frequency. A new equation is introduced which contains the connection between the relative variations of the refractivity (or density) and the horizontal wind perturbations associated with GW. Thus it is shown that the polarization and dispersion relationships for GW can be applied for the RO data analysis.

5. The radio holographic content of the amplitude variations in the GPS occultation signals has been analyzed. The way how to obtain from the RO amplitude variations the phase and amplitude of GW as a function of height is described and validated using GPS/MET and CHAMP RO data. One can obtain the perturbations in the vertical gradient of the refractivity from the GPS RO amplitude variations. Then using the GW polarization relationships one can find the horizontal wind perturbations and its vertical gradient as a function of the altitude. The vertical temperature gradient perturbations can also be derived. Comparisons of the horizontal

wind perturbations obtained from the amplitude data analysis with radiosonde data reveal good correspondence. Radio holographic analysis of the CHAMP RO data has shown the possibility to reveal locations of GW breaking regions in the stratosphere, thus introducing complementary source of information on the physical conditions in the stratosphere to the information obtained from the RO phase data.

## RECOMMENDATIONS

The main result of the work consists in the presentation of a new amplitude radio holographic method for (1) analyzing ionospheric disturbances and estimating the electron density distribution (and its gradient) in ionospheric layers, (2) locating of inclined ionospheric layers, (3) obtaining maps of the seasonal, geographical and temporal distributions of RO events with high values of the  $S_4$  index thus revealing the location and intensity of ionospheric disturbances as function of solar activity and space weather phenomena, (4) investigating the seasonal, geographical and temporal distribution of the GW activity in the altitude 5-100 km altitude interval. These four tasks are now in different states of elaboration. The task (3) is developed and the maps of the geographical distribution of the strong ionospheric events for three years of CHAMP mission are obtained. These maps evidently showed the correlation of ionospheric disturbances with solar activity and magnetospheric phenomena. The main recommendation for task 3 consists in preparing the same maps for the GPS/MET experiment and including the generation of these maps to the routine operational data analysis of the CHAMP and future RO missions. The task 1 and 2 are concerned with quasi-regular ionospheric perturbations. For these kinds of ionospheric perturbations it is possible to find the electron density distribution and its gradient and to locate them by measuring the minimal curvature of the wave front using the radio hologram obtained at two GPS frequencies. The tasks 1 and 2 are

important for future investigations. The method of the electron density retrieval (and its gradient) must be validated using ionosonde data. The task 4 is new direction for RO investigations. It must be elaborated in more detail including the validation with radiosonde data and information obtained from meteorological analysis. From the theoretical point of view it is evident now that the theory of GW can be modernized by using the RO data for the study of the GW activity with global coverage. For example, in this report a new polarization equation for GW is presented. This equation correlates relative refractivity variations with horizontal wind perturbations. This relation excludes the difficulty connected with implicit assumption of the isothermal atmosphere in the current GW theory because the background refractivity profiles are obtained directly from the phase data. The amplitude method for GW detection in the atmosphere is well described and holds great promise to be effective in the operational data analysis in current and future RO missions.

The new UPM method, which is designed to obtain vertical profiles of physical parameters in the upper stratosphere, is now in the beginning of elaboration. The results obtained by this method must be validated by Earth-based and satellite data. However the preliminary results showed its efficiency and the task for future consists in the mass-scale analysis of the possibilities of the UPM method using GPS/MET, CHAMP and SAC-C RO data.

As a result we recommend:

1. To include the generation of the global maps showing the geographical, seasonal and temporal distribution of the RO events with strong amplitude variations to the routine operational data analysis. These maps can be published at the web site of the CHAMP RO team as an information tool for the current state of the ionospheric activity important for the analysis of space weather phenomena, which are correlated

with the solar activity. They also can be used for the estimation of the conditions of radio wave propagation and communication in trans-ionospheric links.

2. To further elaborate the amplitude radio holographic method for observing the seasonal, geographical and temporal distribution of the GW activity and the estimation of its parameters (including the horizontal wind perturbations) in the altitude interval 1-100 km.

3. To further elaborate the method for the estimation of ionospheric disturbance parameters and the disturbance localization by using radio holographic methods.

4. To derive a new method for the analysis of the phase part of the radio hologram with the aim to obtain reliable information of the vertical distribution of refractivity, temperature, and pressure in the stratosphere and mesosphere.

#### ACKNOWLEDGMENTS

The authors are very grateful to the CHAMP team from GFZ Potsdam for the provision of CHAMP and GPS/MET RO data for the analysis and also for the financial and organisational support of our work. We are grateful to the Principal Investigator of the CHAMP mission, Prof. Ch. Reigber for multi-years supporting the cooperation between GFZ Potsdam and IRE RAS. The report is results of a research contract between IRE RAS and GFZ and was funded by GFZ.

## REFERENCES

- Beyerle, G., and K. Hocke; Observation and Simulation of Direct and reflected GPS Signals in RO Experiments. *Geophys.Res. Lett.* **28**. 9. 1895-1898, 2001.
- Beyerle, G., K. Hocke, J. Wickert, T. Schmidt, C. Marquardt, and Ch. Reigber; GPS ROs with CHAMP: A Radio Holographic Analysis of GPS Signal Propagation in the Troposphere and Surface reflections, *J. Geophys. Res.*, **107**(D24), doi:10.1029/2001JD001402, 2002.
- Eckermann S.D., I. Hirota, and W.A. Hocking; GW and equatorial wave morphology of the stratosphere derived from long-term rocket soundings. *Q.J.R. Meteorol. Soc.* **121**. 149-186, 1995.
- Eckermann S.D., and P. Preusse; Global Measurements of Stratospheric Mountain Waves from Space, *Science*, **286**, 1534-1537, 1999.
- Egorov, Yu.V.; Lectures on partial differential equations. Additional chapters. Moscow State University Press. Moscow (In Russian), 1995.
- Fritts D.C., and M.J. Alexander; GW dynamics and effects in the middle atmosphere. *Rev. Geophys.*, **41**, pp 3-1-3-64, 2003.
- Gorbunov, M.E., A.S. Gurvich, and L. Bengtsson; Advanced algorithms of inversion of GPS/MET satellite data and their application to construction of temperature and humidity, Report 211, *Max-Planck-Institute for Meteorology*, ISSN0937-1060, 1996.
- Gorbunov M. E.; Radio-Holographic Analysis of Microlab-1 RO Data in the Lower Troposphere. *J. Geophys. Res.*, **107** (D12), doi: 10.1029/2001JD000889, 2002a.
- Gorbunov M. E.; Radioholographic Analysis of RO Data in Multi-path Zones. *Radio Sci.* **37**(1), doi: 10.1029/2000RS002577, 2002b.
- Gorbunov M. E.; Canonical Transform Method for Processing GPS RO Data in Lower Troposphere, *Radio Sci.* **37**(5), doi: 10.1029/2000RS002592, 2002c.

- Gorbunov M. E., A. S. Gurvich, and L. Kornblueh; Comparative Analysis of Radioholographic Methods of Processing RO Data, *Radio Sci.* **35(4)**, 1025-1034, 2000.
- Gorbunov M. E., and L. Kornblueh; Analysis and Validation of GPS/MET RO Data, *J. Geoph. Res.*, **106** (D15), 17,161-17,169, 2001.
- Gorbunov, M.E.; Radio holographic methods for processing RO data in multi-path regions. Scientific report 01-02. Danish Meteorological Institute, Copenhagen, 2001.
- Heise S., N. Jakowski, A. Wehrenpfennig, Ch.Reigber, and H. Lühr; Sounding of the topside ionosphere/plasmasphere based on GPS measurements from CHAMP: Initial results. *Geophys. Res. Lett.*, 29(14), doi: 10.1029/2002GL014738, 2002.
- Hocke, K.; Inversion of GPS meteorology data, *Ann. Geophys.* 15, 443-450, 1997.
- Hocke, K., A. Pavelyev, O. Yakovlev, L. Barthes, and N. Jakowski; RO data analysis by radio holographic method, *J. Atmos. Solar-Terr. Phys.* **61**, 1169-1177, 1999.
- Igarashi, K., A. Pavelyev, K. Hocke, D. Pavelyev, and J. Wickert; Observation of wave structures in the upper atmosphere by means of radio holographic analysis of the RO data, *Adv. Space Res.*, **27**, 6-7, 1321-1327, 2001.
- Igarashi, K., A. Pavelyev, K. Hocke, D. Pavelyev, I.A. Kucherjavenkov, S. Matugov, A. Zakharov, and O. Yakovlev; Radio holographic principle for observing natural processes in the atmosphere and retrieving meteorological parameters from RO data. *Earth Planets Space*, **52**, 968-875, 2000.
- Jensen A. S., M. S. Lohmann, H.-H. Benzon, and A. S. Nielsen; Full Spectrum Inversion of RO Signals, *Radio Sci.*, **38** (3)., doi: 10.1029/2002RS002763, 2003.
- Kalashnikov, I., S. Matugov, Pavelyev A., and O. Yakovlev; Analysis of the features of RO method for the Earth's atmosphere study. In the book *Electromagnetic waves in the atmosphere and space*, 208-218, "Nauka" Ed. Moscow (in Russian), 1986.

- Karasawa, Y., K. Yasukawa, and M. Yamada, Ionospheric scintillation measurement at 1.5 GHz in mid-latitude region, *Radio Sci*, 20(3), 643-651, 1985.
- Kunitsyn V.E., and E.D. Tereshchenko; Tomography of the ionosphere. Moscow, Nauka Ed. (In Russian), 1991.
- Kunitsyn, V.E., E.S Andreeva, E.D. Tereshchenko, B.Z. Khudukon, and T. Nygn; Investigations of the ionosphere by satellite radiotomography. *Int. J. of Imaging Syst. and Techn.*, **5**. 112-127, 1994.
- Lindzen R.S.; Turbulence and stress owing to GW and tidal breakdown, *J. Geophys. Res.* **86**, C-9, 707-714, 1981.
- Lindal G. F., J. R. Lyons, D. N. Sweetnam, V. R. Eshleman, D. P. Hinson, and G. L. Tyler; The Atmosphere of Uranus: results of RO Measurements with Voyager, *J. Geophys. Res.*, **92**, A13, 14,987-15,001, 1987.
- Liou, Y.-A., A.G. Pavelyev, C.-Y. Huang, K. Igarashi, and K. Hocke; Simultaneous observation of the vertical gradients of refractivity in the atmosphere and electron density in the lower ionosphere by RO amplitude method, *Geophys. Res. Lett.*, **29(19)**, 1937, doi: 10.1029/2002GL015155, 2002.
- Liou Y.A., and C.Y. Huang, Active Limb Sounding of Atmospheric refractivity, Pressure, and Temperature Profiles from GPS Occultation by 3-D Vector Analysis. *Proc. of COSMIC International Workshop. September 27-29, 2000*, pp. 60-69. Taipei, Taiwan, 2000.
- Liou, Y.-A., and C.-Y. Huang; Active limb sounding of atmospheric refractivity and dry temperature profiles by GPS/Met occultation, In: *Space Weather Study Using Multi-point Techniques*, Ling-Hsiao Lyu (Ed.). COSPAR Colloquia Series, **12**, 60-69, 2002.

- Liou, Y.-A., A.G. Pavelyev, C.-Y. Huang, K. Igarashi, K. Hocke, and S. K. Yan; Analytic method for observation of the GW using RO data, *Geophys. Res. Lett.*, **30(20)**, 2021, doi:10.1029/2003GL017818, 2003.
- Marouf, E.A., and G.L. Tyler; Microwave edge diffraction by features in Saturn's rings: Observations with Voyager 1, *Science*, **217**, 243-245, 1982.
- Pavelyev A.G., and A.I. Kucherjavenkov; Refraction attenuation in the planetary atmospheres, *Radio Eng. and Electron. Phys.*, **23(7)**, 13-19, 1978.
- Pavelyev A.G, and S.D. Yeliseev; Study of the Atmospheric Layer near the Ground using Bistatic Radar, *J. Comm. Techn. and Electron.*, **34(9)**, 124-130, 1989.
- Pavelyev, A.G.; Informational structure of image functions and possibility of detecting systematic errors in the solution of ill-posed problems. *Sov. Phys. Dokl.* **35(3)**, 272-274, March 1990.
- Pavelyev A., A.V. Volkov, A.I. Zakharov, S.A. Krytikh, and A.I. Kucherjavenkov; Bistatic radar as a tool for earth investigation using small satellites. *Acta Astron.* **39(6)**, 721-730, 1996.
- Pavelyev A., A.I. Zakharov, A.I. Kucherjavenkov, E.P. Molotov, A.I. Sidorenko, I.L. Kucherjavenkova and D. A. Pavelyev; Propagation of radio waves reflected from Earth's Surface at grazing angles between a Low-Orbit Space Station and Geostationary Satellite, *J. Comm. Techn. and Electron*, **42(1)**, 45-50, 1997.
- Pavelyev A.G.; On the possibility of radio holographic investigation on communication link satellite-to-satellite. *J. Comm. Techn. and Electron.* **43(8)**, 126-131, 1998.
- Pavelyev A., K. Igarashi, C. Reigber, K. Hocke, J. Wickert, G. Beyerle, S. Matyugov, A. Kucherjavenkov, D. Pavelyev, and O. Yakovlev; First application of radioholographic method to wave observations in the upper atmosphere, *Radio Sci.* **37(3)**, 1043, doi: 10.1029/2000RS002501, 2002a.

- Pavelyev A.G., Y.A. Liou, C. Y. Huang, C.Reigber, J. Wickert, K. Igarashi, K. Hocke;  
Radio holographic method for the study of the ionosphere, atmosphere and terrestrial  
surface from space using GPS occultation signals. *GPS Solutions*, 6, 101-108, 2002b.
- Pavelyev A.G., T. Tsuda, K. Igarashi, Y.A. Liou, and K. Hocke; Wave structures in the  
electron density profile in the ionospheric D and E-layers observed by radio  
holography analysis of the GPS/MET RO data, *J. Atmos. Solar-Terr. Phys.*, **65**, 1, 59-  
70, 2003.
- Pavelyev A.G., Y. A. Liou, J. Wickert; Diffractive vector and scalar integrals for bistatic  
radio holographic remote sensing, *Radio Sci.*, 39 (4), RS4011, 1-16,  
doi:10.1029/2003RS002935, 2004.
- Pedlosky, J., Geophysical fluid dynamics, Springer –Verlag, New York Heidelberg Berlin,  
v. 1, 1982.
- Pfister, L., K.R. Chan, T.P. Bui, S. Bowen, M. Legg, B. Gary, K. Kelly, M. Proffit, and W.  
Starr; GW generated by a tropical cyclone during the STEP tropical field program: a  
case study. *J. Geophys. Res.*, **98**. D5, 8,611-8,638, 1993.
- Rabiner L., and B. Gold; Theory and Application of Digital Signal Processing. Pontis Hall,  
1978.
- Rocken, C., R. Anthes, M. Exner, D. Hunt, S. Sokolovskiy, R. Ware, M. Gorbunov, W.  
Schreiner, D. Feng, B. Herman, Y.-H. Kuo, and X. Zou; Analysis and validation of  
GPS/MET data in the neutral atmosphere. *J. Geophys. Res.*, **102**. 29849-29866., 1997.
- Reigber, Ch., P. Schwintzer, H. Lühr, and J. Wickert (Eds.); Earth Observation with  
CHAMP: Results from Three Years in Orbit, Springer Verlag, Berlin Heidelberg  
New-York. 2005.
- Sokolovskiy, S.V.; Inversion of RO amplitude data, *Radio Sci.*, **35**. 1. 97-105, 2000.

- Sokolovskiy, S.V., W. Schreiner, C. Rocken, and D. Hunt; Detection of high-altitude ionospheric irregularities with GPS/MET, *Geophys.Res. Lett.* **29**(3). 621-625, 2002.
- Steiner, A. K., G. Kirchengast, und H. P. Ladreiter; Inversion, error analysis and validation of GPS/MET data, *Ann. Geophys.*, **17**, 122-138, 1999.
- Steiner, A. K., and G. Kirchengast; GW spectra from GPS/MET occultation observations, *J. Atmos. Ocean. Tech.*, **17**. 495-503, 2000.
- Tsuda T., M. Nishida, C. Rocken, and R.H. Ware; A global morphology of GW activity in the stratosphere revealed by the GPS occultation data (GPS/MET). *J. Geophys. Res.* **105**. 7257-7273, 2000.
- Tsuda T., and K. Hocke; Vertical wave number spectrum of temperature fluctuations in the stratosphere using GPS occultation data, *J. Met. Soc. Japan.* **80**. 4B. 1-13, 2002.
- Yeh, K.C., and C.H. Liu; Radio wave scintillations in the ionosphere. *Proc. IEEE*, **70**(4), 324-360, 1982.
- Wickert, J., Ch. Reigber, G. Beyerle, R. König, C. Marquardt, T. Schmidt, L. Grunwaldt, R. Galas, T. Meehan, W. Melbourne, and K. Hocke; Atmosphere sounding by GPS ratio occultation: First results from CHAMP, *Geophys.Res. Lett.*, **28**, 3263-3266, 2001.
- Wickert, J.; Das CHAMP-Radiookkultationsexperiment: Algorithmen, Prozessierungssystem und erste Ergebnisse, *Scientific Technical Report STR02/07*, GFZ Potsdam, 2002.
- Wickert, J., A.G. Pavelyev, Y. A. Liou, T. Schmidt, Ch. Reigber, K. Igarashi, A.A. Pavelyev, and S. Matyugov; Amplitude variations in GPS signals as a possible indicator of ionospheric structures, *Geophys. Res. Lett.*, **31**, L24801, doi:10.1029/2004GL020607, 2004.
- Zverev V. A. Radio-optics, Moscow, Soviet Radio Ed., 1975.